

# **Investigating Abundances in Galaxy Clusters and Gas Motions in M87 using XRISM**

by

Neo Dizdar

A thesis  
presented to the University of Waterloo  
in fulfillment of the  
thesis requirement for the degree of  
Masters of Science  
in  
Physics and Astronomy

Waterloo, Ontario, Canada, 2025

© Neo Dizdar 2025

### **Author's Declaration**

I hereby declare that I am the sole author of this thesis. This is a true copy of the thesis, including any required final revisions, as accepted by my examiners.

I understand that my thesis may be made electronically available to the public.

## Abstract

Galaxy clusters are the forefront of extragalactic diffuse X-ray astrophysics, yet there are still many questions about their formation and evolution. The creation of XRISM, a new X-ray imaging and spectroscopy mission, will study the metal abundance history of clusters and the conversion of jet energy into atmospheric kinetic energy. XRISM's payload contains an instrument with the highest spectral resolution (5 eV) in the field of X-ray astronomy so far. With this resolution, we observed metal abundances and the broadening of metal lines through turbulent motions in the intracluster medium.

In this thesis I present the conversion of data from the Chandra X-ray Observatory to XRISM's high-resolution format. This includes the preparation and selection of clusters in Chandra, simulating selected clusters for XRISM and applying for proposals. Finally, we extracted abundance and velocity information from the Virgo cluster's early XRISM data.

I prepared a subset of 16 galaxy clusters with a wide array of morphologies and redshifts using the Chandra X-ray database. This produces radial profiles of metallicity, temperature, and cooling time for each cluster. The entire subset shows that the metallicity asymptotically reaches 0.3 solar abundance ( $Z_{\odot}$ ) in each cluster. This independence from redshift implies that there was early enrichment in clusters. Within this sample of clusters, there are two that appear as outliers for the standard categories of clusters, implying that the categories may require updates. This dataset of clusters is then reformatted into datasheets with the addition of extracting a spectrum of the size of XRISM's footprint. These datasheets are used to select candidate clusters for XRISM observation proposals. The three selected clusters are Hydra A, Abell 2199 and MS0735. This selection was done by creating upscaled simulations of CHANDRA spectra that mimic the expected properties of XRISM. The minimum exposure time required to accurately model the simulated turbulent broadening velocity was found by modelling the Fe-K complex in each cluster. The pointings and required exposure times are collected and composed into proposals to observe clusters in XRISM's A01 cycle.

To conclude the thesis, I present an initial analysis of the Virgo cluster's structure and atmospheric motions. The cluster shows a significant super-Solar abundance ratio over all metals found between 1.7 keV – 10 keV. The turbulent velocity in the cluster is low (57 km s<sup>-1</sup> – 149 km s<sup>-1</sup>) as expected from a weaker jet of  $\sim 10^{43}$  erg s<sup>-1</sup>. The bulk flow shows a small systematic blue shift over all 4 pointings, suggesting that the brightest cluster galaxy is oscillating around the center of the gravitational potential well. Narrowband observations show that the softband metals found in cooler gas move at higher speeds in most of the pointings in this cluster and have increased abundance in the southwest arm. This suggests the need for two temperature fitting in clusters and a separate study between hotter and cooler gases.

## Acknowledgments

I would like to thank my supervisor Prof. Brian McNamara for the opportunity at working with new data in galaxy clusters, guiding me into the right direction and his continuous support. I thank my committee members Michel Fich and James Taylor for their suggestions and hard hitting questions in my presentations. I would like to thank the members of the M87 XRISM team for taking me in and helping with modelling errors. I thank colleagues and friends in Brian's research group for their guidance and assistance with handling new data. In particular I would like to thank Julian Meunier and Tom Rose for our collaborative work between the XRISM teams. I thank Prathamesh Tamhane for getting me started with Chandra analysis and XRISM simulation work.

I have to thank my undergraduate friends, Erik, Ethan, Damian, Jacob, Emma, Jess and everyone else for their continuous jokes, game nights and overall support even to this day.

I would like to thank all of the professors at the University of Waterloo that taught both in undergraduate and graduate school, your knowledge culminated into me writing this thesis.

And finally, I thank my parents and my brother for listening to my ramblings about astrophysics, showing continuous love and support every single day.

# Table of Contents

<b>Author's Declaration</b>	ii
<b>Abstract</b>	iii
<b>Acknowledgments</b>	iv
<b>List of Figures</b>	viii
<b>List of Tables</b>	x
<b>1 Galaxy Cluster Background</b>	1
1.1 Hot Atmospheres . . . . .	2
1.1.1 Bremsstrahlung Emission . . . . .	2
1.2 X-Ray Spectral Components . . . . .	3
1.3 Metallicity . . . . .	5
1.3.1 SNeIa and SNeII . . . . .	5
1.4 Cooling Clusters . . . . .	7
1.5 AGN Jets . . . . .	8
1.6 Cavities . . . . .	11
1.6.1 Cavities: Uplift . . . . .	14

<b>2 CHANDRA: Galaxy Cluster Temperature &amp; Abundance Profiles</b>	<b>15</b>
2.1 CHANDRA . . . . .	16
2.1.1 Cluster ObsIDs . . . . .	18
2.2 Extracting Spectra . . . . .	19
2.2.1 RMFs and ARFs . . . . .	21
2.3 Modelling CHANDRA Spectra . . . . .	23
2.3.1 Xspec Model Components . . . . .	23
2.3.2 Model Outputs . . . . .	26
2.4 Data Analysis: Radial Profiles . . . . .	28
2.5 Data Analysis: XRISM Region & Datasheets . . . . .	37
2.6 Conclusion . . . . .	40
<b>3 Simulating XRISM Data</b>	<b>41</b>
3.1 XRISM . . . . .	42
3.1.1 Gate Valve . . . . .	44
3.2 Simulating Spectra . . . . .	46
3.3 Selecting Clusters . . . . .	48
3.3.1 Hydra A . . . . .	52
3.3.2 MS0735 . . . . .	54
3.3.3 A2199 . . . . .	55
3.4 Modelling Broadening . . . . .	56
3.5 Conclusions & Proposal Outcomes . . . . .	62
3.6 Future Work . . . . .	64
<b>4 XRISM: A Study of M87 &amp; Virgo's Intracluster Medium</b>	<b>65</b>
4.1 M87 . . . . .	66
4.2 Data Extraction . . . . .	68
4.3 Observing Metals . . . . .	68

4.4	Model Selection . . . . .	70
4.5	Data Analysis . . . . .	73
4.5.1	SPEX or Xspec . . . . .	74
4.5.2	Metallicities . . . . .	76
4.5.3	Turbulent Broadening . . . . .	78
4.5.4	Bulk Motions . . . . .	79
4.6	Jet Energetics . . . . .	81
4.7	Conclusion . . . . .	83
<b>5</b>	<b>Conclusion</b>	<b>85</b>
<b>References</b>		<b>88</b>
<b>APPENDICES</b>		<b>99</b>
<b>A</b>	<b>Chandra Cluster Datasheets</b>	<b>100</b>
A.1	XRISM Narrowbands . . . . .	100
A.2	The Datasheets . . . . .	102

# List of Figures

1.1 Components of an X-Ray Continuum . . . . .	4
1.2 HerculesA Multi-Wavelength image . . . . .	11
2.1 ACIS CCD format . . . . .	17
2.2 Abell 426 (Perseus Cluster) Summed ObsID . . . . .	20
2.3 Location of Annuli on A426 . . . . .	20
2.4 A426 RMF and ARF . . . . .	22
2.5 A426 Bapec vs Btapec model . . . . .	25
2.6 Radial Spectra of A426 . . . . .	27
2.7 Cool-core and non-cool-core cluster . . . . .	28
2.8 Abell 2029 Radial Properties . . . . .	29
2.9 A2319 Radial Properties . . . . .	29
2.10 Abell 2199 Dust Core Example . . . . .	31
2.11 Abell 2142 Flat Metallicity Cool-core Cluster . . . . .	32
2.12 Abell 3571 Intermediate Cluster . . . . .	33
2.13 Galaxy Cluster Radial Metallicity Comparison . . . . .	34
2.14 Mass and SFR comparisons to Radial Trends . . . . .	36
2.15 Metals in CHANDRA Broadband . . . . .	38
3.1 Hitomi Perseus Spectrum . . . . .	43
3.2 Gate Valve Open and Closed Simulation . . . . .	45

3.3	M87 XRISM Simulated Images . . . . .	47
3.4	Fe-K Complex Lines . . . . .	49
3.5	Hydra A Pointing Proposal . . . . .	53
3.6	MS0735 and A2199 Pointing Proposal . . . . .	55
3.7	Fe-K Multifit Model . . . . .	58
3.8	Fe-K Single-fit Model . . . . .	58
3.9	Hydra A Proposal Simulations . . . . .	61
4.1	XRISM M87 Pointings . . . . .	67
4.2	XRISM Pixel Values . . . . .	69
4.3	M87 Central Pointing Xspec Model . . . . .	72
4.4	Broadband Turbulence Comparison SPEX vs Xspec . . . . .	75
4.5	Metallicities of M87 . . . . .	76
4.6	Mass and Cooling Time Profiles of the Virgo Cluster . . . . .	82

# List of Tables

2.1	List of Clusters and ObsIDs . . . . .	18
2.2	List of Cool-cores and Non Cool-cores . . . . .	30
2.3	Cluster Data found in Datasheets . . . . .	39
3.1	Photon Counts of Simulated clusters . . . . .	51
3.2	Modelled Velocity Broadening vs True Values . . . . .	59
4.1	Narrow Band Limits on XRISM Models . . . . .	70
4.2	SPEX vs Xspec: Fe Central Pointing . . . . .	74
4.3	M87 Narrow Band Extra thermal Velocity . . . . .	78
4.4	Virgo Cluster Bulk Motion . . . . .	79
4.5	Virgo Cluster Heliocentric Bulk Motion . . . . .	80

# Chapter 1

## Galaxy Cluster Background

Galaxy clusters are the largest gravitationally bound structures in the universe. Having masses range between  $10^{14}$  and  $10^{15} M_{\odot}$ , they are composed primarily of 80% dark matter, 12% hot gas (intracluster medium (ICM)), and 8% stars [47]. These massive objects are found at the intersections of cosmic filaments [9, 47]. There are still many unknowns about how clusters form and evolve. This thesis concerns the efficiency of active galactic nuclei heating the intracluster medium, and higher than expected metal abundances being found in clusters. Most clusters contain a brightest cluster galaxy (BCG) at their centers. Since all massive galaxies are thought to host a supermassive black hole and BCGs are the largest galaxies in the universe, it is expected that they harbour the largest black holes ( $10^9$ – $10^{10} M_{\odot}$ ) [16]. When matter falls onto a galaxy’s supermassive black hole, it becomes active and emits radiation, winds and jets. Jets inflate large radio lobes [8, 103]. AGN jets and winds pump energy back into the intracluster medium, this process reheats and pushes out gas from the galaxy [116].

## 1.1 Hot Atmospheres

The intracluster medium (ICM) is a large region of plasma composed of mostly H and He pervading the entire galaxy cluster. This plasma is in hydrostatic equilibrium with the gravitational potential of the cluster. This plasma is heated to  $10^7$  K -  $10^8$  K ( $\sim 1.7$  keV) by accretion shocks [73]. Galaxy groups have cooler plasma temperatures, they will not be discussed in this thesis [73]. The cluster plasma is diffuse, having an average density of  $10^{-3}$  atoms  $\text{cm}^{-3}$  [97]. The optically thin plasma of the ICM glows in the X-ray band, with luminosities between  $10^{43}$  and  $10^{46}$  erg  $\text{s}^{-1}$  [68]. A majority of the light is produced through bremsstrahlung radiation.

### 1.1.1 Bremsstrahlung Emission

A bremsstrahlung photon is emitted during a coulomb interaction between an electron and an ion. The cross-section of this interaction scales with the amount of energy emitted, with smaller distances producing photons at higher frequencies [40].

The emissivity of thermal bremsstrahlung photons shapes the continuum of the cluster's spectrum as,

$$\epsilon_{\text{ff}} = 1.4 \times 10^{-27} Z^2 n_e n_i \sqrt{T} \bar{g} \quad \text{erg cm}^{-3} \text{ s}^{-1} \quad [95], \quad (1.1)$$

where  $Z$  is the charge of an ion,  $n_e$  and  $n_i$  are the number densities of electrons and ions respectively,  $T$  is the temperature of the gas and  $\bar{g}$  is the frequency averaged Gaunt Factor. The Gaunt Factor is a quantum mechanical correction to the cross section between the two particles. The shape of the continuum is affected by the optical depth of the projected optically thin plasma.

The spectral turnover of the continuum is set by the gas temperature. Hotter gas temperatures can emit higher energy bremsstrahlung photons. At low energies it is expected to see more bremsstrahlung photons, but due to instrumental filtration low energy photons fail to reach the detector.

## 1.2 X-Ray Spectral Components

An X-ray spectrum from a galaxy cluster's hot atmosphere contains multiple thermal components. The bremsstrahlung continuum defines the shape of the spectrum. Superposed on the continuum are emissions from recombination lines, this can explain why some photons are observed beyond the limit of maximum photoenergy.

The spikes of photon counts can be attributed to characteristic X-ray emission lines. Spectral line strengths are a function of gas density, ionization temperature and chemical abundance. The emission lines are broadened by the natural line width, thermal broadening, instrumental broadening and Doppler broadening. The natural line width is set by the Heisenberg uncertainty principle, and is usually the smallest broadening factor. The natural line width has a Lorentzian shape [38]. Thermal broadening occurs due to interactions between photon emitting atoms. Instrumental broadening is set by the spectral resolution of the instrument. Doppler broadening is due to gas motion. Thermal, instrumental and Doppler broadening have gaussian shapes around the emission line. The thermal broadening is set by the gas temperature of the cluster. The thermal component can be subtracted from the observed line profiles to measure gas motion (turbulence and gas flows). Bulk motions shift the line centers, causing the gas to appear to be at a slightly different redshift.

The X-ray spectrum of a cluster's hot atmosphere is mostly composed of bremsstrahlung continuum and spectral lines. Two other factors contribute weakly to the overall shape of the continuum: recombination lines and two photon emission. In high temperature environments, like the intracluster medium, these two components can be ignored.

Fig 1.1 shows the relationship between gas temperature and the X-ray spectrum. Bremsstrahlung emission increases in strength as the temperature of the cluster increases, since  $\epsilon_{\text{ff}} \propto T^{0.5}$  (seen in Eq 1.1). Increasing the temperature shifts the spectral turnover to higher energies, increasing the line strengths located near the turnover. At high temperatures the spectral lines will broaden due to thermal broadening, this creates wider spectral lines with a lower emissivity. At lower temperatures the strength of bremsstrahlung emission weakens, lowering the energy where the spectral turnover occurs and allowing other forms of emission to dominate. Lower temperature atmospheres can also remove high energy emission lines completely, since the environment is too cool to produce that photon.

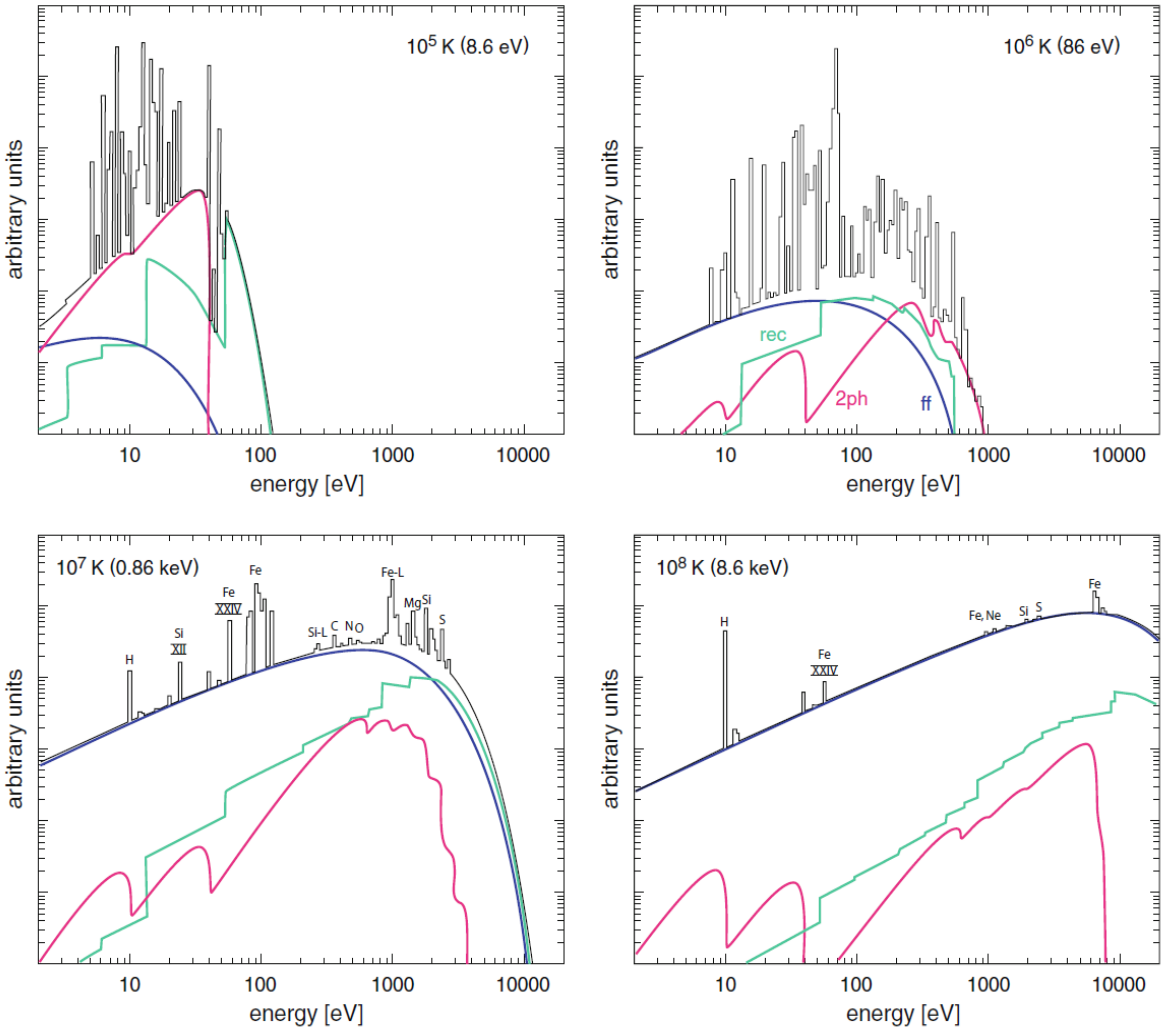


Figure 1.1: Four simulated spectra from clusters that have different temperatures. The blue line represents bremsstrahlung emission, the green line represents recombination radiation and the red line represents two photon emission. Bremsstrahlung is the dominating form of emission in high temperature regions, but recombination radiation has an effect on the upper energy values of the cooler clusters - [10]

## 1.3 Metallicity

The hot atmospheres consists of primarily ionized hydrogen (75% of gas mass), helium (23%) and other ionized heavier elements. Some of the most prominent x-ray lines found in the cluster's atmosphere include: S, Si, O, Ca, Ni, Ar, Mg, and Fe. These hot atmospheres are an optically thin plasma in ionization equilibrium. The strength of the emission lines from any atomic species is proportional to their abundance. Metal abundance of a galaxy cluster can be given as a ratio in terms of solar values, this ratio is defined as the "metallicity".

Iron produces two of the brightest line complexes in the spectrum. These complexes, Fe-L and Fe-K, form photons emitted by electron transitions to the first (K) and second (L) electron shells [17]. The Fe-L complex is located around 1 keV and the Fe-K complex is located around 6.7 keV. CHANDRA, a low spectral resolution X-ray instrument, uses these lines primarily to measure metal content in galaxy clusters. Importantly CHANDRA has a high image resolution allowing for radial metallicity measurements. The average metallicity of a hot atmosphere is  $0.3 Z_{\odot}$  [105]. The metallicity rises to near solar values ( $1 Z_{\odot}$ ) in cool core clusters. The metallicity in non-cool core clusters is constant. In most cool core clusters there is a steady rise in metallicity towards the center of the cluster, ranging from 0.5 to  $3 Z_{\odot}$  [72, 102, 105]. There are outlier cool core clusters that show a depletion in the central-most regions. Theories suggest that this sudden extinction is occurring due to ions cooling and combining with dust at the cores of clusters. These compounds would then stop emitting bremsstrahlung photons, lowering the number of detections in X-ray instruments [72, 84, 85].

### 1.3.1 SNeIa and SNeII

Atoms with higher atomic numbers such as Fe, Si, S and Mg are primarily produced by supernovae. By observing metallicity values within galaxy clusters we can calculate the frequency of past supernovae. Since galaxy clusters may be considered a "closed box", as external enrichment is rare, the history of all metal enrichment a galaxy cluster can be found through observing their spectral abundances [69]. The two main types of supernovae that will be discussed are the thermal runaway supernovae (SNeIa) and the core collapse supernovae (SNeII).

Type 1a supernovae form when a white dwarf star accretes mass beyond the Chandrasekhar limit. The dwarf star fails to produce enough electron degeneracy pressure to offset the gravitational force acting on its outer layers, causing a collapse [59, 93]. As white dwarves typically do not form with masses higher than  $1.44 M_{\odot}$  (the Chandrasekhar limit) Type 1a supernovae must occur through accretion. The most common model is a red giant and white dwarf binary system. As the red giant enlarges past the Roche limit the white dwarf accretes the mass of the red giant's outer layers. This passes the Chandrasekhar limit of the white dwarf [59]. Type 1a supernovae synthesize Fe, Ar, Mn and a subset of elements that surround the Iron peak like Cr and Ni [33, 55]. Notably Type 1a supernovae may also output Ca, Ti, V, Si and S in less prominent amounts. By observing Fe, Cr, Ni and Mn one can correlate their abundances to the number of Type 1a supernovae that have occurred in the history of the cluster.

The other common type of supernovae found in clusters are the Type II core collapse supernovae. Core collapse occurs when stars produce Fe in their core. Fusing Fe will absorb energy, being the peak in the binding energy curve, it leaves an inert Fe core. Once this Fe core reaches the Chandrasekhar limit, the electron degeneracy pressure fails to oppose gravity and the core collapses [51]. The outer layers fall onto the rebounding core, expelling energy through nuclear fusion and shedding the outer regions in a large supernova. Core collapse supernovae proceed to expel the stable alpha elements from the trapped stellar layers: O, Ne, Mg, Si and S [111]. They produce non-alpha elements including: Ar, Ca and Ni. The abundances of O, Ne, Mg, Si and S are sensitive to the number of core collapse supernovae in the cluster's history [4].

There is an issue with the current paradigm comparing abundances to the rate of supernovae in galaxy clusters. Stellar metallicities lie below the metallicity measured in the ICM, implying that galaxy clusters were enriched by early type galaxies. There had to be galaxies with iron values from 2-5 times the iron mass we see today to produce the abundance ratios seen in most clusters [4, 62]. Since Type 1a supernovae are the main process known to expel iron into galaxy clusters it would imply that such supernovae were more frequent in the early universe. Higher redshift clusters show no change to this trend suggesting that there is not a late stage influx of metals introduced into clusters. This instead supports current early enrichment theories [69, 75]. Deeper studies of metallicities in high redshift clusters with telescopes such as ATHENA may be required to truly understand how galaxy clusters have obtained this injection of metals in their early life.

## 1.4 Cooling Clusters

Two broad X-ray categories of galaxy clusters exist. Non-cool core clusters are defined as clusters that have a constant metallicity and temperature. Non-cool core clusters do not have large cooling flows, as the cooling time of its hot atmosphere is larger than the age of the cluster. Cool core clusters are defined by decreases in temperature and entropy in the centers of the cluster. Cool core temperatures decrease by a factor of 3 lower than the surrounding temperature of the atmosphere [96]. For example Abell 2199 has an ICM temperature of 4.7 keV ( $5.4 \times 10^7$  K) in the outer regions of the cluster, whilst the inner core drops to a temperature of 2.2 keV ( $2.5 \times 10^7$  K) [values from the datasheets]. It is believed that “cooling flows” is the mechanism responsible for these cool cores.

Over time the plasma cools from the continuous emission and its density increases. These denser regions move towards the center of the cluster. This continues until the plasma reaches hydrostatic equilibrium. This process is repeated throughout the cooler/lower entropy regions at a higher rate as the entropy is proportional to cooling time. The cooling time is given by:

$$t_{\text{cool}} = \frac{p}{(\gamma - 1)n_e n_H \Lambda(T)}. \quad (1.2)$$

Within Eq. 1.2 p is the gas pressure,  $\gamma$  is the adiabatic index, and  $\Lambda(T)$  is the cooling function. As the entropy of the ICM plasma drops it lowers its gas pressure; this shows that the cooling time shortens for denser gases. Enrichment occurs within a region about 100-150 kpc from the center of the cluster [88]. This can explain the higher than expected rates of star formation in BCGs. Since the BCG is located in a metal-rich environment, it would accrete more metals than standard galaxies, which increases the star formation rate [113].

## 1.5 AGN Jets

The cooling time for the plasma in the central cooling region is less than 1 GYr [69]. Classical cooling flow models predict that 100-1000  $M_{\odot}$  of cooled gas should accumulate per year in the central galaxy [28]. As observed cooling rates are not as high as classical models imply, there has to be a heating mechanism that offsets cooling faster than the cooling time within the core of a cluster.

The leading sources of reheating are the BCG’s active black hole and relativistic jets. The excess cooled gas around the AGN accretes onto the central black hole. Some of this gas may pile up into an accretion disk around the black hole, this process produces large relativistic radio jets. These jets emitted from the AGN output energy into the surrounding environment in the order of  $10^{53}$  erg  $M_{\odot}^{-1}$  [116]. The process of relativistic jet emission and its underlying mechanisms are still poorly understood. The Blandford–Znajek process, posits that a Kerr black hole twists the magnetic field formed by the plasma within its accretion disk. This action of winding magnetic fields converts rotational energy into large relativistic jets [8, 103]. Jets are launched along the spin axis of the black hole. These jets can bend under the influence of their environment; some mechanisms that can cause this are galactic winds and bulk motion. As a particle coils along the jet it emits magnetobremsstrahlung radiation [37].

The jets emit synchrotron radiation in the radio band. This causes some jets to be invisible to X-ray telescopes such as XRISM and CHANDRA. The effect the jet has on the surrounding ICM is crucial as the expansion of the radio jet pushes the gas surrounding it. This means that pressure of the jet pushes away the gas from the core, lifting the cooler gas from the center out into the warmer outer regions of cluster.

In MS0735.6+7421 jets were seen out to 170 – 180 kpc from the core [101]. Most of the entrained gas in the jets is still within the metal-enriched core, but the jets become diffuse and expand into lobes 200 kpc across [68]. This portion of the jet passes the cool core threshold, which implies that some of the cooled gas from the core has successfully reached a warmer environment. This lifted cooler gas will then be heated through thermal conduction.

Jets heat through work, lifting low-entropy gas up into regions with higher entropy, while also injecting their own kinetic energy into the surrounding environment creating a shock front. This injection of energy creates a low-density region of hot gas; these are called cavities because of their initial circular shape and buoyant nature. Cavities are X-ray features that stand out in cool core clusters since a cavity lowers the luminosity of the region to 40% below the surrounding ICM [27, 69]. The amount of energy within each cavity is equivalent to the energy of the radio lobe, in addition to the work required to

inflate the cavity against the pressure of the surrounding ICM. The energy requirement to produce a cavity is equivalent to its enthalpy [104]. This simplifies into an equation which calculates the overall energy to produce a cavity with a set volume.

$$E_{\text{cavity}} = H = E_{\text{jet}} + pV \quad (1.3)$$

$$E_{\text{jet}} = \frac{1}{\gamma - 1} pV \quad [69] \quad (1.4)$$

Within the Eq 1.3 and 1.4  $p$  is the pressure of the ICM,  $V$  is the volume of the inflated cavity and  $\gamma$  is the adiabatic index. Usually the radio lobes inflating the cavities are considered to be dominated by relativistic particles, meaning that the adiabatic index is equivalent to  $1.3$  which equates to  $4pV$  [7]. This is the standard for initial cavity production. There also is an adiabatic index for generating a cavity with non-relativistic gas, this is equivalent to  $1.6$  which equates to  $2.5pV$  [104]. This comes from the assumption that the hot atmosphere is composed of monoatomic gas, where the particle only has 3 degrees of freedom [20]. There is a third case where cavities are dominated by magnetic fields instead of relativistic and non-relativistic particles, for this the enthalpy of the radio lobe is equivalent to  $2pV$  [69]. As they are under the influence of multiple factors the true enthalpy of the radio lobe will usually be found between  $2pV - 4pV$ . With this value the power of a cavity may be defined by comparing the calculated enthalpy of the cavity and the overall age of the cavity.

$$P_{\text{cavity}} = \frac{E_{\text{cavity}}}{t_{\text{cavity}}} \quad (1.5)$$

AGN jets are not instantaneous events. After the initial outburst a jet may continue to inject energy into the surrounding ICM for thousands of years. This means that the ICM is continuously being reheated with an expanding cavity at the end of this jet. This explains how MS0735.6+7421 has produced a pair of cavities with a radius of at least 200 kpc [68]. To find the actual energy output of the AGN we use an equation relating luminosity to the mass accreted by the AGN:

$$L = \epsilon_r \dot{M}_{\text{acc}} c^2 = 5.7 \times 10^{45} \left( \frac{\epsilon_r}{0.1} \right) \left( \frac{\dot{M}_{\text{acc}}}{M_{\odot}} \text{ year}^{-1} \right) \text{ erg s}^{-1} \quad [106]. \quad (1.6)$$

Here  $\epsilon_r$  is defined as the radiative efficiency, a coefficient relating to the accretion rate of the black hole and the type of accretion disks that may form, usually  $\leq 0.2$  [56, 106]. The luminosity and output energy is defined by the mass accretion rates and the rotation

speed of the Kerr black hole. The AGN can be characterized by two different modes of feedback: quasar mode, occurring only if the AGN is considered radiatively efficient and radio mode, where the AGN is considered radiatively inefficient which emits large radio jets [106]. This thesis will discuss radio mode feedback, its energy injection rate is defined below:

$$\dot{E}_k = \epsilon_{f,k} \dot{M}_{acc} c^2 = 5.7 \times 10^{46} \epsilon_{f,k} \left( \frac{\dot{M}_{acc}}{M_\odot} \text{ year}^{-1} \right) \text{ erg s}^{-1}, \quad (1.7)$$

$\epsilon_{f,k}$  is defined as the efficiency of the kinetic energy coupling driving the outflow around the hot gas atmosphere. Recent simulations show that this value may range between  $10^{-3} - 0.08$  depending on rotation speeds [49, 115, 114]. Since some jets last more than 1 Myr the total injected energy provided by them is extreme. As an example PKS 1138-262 has a pair of jets that have been injecting their energy into the surrounding ICM for  $2 \times 10^7$  years, at a rate of  $5 \times 10^{46}$  erg s $^{-1}$  [12, 116]. The total energy the jets deposit into the surrounding atmosphere would be a total of  $\epsilon_{f,k} \times 3.154 \times 10^{61}$  ergs, assuming an accretion rate of  $1 M_\odot$  per year. These large energy pumps inflate a pair of cavities in the surrounding atmosphere to restart the heating cycle.

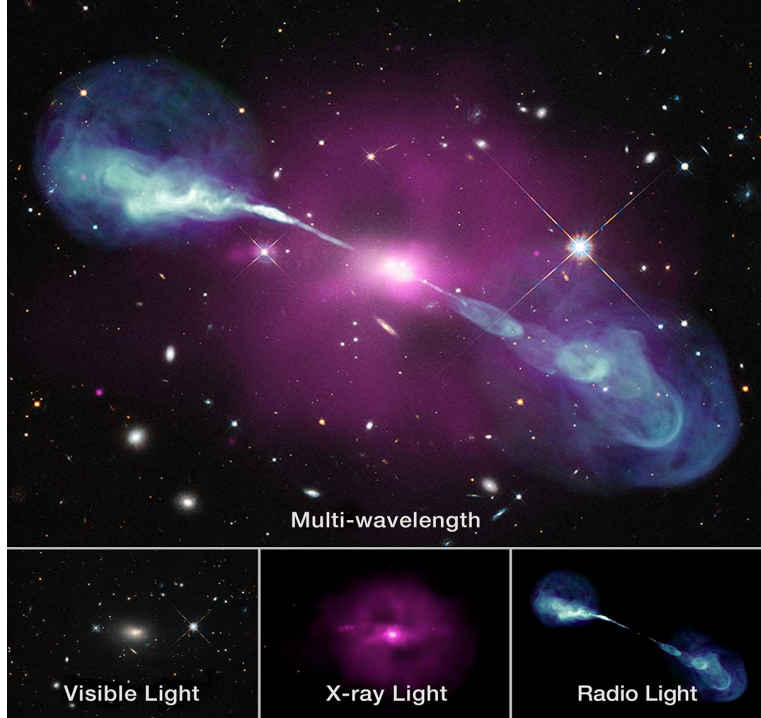


Figure 1.2: HerculesA multi-wavelength image with bright radio jets. The optical wavelength data is provided by the STScI, X-ray produced by Chandra, and Radio produced by the NRAO VLA

## 1.6 Cavities

Cavities are regions of low density gas found in the hot atmospheres of cool core clusters. They are produced by the introduction of high powered jets into a convectively stable environment. Through continued injection the jet produces an expanding elliptical region of a lower density plasma, with a higher density cool gas surface that envelopes the edges of the cavity [66]. This system can be considered as a buoyant bubble; it is a low-density gas enveloped by a higher-density surface in an environment with a density gradient. The cavity rises buoyantly in the cluster as a result of the pressure in the atmosphere. This may decouple the cavity from the AGN jet, allowing it to “float” further than the jet’s influence. Many cavities appear to be formed from older jets and still continue to rise well after they stopped firing. This can create multiple cavity pairs in clusters, which can be seen in HydraA, a cluster that has at least 3 cavity pairs. The motions of these cavities affect the gas velocity structure and the dispersion of metals within the ICM.

The age of a cavity is inversely proportional to its power (Eq. 1.5). The age of a cavity can be defined by the distance ( $R$ ) from the BCG and its terminal velocity ( $\nu_{\text{term}}$ ).

$$t_{\text{cavity}} = \frac{R}{\nu_{\text{term}}} , \quad (1.8)$$

As the cavity distances are projected onto the sky, this is a minimum timescale, assuming all cavities are moving along the plane of the sky. Deprojecting the cavities will increase the distance from the BCG, which in turn increases the age of the cavity.

Cavities are not expected to be stable objects; most bubbles are prone to multiple instabilities. For instance, ram pressure, Rayleigh–Taylor and Kelvin–Helmholtz instabilities can affect a cavity while forming and after it decouples.

Ram pressure acts as a drag force against the motion of a cavity rising through the core of a cluster. It can deform and strip the edges of a cavity, flattening the spherical regions as they rise through the cluster [41]. Stripping the edge of a cavity will destroy the cavity as the environmental inflow fills the low-density region. The strength of ram pressure is calculated using the density of the atmosphere ( $\rho_e$ ) and the velocity of the cavity ( $\nu$ ):

$$P_r = \rho_e \nu^2 [41]. \quad (1.9)$$

The cool gas envelope between the hot atmosphere of the cluster and the low-density region inside a cavity can be treated as a fluid interface. Fluids of different densities flowing past each other experience Rayleigh–Taylor (R-T) and Kelvin–Helmholtz (K-H) instabilities. The face of the cavity that experiences ram pressure will experience R-T instabilities, while the sides parallel to the motion of the cavity and its wake experience K-H instabilities [15, 53]. The wake of the cavity will form eddies due to K-H instabilities, increasing the turbulent motions of gas behind a cavity. This should increase the velocity broadening in x-ray emission lines in the inner regions found behind the cavities.

Over long timescales, the R-T and K-H instabilities should grow to destroy cavities. The equations for the growth time of both Rayleigh–Taylor and Kelvin–Helmholtz instabilities are shown below:

$$t_{\text{KH}} = \frac{\lambda_h}{\Delta\nu} \frac{(\rho_L + \rho_H)^2}{\rho_L \rho_H}, \quad (1.10)$$

$$t_{\text{RT}} = \sqrt{\left( \frac{\lambda_h}{2\pi A|g|} \right)} [23]. \quad (1.11)$$

$\lambda_h$  is defined as the size scale of the instability,  $A$  is the Atwood number (a value defining the shape of the R-T instability),  $\Delta\nu$  is the velocity difference between the cavity and the bulk motion,  $\rho_L$  is the density of the cavity,  $\rho_H$  is the density of the environment, and  $g$  is gravitational acceleration. These timescales are well below observed ages of cavities; some cavities would not be able to exist for more than 5 Myr in some clusters. With these short instability timescales there must be a component in cavities that resists both forms of instabilities [23]. The current prevailing theories of processes that offset both Kelvin–Helmholtz and Rayleigh–Taylor instabilities are: cavity expansion [87], magnetic field lines [63], and viscosity [43, 91, 94].

The timescales of R-T instabilities suggest that cavities would be destroyed before they decouple from radio jets. The cavity inflation has been theorized to be strong enough to dampen the effect of R-T instabilities [57]. Inflation creates a drag effect on the growth rate of R-T instabilities, akin to Hubble drag dampening the perturbations in the Universe’s expansion [87]. The location in which the cavity is produced can also effect its lifetime, as the initial cavity radius is inversely proportional to the density of the surrounding ICM and low density environments decrease the Atwood number [24]. The inflation of cavities is finite, implying cavities will succumb to R-T instabilities at longer timescales. Cavity inflation only weakens R-T instabilities, they do not change the timescales of Kelvin–Helmholtz instabilities.

Tangled magnetic fields are found in cavities, the fields are produced by AGN jets through the Blandford–Znajek process [58, 79]. Simulations injecting cavities into an environment with weak magnetic fields show that R-T and K-H instabilities dominate the cavity. In simulations where the magnetic fields are strong (over  $1 \mu\text{G}$ ) the instabilities are significantly quenched [52, 71]. Diehl (2008) suggests that observed cavities are similar to bubbles that were produced by an inflation of a chaotic bundle of magnetic field lines which bolster against environmental perturbations [23]. These magnetic field lines weaken instabilities over the entire lifecycle of cavities unlike inflation.

Viscosity is a late stage component that offsets the effects of both forms of fluid instabilities. Simulations were run with and without a viscosity component: without viscosity cavities devolve into “torus-like” objects and dissipate, with viscosity cavities retained shape [42]. Viscous dissipation can also be used as a method to carry energy throughout the cluster in longer timescales, providing another source of heating. The slow heating and cooling of a viscous fluid may also explain why a cool envelope of the hot atmosphere continues to surround cavities [91].

### 1.6.1 Cavities: Uplift

The efficiency of the heat pump created by the motions of cavities defines the longevity of galaxy clusters. A cavity will carry gas up as it buoyantly rises through the cluster while also pulling up gas through its trailing outflows. These outflows will deposit some gas along the wake providing linear filament structures behind each cavity [25]. These two processes mechanically lift metal-rich parcels of gas within the cluster to distant metal-poor regions. The total metallicity of the outer regions of a galaxy cluster increases due to metal enrichment from the cooled out core. If cavities deposit this cooled metal-rich gas at a consistent radius then there should be a peak in metallicity not directly at the core of the cluster. An abundance turnover does occur within several clusters shown in the datasheets in the appendix, the known clusters that show this peak in metallicity are: A426, A2199, AWM7, Centaurus, HydraA and Ophiuchus. Other sources such as M. Gendron-Marsolais (2017) have found this drop and peak feature to exist in more clusters [34]. The decrease of metallicity in the core may be an effect of dust combination with cooled out ions, thus the metallicity turnover is not necessarily from cavities removing and depositing cooled gas in the same region.

It can be difficult to trace where uplifted metals originated in the cluster, therefore simulations of cavity gas displacement have been created. These simulations can extract information on the energy efficiency of a single cavity, since this process is where energy is used to transport and (re)heat gas. If this process is found to be energy inefficient galaxy clusters will cool down over time and will not be able to perpetually reheat themselves through thermal conduction. Chen's (2019) simulations show radial gas particle positions can be traced back to their starting position [14]. Cavities emulate geothermal heat pumps, a heated fluid enters the core, and the cooled fluid is pushed up to the outer edges of the cluster to be reheated [14]. There is no work expended lifting the gas against gravity because of buoyancy; the gas gains energy by being lifted into a heated environment. When the gas is lifted beyond the hot regions of the cluster, it will have a negative thermal energy budget because it emits heat into the cooler environment.

This is the solution to the galaxy cluster cooling catastrophe, as the heat is recycled using cavities as an efficient geothermal heat pump-like process that offsets the cooling produced by thermal radiation. Cavities deposit metal-rich parcels of gas into metal-poor regions at specific radii, and this deposit location is dependent on the initial radial position of the gas. To observe the increase in metal abundance around cavities and regions where the gas is deposited, high spectral and angular resolution X-ray telescopes are required. Although CHANDRA can be used to observe annular radii around the cluster, its spectral resolution is somewhat poor ( $\sim 95$  eV), XRISM has the opposite issue wherein the angular resolution is poor but the spectral resolution is cutting edge ( $\sim 5$  eV).

## Chapter 2

# CHANDRA: Galaxy Cluster Temperature & Abundance Profiles

*This chapter includes original research, using data from the publicly available CHANDRA X-Ray Observatory database, it also includes mass data produced by Mike Hogan to normalize the radii. All X-ray data within this chapter was analyzed and produced by Neo Dizdar unless stated otherwise.*

Comparing structural differences between cool-core and non-cool-core cluster atmospheres requires a high spatial resolution X-ray database. CHANDRA, a high spatial resolution low spectral resolution X-ray telescope, contains the largest database of cluster spectra available to the public. By using CHANDRA images I create radial metallicity, temperature and cooling time curves for several galaxy clusters. The profiles are then compared to observe common trends between cluster types. Other values may be extracted from a CHANDRA spectrum such as the cluster X-ray luminosity and photon counts from the Iron-K complex. Radial metallicity trends between clusters may be used to study dusty cores, abundance dispersion and the metallicity floor in the outer regions of a cluster. Within this chapter I reformat CHANDRA images into datasheets that contain the radial curves to compare between clusters. I also extract spectra and create datasheets using XRISM's Resolve footprint to create baselines for future data.

## 2.1 CHANDRA

CHANDRA is an X-ray telescope that was deployed in 1999, with its mission designed around observing high-energy X-ray data from clusters and other X-ray sources. The CHANDRA’s ACIS (Advanced CCD Imaging Spectrometer) has a spectral bandpass between 0.2 keV – 10 keV and a spectral resolution of 95 eV. This spectral resolution causes the X-ray emission lines to blur into large Gaussians, covering many other weak lines, and causing some metals to become unresolved. CHANDRA’s ACIS imaging resolution is 0.5 arcsec and a total field of view of 16.9 x 16.9 arcmin (Wide Field Mode) or 8.3 x 8.3 arcmin (High Resolution Mode) [35].

CHANDRA’s ACIS instrument has 10 CCDs in two configurations, ACIS-I and ACIS-S. ACIS-S appears as a straight line of 6 CCDs. ACIS-I is a set of four CCDs in a 2x2 square offset from ACIS-S by 163 arcsec [81]. ACIS-I does not have any back illuminated CCDs; this lowers this configuration’s energy resolution. Most exposures contain six CCDs, four CCDs from the selected configuration, and two CCDs from the other configuration. The two CCDs are used for background flare removal, filtering out non-ICM emission from the images, allowing for clearer imaging.

Each CCD is separated by a small gap, causing blank spots in the images. The approximate size of the chip gaps is shown in Fig 2.1, the ACIS-I gaps are larger than ACIS-S. To reduce the effect of these blank spots appearing in the images, multiple exposures were taken with different roll angles (or different pointings) and stacked. Images taken with the ACIS-I configuration are particularly affected by the CCD spacing, as the spacings are larger and that configuration usually is used for large angular size clusters. This creates a large dark cross in the most large non-cool-core cluster images.

The CHANDRA X-Ray Observatory provides one of the most extensive X-ray databases. The database contains a large amount of ACIS images for many clusters with high image resolution and usable spectral resolution. This can create large-scale studies of temperature and metallicity profiles between different varieties of clusters. To access and use these data, a tool is provided: CIAO (CHANDRA Interactive Analysis of Observations) which requires the observation ID (or ObsID for short) to extract data from the database. It is suggested to use more than one observation for robust results, as it will increase the signal-to-noise ratio on each object.

# ACIS FLIGHT FOCAL PLANE

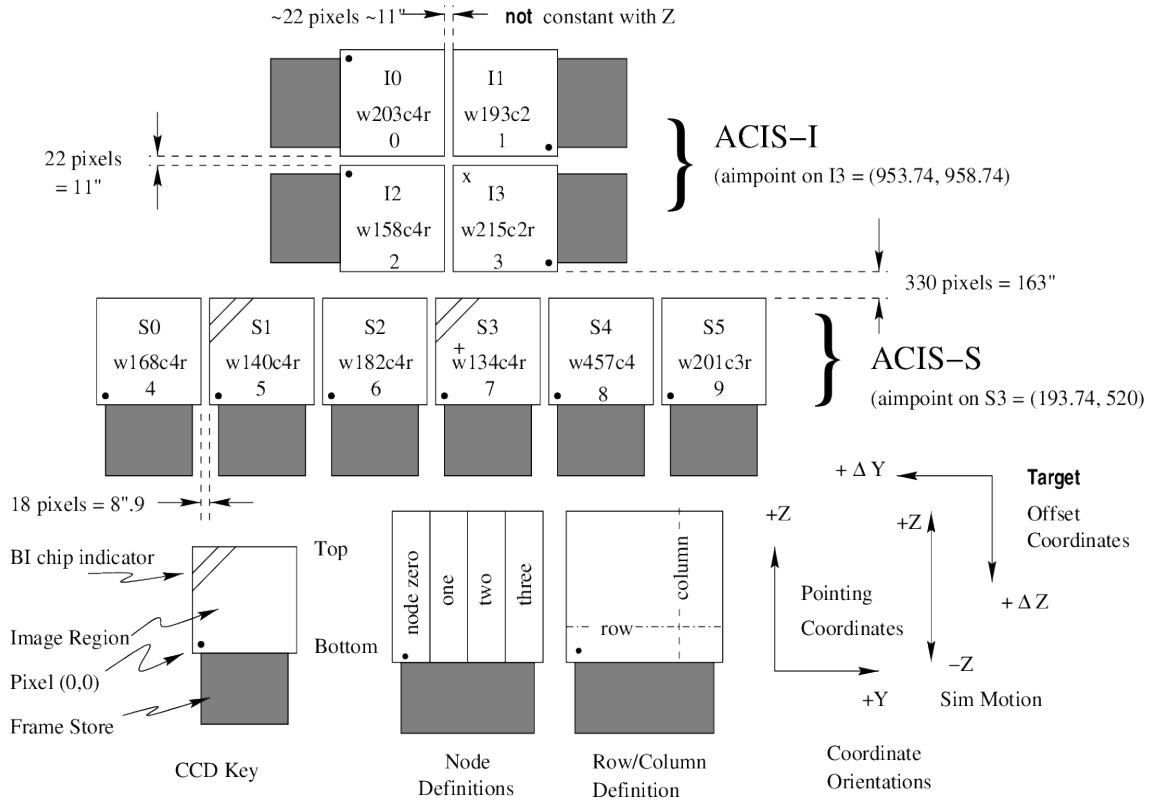


Figure 2.1: A diagram showing the format of CHANDRA's ACIS instrument. The double lines in the top corners of the chip denote a Back illuminated chip. [81]

### 2.1.1 Cluster ObsIDs

ObsIDs of Clusters used	
Cluster	ObsID
Abell 426	1513, 3209, 4289, 4946, 4947, 4949, 6145, 11713, 11714
Abell 478	1669, 6102
Abell 754	577, 10743
Abell 2029	891, 4977, 6101
Abell 2142	5005, 7692, 15186, 16564, 16565
Abell 2199	497, 498, 10748, 10803, 10804
Abell 2319	3231, 15187
Abell 3571	4203
Abell 3667	889, 5751, 5752, 5753, 6292, 6295, 6296, 7686
AWM7	908, 11717, 12016, 12017, 12018
Centaurus	504, 505, 4954, 4955, 5310, 16223, 16534, 16608, 16610
Coma	9714, 10672, 14406, 14411
CygnusA	6226, 6228, 6229, 6250, 6252
HydraA	576, 4969, 4970
MS0735	4197, 10468, 10470, 10471, 10822, 10918, 10922, 16275
Ophiuchus	3200, 16142, 16143, 16464, 16626, 16627, 16633, 16634, 16635, 16645

Table 2.1: The clusters shown were used to produce cluster datasheets, the ObsIDs given can be found in CHANDRA’s database and are available for use by the public

The clusters were selected using multiple criteria: number of observations, number of research papers, or being a known non-cool-core cluster. There are certain images of clusters that did not load properly and had to be removed. This leads to some clusters (Abell 3571, Abell 2319 and Abell 754) having only one or two observations (ObsIDs), causing a lower signal-to-noise ratio and increasing uncertainties in photon counts. The uncertainties propagate further to metallicity and temperature calculations, as modelling these values are based solely on source-photon counts. This chapter discusses a dataset of 16 known clusters, each of which will have their own datasheet created that will contain temperature, abundance, and cooling time profiles. These datasheets are found in the appendix of the thesis.

## 2.2 Extracting Spectra

CHANDRA spectra are extracted through the use of CIAO tools from files in the CHANDRA database. The images initially are in separate ObsIDs and must be reprojected, aligning data to a singular point in the sky. Background subtraction is done by using blank-sky images to disentangle the background and low luminosity ICM photons. The blank sky images account for vignetting and readout lines within the telescope. If done correctly blank sky subtraction produces images with clear distinctions between the background noise and the extended object.

Background subtraction will highlight point sources in and around the galaxy cluster. Point sources like background stars and galaxies may pollute the spectrum and need to be removed for studies of the cluster's atmosphere. They can be removed with instruments that have high spatial resolution, like CHANDRA's ACIS, but will affect missions with low spatial resolution, like XRISM, as point sources become unresolved. To emulate XRISM data for Chapter 3 this process must be repeated while including point sources. CHANDRA's tool for finding point sources (`wavdetect`) scans the image for Ricker wavelets, the Laplacian of a Gaussian function, and highlights point sources for removal [108]. Point sources are widened by a point-spread function file attached to the image. This function then generates a list of point sources with their luminosity values. However, extracting photons from regions containing point sources can be ignored.

To obtain radial profiles of a cluster the image must be subdivided into smaller regions. A relaxed cluster may be approximated to be spherical. Therefore radial profiles can be made by extracting data in concentric annuli centered on the BCG. The rest of the rings are produced by counting the number of photons in a circular area outward until a predetermined photon limit is reached, in this thesis each annulus representing 3000 photons. This produces scaled bins by photon counts with varying annulus width, with the smallest annulus near the BCG and the outermost regions in the ICM having the largest annuli. The radius of the inner and outer edges of each annulus is stored with its own separate spectrum. Modelling the spectrum extracted from each annulus and attaching an average radius produces a radial profile of a cluster.

Each annulus turns its pixel photon counts into .pi files. A .pi file is used to convert photon count data into a histogram producing a distribution of photon counts in terms of energy channels. This process uses the known exposure time of the image and divides the total photon count in an energy channel by exposure time. These energy channels require a function to convert them into energy values. This conversion is done by an RMF (redistribution matrix file) and an ARF (ancillary response file).



Figure 2.2: This is an image of all of the ObsIDs of Abell 426 overlapped, the CCD gaps are very noticeable in this image due to it being taken at a log photon counts scale.

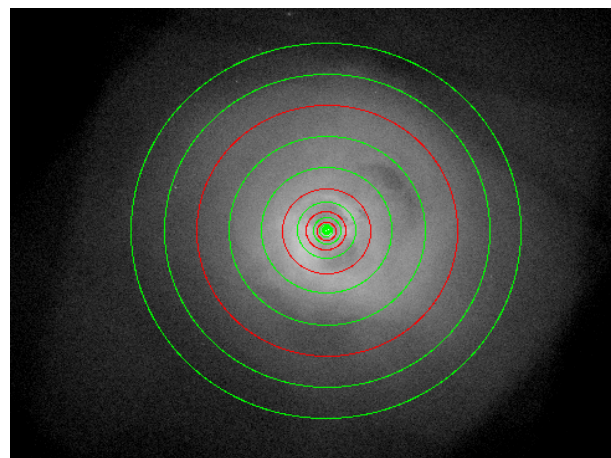


Figure 2.3: Radial Annuli around Abell 426, red annuli are extracted and presented as spectra in Fig 2.6.

### 2.2.1 RMFs and ARFs

A redistribution matrix file (RMF) maps a photon's pulse height to the energy value of a detector. This spreads photon counts over the resolution of the detector through matrix multiplication. Each detector requires a different response matrix function, and as a detector degrades over time, these response matrices change. It is suggested that an RMF should be produced every time a new observation is made. A response matrix will appear as a linear relationship that relates energy channels and photon energy in high-resolution instruments [19]. The ACIS detectors do not have a perfect diagonal relationship, being affected by escape peaks and low-energy tails. These features only affect the energy extremes of the detector [86].

An ancillary response file (ARF) describes the combination of the effective area of the instrument and the quantum efficiency of the instrument, mapping the efficiency of each pixel in the detector. One component of an ARF measures the effect of vignetting on the CCD, where the peripheral pixels on the CCD become dimmer. The quantum efficiency of an ARF is the fraction of detected incoming photons over the total number of photons reaching the detector [77]. The quantum efficiency of ACIS is strong (near 100%) between 0.5 keV – 10 keV but weakens significantly (below 10%) below 0.1 keV [54].

Instruments may have pixels that are failing, these pixels must be removed and ignored as to not contaminate data. Other CCDs may also have a chip turned off to use as a calibration pixel. This requires updating the ARFs with corrected chip regions, as pixels that are removed can change the instrument's effective area.

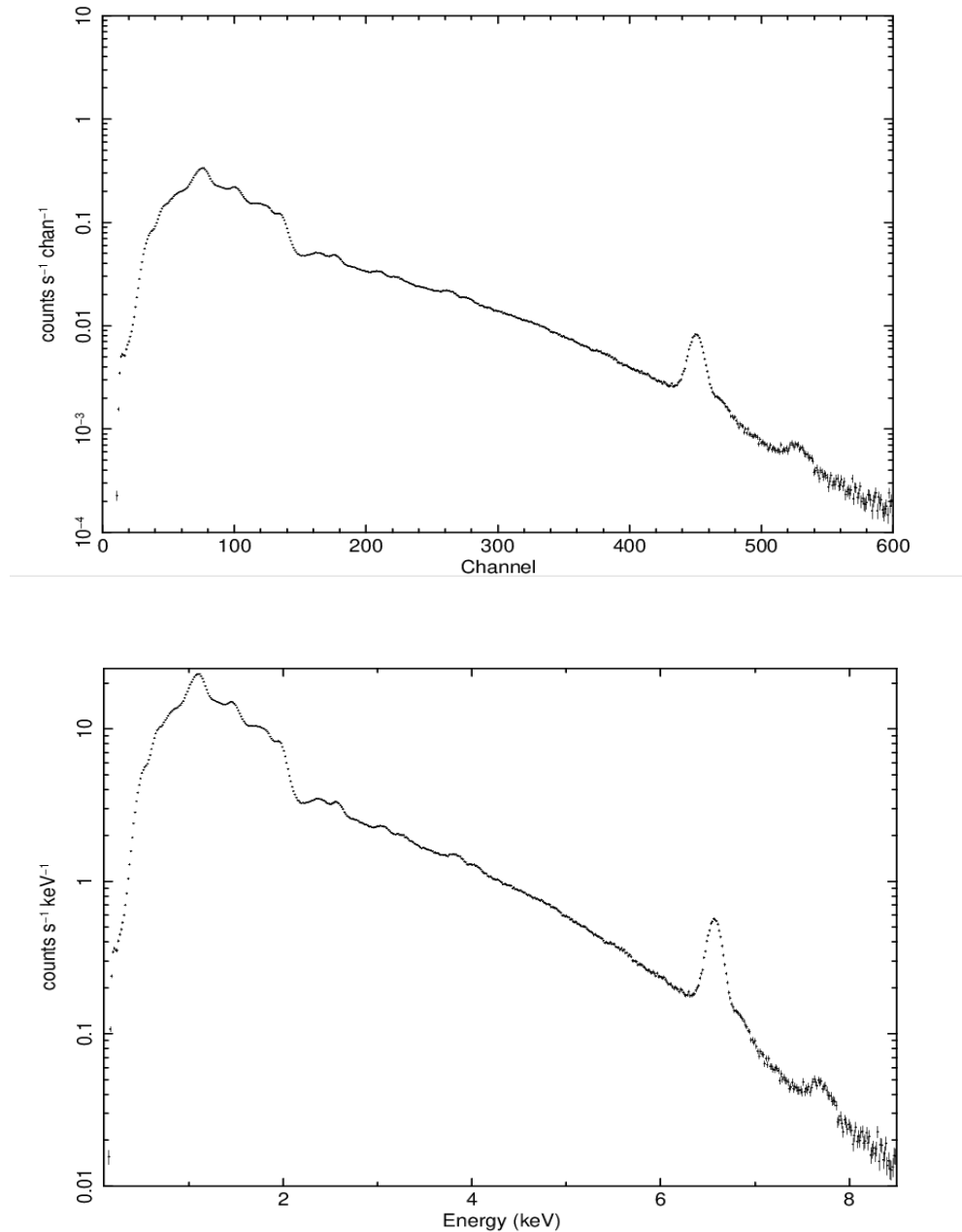


Figure 2.4: This is a spectrum of the Perseus cluster using CHANDRA, the upper image is the raw .pi file while the lower image is the spectrum, corrected and calibrated using the RMF and ARF files. The axis changes from channels to energy values (keV).

## 2.3 Modelling CHANDRA Spectra

With RMF and ARF corrected data, a model may be fit onto the spectrum, extracting metallicity, temperature, turbulent velocity, and redshift from the image. These models start with random initial parameters and use the  $\chi^2$  statistic to decrease the residual between the data and the model. Xspec, a model fitting tool made by NASA’s HEASARC, is used to create the models within this chapter. This tool is the standard for modelling emission spectra in X-ray astronomy. In Chapter 4 XRISM data will test both Xspec and SPEX, another tool made by SRON, to observe any major differences.

The bandpass of CHANDRA’s ACIS instrument is 0.5 keV – 7 keV, data outside of this range will be ignored while modelling. To calculate the metallicity of a cluster, a model must use metallicity tables that relate photon counts to solar abundance values. There are multiple metallicity tables with different values used in the field, the two most common are those of: Andres and Grevesse (1989) [2] and Lodders (2003) [61]. In this chapter the Andres and Grevesse abundance table will be used. The models also must include the current cosmological parameters to convert redshift into distance, which in this thesis are:  $H_0 = 70 \text{ km s}^{-1} \text{ Mpc}^{-1}$ ,  $\Omega_M = 0.3$  and  $\Omega_\lambda = 0.7$ .

### 2.3.1 Xspec Model Components

Xspec supports multiple different model components that may be combined to produce full spectra. These components have five categories: additive components, multiplicative components, convolution components, pile-up components, and mixing model components [3]. The models created in this chapter only use additive and multiplicative components. Additive components represent sources of emission and are the only component required to produce a model. Multiplicative components apply transformations on the additive component, only applying a flat transformation per energy bin.

The two Xspec components used are `apec`, an additive model component, and `phabs`, a multiplicative model component. The models are named in the format of “multiplicative \* additive” as an example the first model is: `phabs*apec`. `apec` (Astrophysical Plasma Emission Code) is a model that contains data of more than  $10^6$  different X-ray emission lines stored in the AtomDB database. This component measures the emissivity of both the X-ray emission lines and the continuum [99]. It assumes that the object observed (the ICM) is a hot optically thin plasma in collisional ionization equilibrium. `apec` is composed of 4 different parameters, these are temperature, metallicity, redshift, and normalization. The temperature is defined as the plasma temperature of the ICM in terms of keV (1 keV  $\simeq 11.6 \times 10^6$  K). The metallicity of the `apec` model is a combination of elements between

carbon and nickel as a single total metallicity in terms of solar abundances. The redshift is a frozen parameter of the BCG's redshift, found in NASA's Extragalactic Database [46]. If the redshift is left to vary, the computing time for model generation increases exponentially. The normalization is defined as:

$$norm = \frac{10^{-14}}{4\pi(D_A(1+z)^2)} \int n_e n_H dV. \quad (2.1)$$

$D_A$  is the angular diameter distance to the cluster,  $n_e$  is the electron density and  $n_H$  is the hydrogen density. **apec** has several variants, these are **bapec**, **vapec**, **vvapec** and **btapec**, each represents an **apec** model with additional parameters. **bapec** has a parameter for velocity broadening in X-ray lines, providing a broadening  $\sigma$  in terms of  $\text{km s}^{-1}$ . **vapec** contains 13 additional parameters, each representing abundances of elements between He - Ni, the abundance parameters are in terms of Solar metallicity. **vvapec** can adjust all metal abundances up to Zn, both **vapec** and **vvapec** can be combined with a velocity broadening parameter named **bvapec** and **bvvapec** respectively. Finally, **btapec** is a two-temperature + velocity broadening model, where the X-ray continuum and emission line temperatures are separate parameters.

**phabs** is a multiplicative model component that represents photoelectric absorption with one parameter: the projected hydrogen density ( $n_H$ ) through a column of the ICM.  $n_H$  is the only other parameter that is frozen, found by using HEASARC's H column density tool. The **phabs** model is a scalar variable defined by this equation:

$$M = \exp^{-n_H \sigma(E)}. \quad (2.2)$$

$\sigma(E)$  is the photoelectric effect cross section, the cross section where a ray and an atom interact. **phabs\*bapec** and **phabs\*btapec** produces most of the models within this chapter. Some models require the addition of a powerlaw emission component, an additional additive component that accounts for the nonthermal photons produced by the AGN. The clusters that contain a powerlaw component are Perseus and Centaurus.

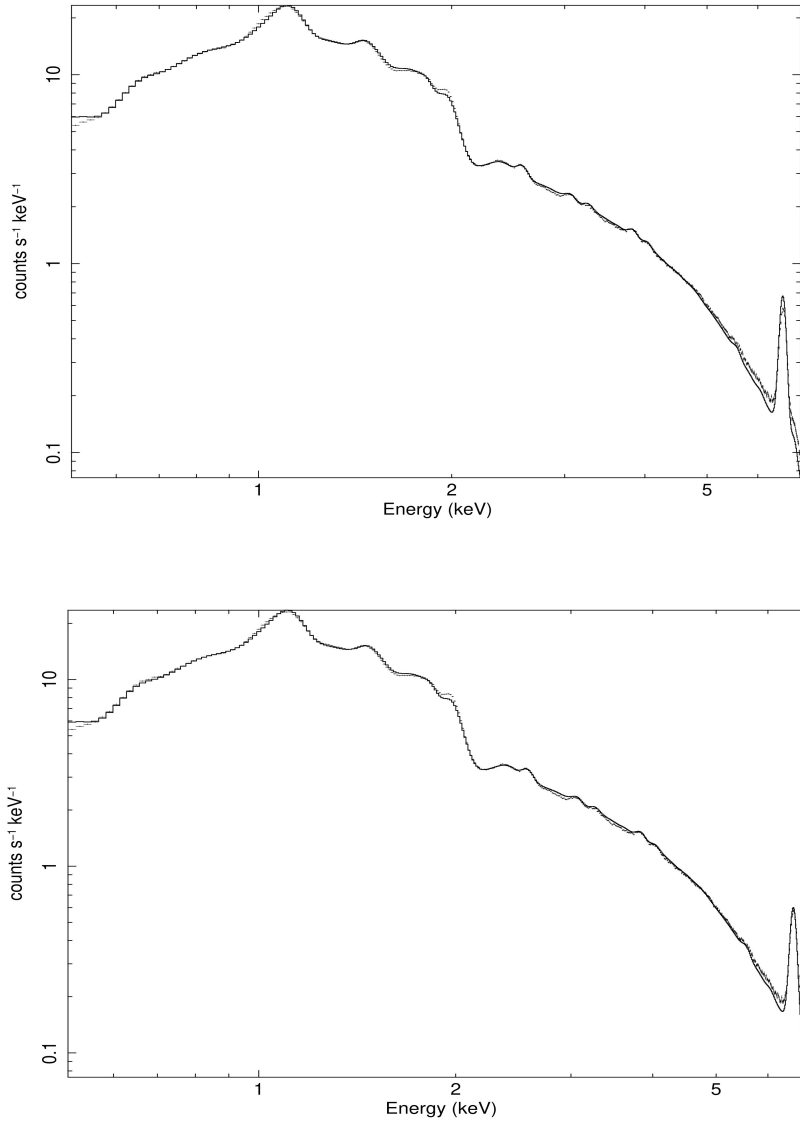


Figure 2.5: Spectra obtained from Abell 426, attempting to use two models bapec (upper) and btapac (lower), the data appears as points with error bars whilst the model is the black stepped line. As observed, the 2-temperature model is more accurate at matching the Iron-K data peak.

### 2.3.2 Model Outputs

Each cluster has spectra extracted from radial annuli regions and a XRISM Resolve footprint centered on the BCG ( $2.9 \times 2.9$  arcmin square). Two models, `bapec` and `btapec`, are tested on these annular regions. The model configuration was selected based on the residuals between the data and the model. In many cases a two-temperature model is not needed, but for clusters like Abell 426 as shown in Fig 2.5 `btapec` is used instead to align with the Fe-K complex. Each model outputs three important values: radial metallicity, radial temperature, and the photon counts.

Photon counts are important, as they can be used to calculate the flux in different energy bands, for example: the continuum can be isolated around the Iron-K peak, providing only Fe-K photons. This allows observations of flux from other visible metals in the spectrum, but Fe-K is predominantly used over bright low energy lines (like Fe-L) since Hitomi and XRISM cannot resolve data below 1.8 keV. Photon counts over emissions cannot distinguish between bremsstrahlung photons and photons in the emission line. These bremsstrahlung photons must be removed to accurately measure the abundance of the metal producing the emission line. This is done by observing photon counts of two energy values near the broadened emission line, usually in a small bin (0.5 eV width), then applying a linear interpolation of the slope between the edges of the broadened line. Over small ranges this becomes sufficiently close to being a straight line. The amount of photons under this straight slope is calculated and removed from the total photon count; the remainder represents emission line photons. This process was repeated in regions near the Fe-K complex that do not contain a resolved emission line. This provided extremely low photon counts, which can be considered noise. This suggests that assuming the background continuum under an emission line is a straight slope is justifiable and will not affect the emission line photon count.

The final product extracted from the model is the cooling time. The cooling time is found by measuring the photon counts, temperature and radius of the region. These values are converted into the gas cooling time using the equation below:

$$t_{\text{cool}} = \frac{\frac{5}{2}nkT}{L} \frac{4\pi (r_{\text{outer}}^3 - r_{\text{inner}}^3)}{3} [26]. \quad (2.3)$$

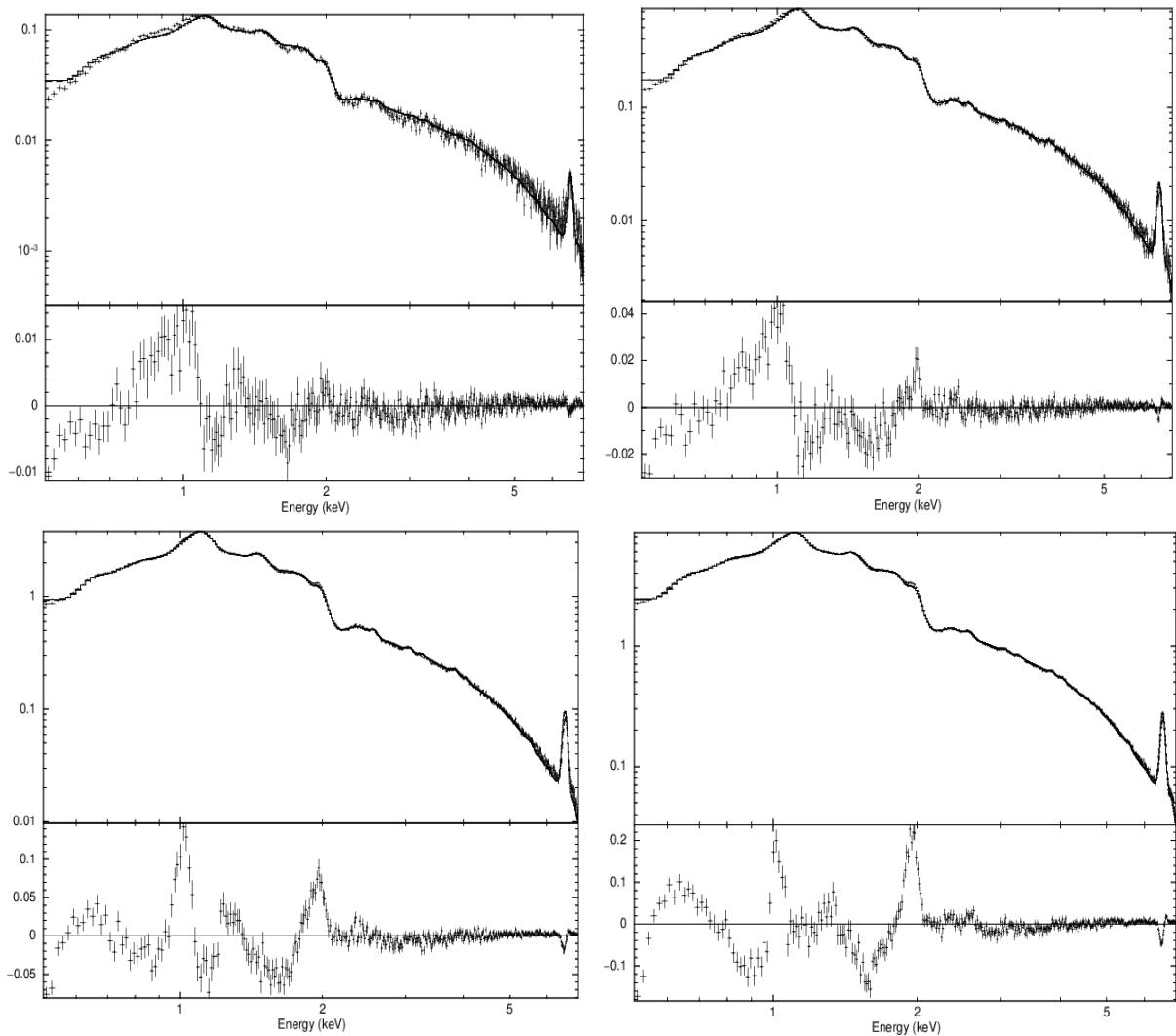


Figure 2.6: Four spectral annuli of A426, each consecutive annulus is at a higher radius. The lower graphs are the residuals between data and model.

## 2.4 Data Analysis: Radial Profiles

Modelling the extracted spectra from the concentric annuli correlates the model parameters to the radius of the cluster, producing radial profiles of metallicity, cooling time and temperature. These radial profiles can trace increases or decreases in abundance and temperature throughout the cluster. Predominantly, this is attributed to metallicity, as this allows one to trace increases and decreases throughout the cluster. Radial temperature trends are expected to show temperature decreases in the inner regions of cool-core clusters and no temperature changes in non-cool-core clusters. The metallicity in cool-core clusters is expected to increase in the inner regions while it is expected to be flat in non-cool-core clusters. The cooling time is proportional to the temperature, volume, and pressure of the system. Cool-core clusters are expected to show a decrease in temperature and volume in the inner radii, suggesting that the cooling time also decreases. The cooling time of non-cool-core clusters should decrease as well as the volume dominates the equation while temperature is constant. This implies that non-cool-core clusters may have small cooling flows occurring near the central-most regions of the cluster. Categorically cool-core and non-cool-core clusters have key visual differences, as cooled cores have a higher luminosity than the surrounding cluster, which can usually be defined by visual inspection, as seen in Fig 2.7.

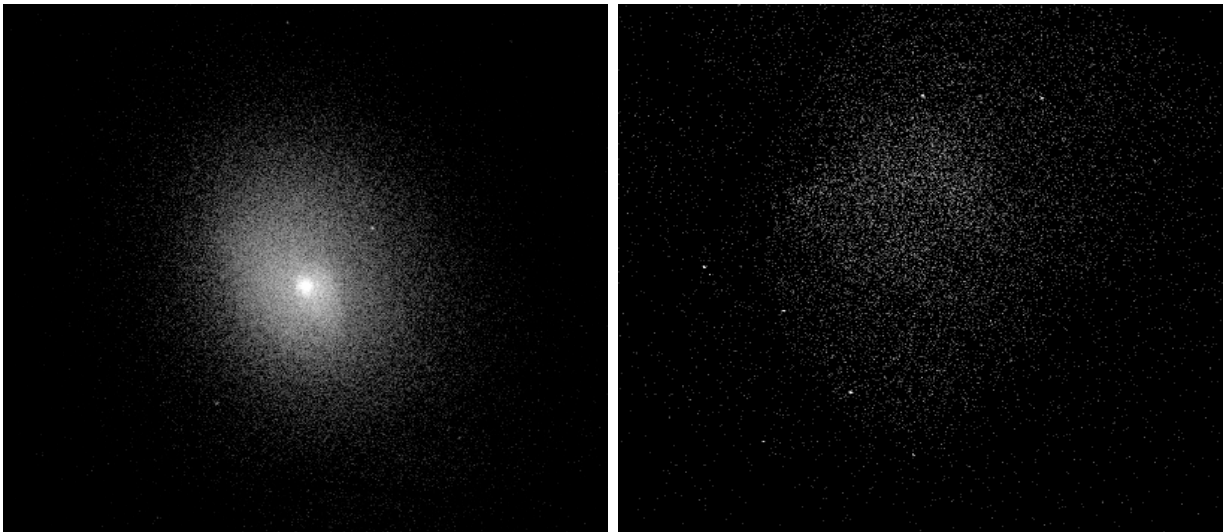


Figure 2.7: (**Left**) Abell 2029 - a cool-core cluster, the luminosity increases towards the core. (**Right**) Abell 2319 - a non-cool-core cluster, a dim cloud of X-ray emitting photons.

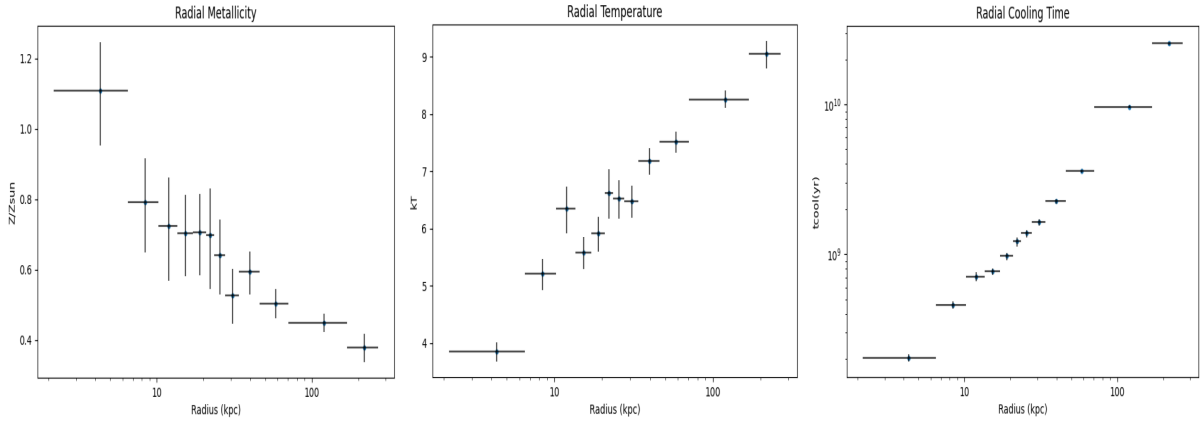


Figure 2.8: The metallicity, temperature and cooling time profiles of Abell 2029. Cool-core clusters show an increase in metallicity, decrease in temperature and decrease in cooling time towards the core.

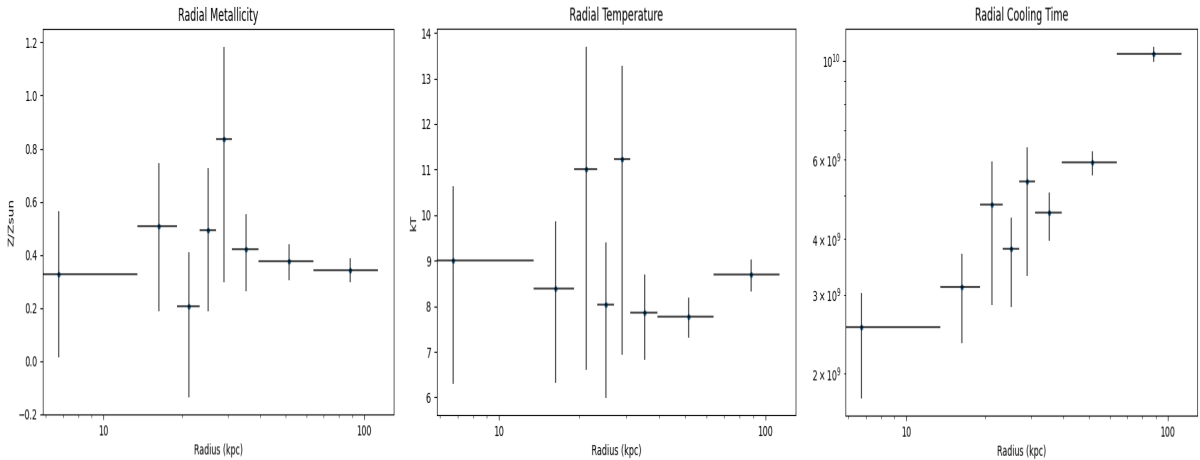


Figure 2.9: The metallicity, temperature and cooling time profiles of Abell 2319. Non-cool-core clusters have flat metallicity and temperature profiles while the cooling time decreases towards the core.

Types of Clusters in Dataset	
Cool-core	Non-cool-core
Abell 426*	Abell 754
Abell 478	Abell 2319
Abell 2199*	Abell 3571*
Abell 2029	Abell 3667
Abell 2142*	Coma
AWM7*	
Centaurus*	
CygnusA	
HydraA*	
MS0735	
Ophiuchus*	

Table 2.2: This is the total list of clusters that have had their radial data measured, the marked clusters with \* have unexpected profiles for their classification.

Four out of 11 cool-core clusters in Table 2.2 provide expected radial profiles, where metallicities increase closer to the core of the cluster, the temperature, and the cooling time both decrease toward the core. All of the 16 clusters reach a metallicity value of  $0.3 Z_{\odot}$  in their outer regions. There are 6 cool-core clusters in this dataset that show signs of a “dusty core” and one cool-core cluster that has a flat metallicity gradient. Cool-core clusters are defined by hot gas in collisional ionization equilibrium becoming cooler towards the center of the cluster; therefore, it is expected that each cool-core cluster shows that the hot atmosphere temperature decreases at lower radii.

Abell 426, Abell 2199, AWM7, HydraA, Ophiuchus, and Centaurus all show a sudden decrease in metallicity in the regions around the center of the cluster. This opposes the expected trend where metallicity increases towards the center of a cool-core cluster. This change in metallicity may be caused by dust particles in cluster cores. Cooled ions can combine with dust grains, these compounds do not emit X-ray photons, which appears as a depletion of metal abundance in X-ray instruments [72, 85]. Since Ar and Ne are inert and are less likely to form dust compounds, measuring their abundance ratios and comparing them to the rest of the metals can be used as a signifier of dust-to-metal depletion occurring. There is a form of molecular gas with  $\text{ArH}^+$  but it is unlikely that this gas can form in cluster atmospheres [72]. Dusty core clusters are defined by an increasing abundance of Ne and Ar, while the other metals decrease in the center of the cluster. The characteristic lines of Ar and Ne are weak and are difficult to distinguish from the bremsstrahlung continuum. With CHANDRA’s spectral resolution, attempting to measure their abundance profiles will

provide large errors. Future missions with XRISM and ATHENA may improve confidence in this theory as the spectral resolution of those instruments can make many noble gas emission lines visible. The decrease in metallicity may also be caused by turbulent inner regions which displace metal-rich gas. Abell 426, Abell 2199, HydraA, and Centaurus all show a turbulent inner region where large cavities are forming near the core, previous cavities may drag out the metals and deposit them at higher radii. The clusters that have this decrease in metallicity near the core also have a metal “peak” which could be the radius where cavities may deposited the cooled out metals. Beyond the peak the metallicity decreases rapidly towards  $0.3 Z_{\odot}$  in the outer regions.

Abell 2142 is a non-standard cool-core cluster with a flat metallicity profile. It appears to be a dim extended cluster with a flat metallicity profile, a common trait of a non-cool-core cluster, but the temperature profiles show cooling towards the cluster’s core. This cluster may be a link between cool-core and non-cool-core clusters. The abundance profile of Abell 2142 may be caused by external factors such as sloshing, as a large shock front is found in the cluster, or a recent merger event that influenced the metallicity in the core [22, 21]. For a deeper examination on A2142 future studies should extract spectra specifically from the shock front in the cluster, under the assumption that it contains the displaced gas in the system.

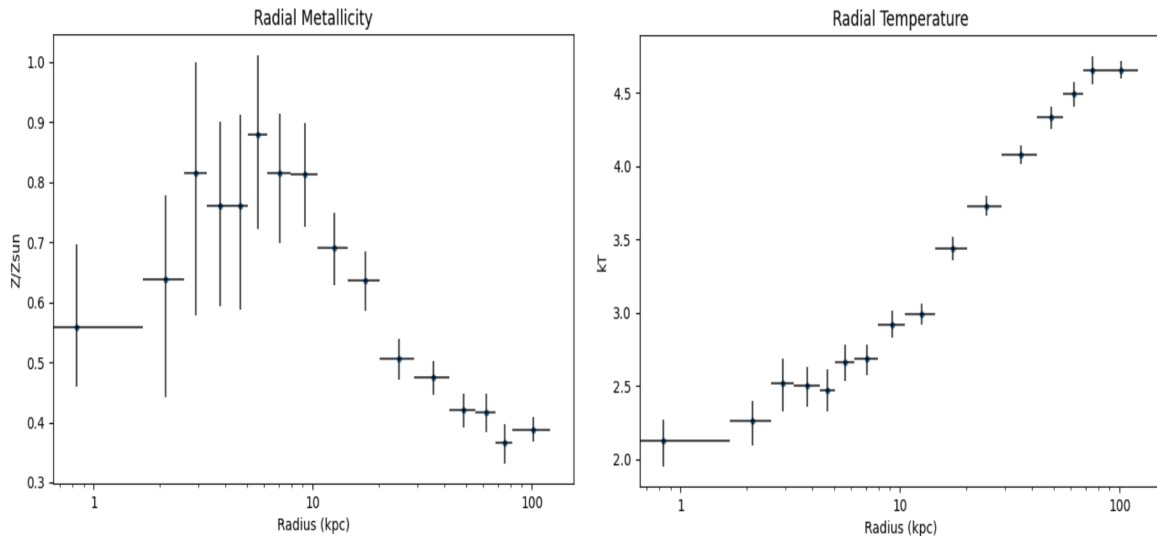


Figure 2.10: Abell 2199, shows signs of metal depletion in its core, radial temperature acts like a cool-core system.

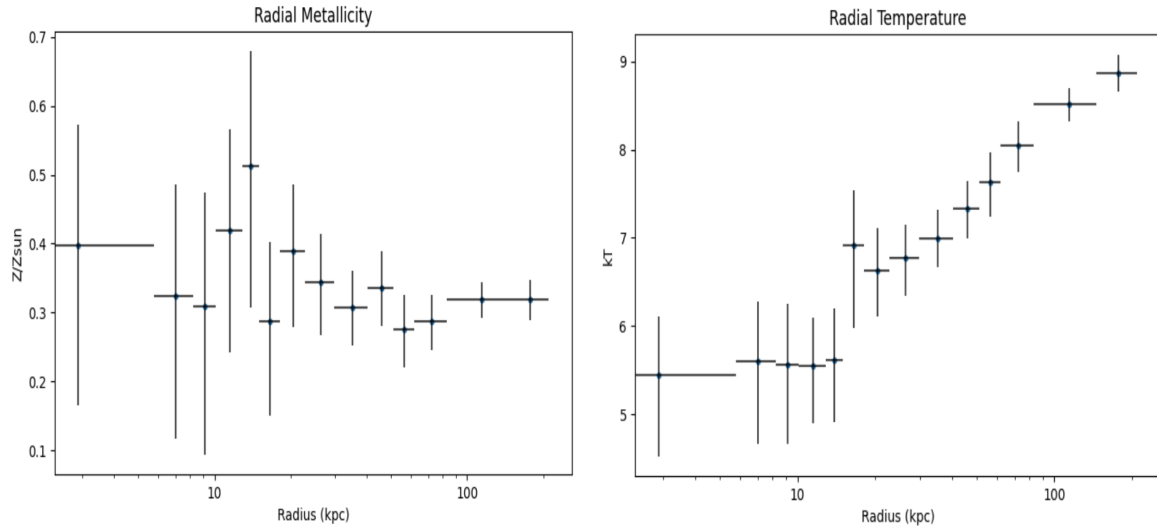


Figure 2.11: Abell 2142, shows a flat metallicity trend, similar to a non-cool-core system, but radial temperature decreases inwards like a cool-core system.

Abell 3571 is one non-cool-core cluster that does not align with expected radial profiles. Its metallicity profile slowly increases towards the core of the cluster, similar to a cool-core cluster, but the temperature profile appears to be flat. This cluster has had multiple papers discussing its classification; some theories suggest that it is an “intermediate” cluster converting into a cool-core cluster as it contains a cool-core remnant [50, 92, 107]. In the radio and optical bandpasses the cluster has an asymmetrical galaxy distribution, implying external effects such as a merger. The x-ray bandpass shows a quiescent cluster, relaxed to the point where a cooling flow begins to form [107]. This may be related to the two other clusters in close proximity. These two clusters are Abell 3572 and Abell 3575; they appear so close together that they spatially overlap in the sky, causing observations of Abell 3571’s hot atmosphere to be influenced by the other clusters. This may explain why the cluster looks like it has a higher metallicity in its core. Abell 3571 has a unique non-cool-core cluster metallicity profile unlike the other four non-cool-core clusters.

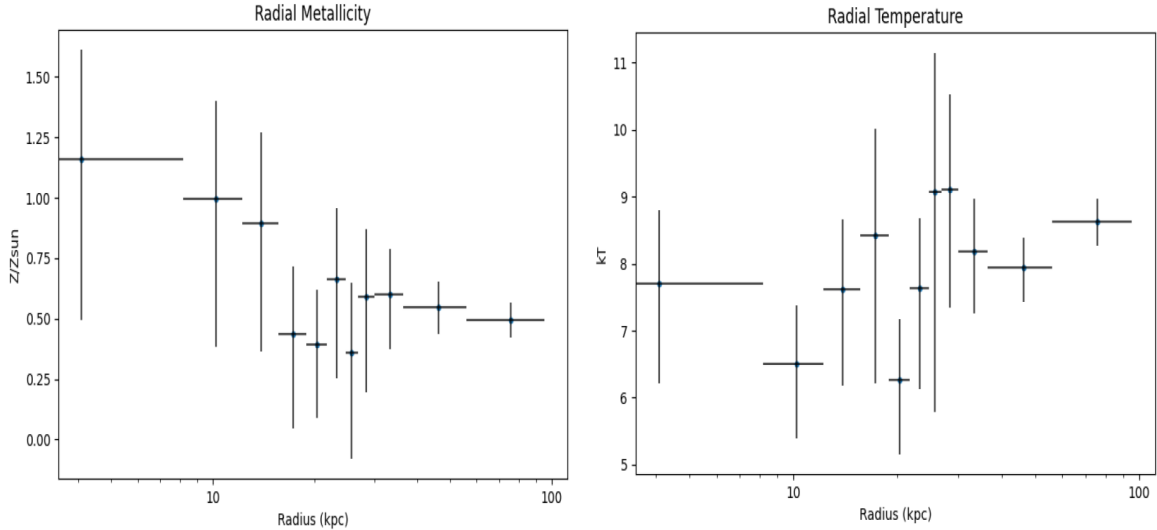


Figure 2.12: Abell 3571 shows signs of metal accumulation in its core, radial temperature slightly decreases towards the center, between cool-core and non-cool-core.

Both cool-core and non-cool-core clusters have an abundance of  $0.3 Z_{\odot}$  in their outermost regions, and by plotting the metallicity profiles together it may show other trends between cluster types. Some cool-core clusters have showcased a characteristic metal depletion near their cores. This depletion may exist in most cool-core clusters. Clusters that do not have dusty core metal depletion may just be too dim (or distant) to resolve these features in the overall radial profile. Therefore radial profiles may need to be normalized to the cluster's size. Since a cluster's edge is poorly defined the virial radius is used instead. The virial radius is a defined distance in which the encapsulated region has a density equivalent to the critical density of the universe:  $\sim 3 \times 10^{-26} \text{ kg m}^{-3}$ . This radius would encapsulate the entire visible cluster and much of the surrounding empty space in CHANDRA images. The radial profiles of a galaxy cluster may require a smaller unit of measurement:  $r_{2500}$ .  $r_{2500}$  is a radius that encapsulates an area of space that has a density equivalent to 2500x the critical density. The value for 2500x the critical density is defined as:

$$\rho(< r_{2500}) = 2500\rho_{\text{crit}}(t) = 2500 \frac{3H^2(t)}{8\pi G} \quad (2.4)$$

The virial radius of a cluster requires the mass of the cluster. The masses of clusters can be calculated by modelling a cluster with two mass components, an NFW model and an isothermal model. This process was already completed by Pulido (2017), Hogan (2017) and Comis (2011) [18, 48, 89]. Their datasets were used to define the  $r_{2500}$  for each available cluster. If a cluster's  $r_{2500}$  was not available in these datasets then the cluster is not used in Fig 2.13 and Fig 2.14. Clusters missing from these datasets are: Abell 426, Abell 754, and Coma and will not be available for structural comparisons. This lowers the available clusters to a total of 13. Future work should focus on expanding this dataset to all well-known clusters.

Most clusters appear have their metallicity decreasing to  $0.3 Z_{\odot}$  beyond a radius  $0.5 r_{2500}$ . The clusters in this dataset span between  $0.01 z$  and  $0.54 z$ , this asymptotic decrease to  $0.3 Z_{\odot}$  being independent to redshift implies that clusters must be formed with a higher metallicity content than previously predicted. Mantz (2017) shows that this trend extends to clusters with redshifts of up to  $1.2$  [64].

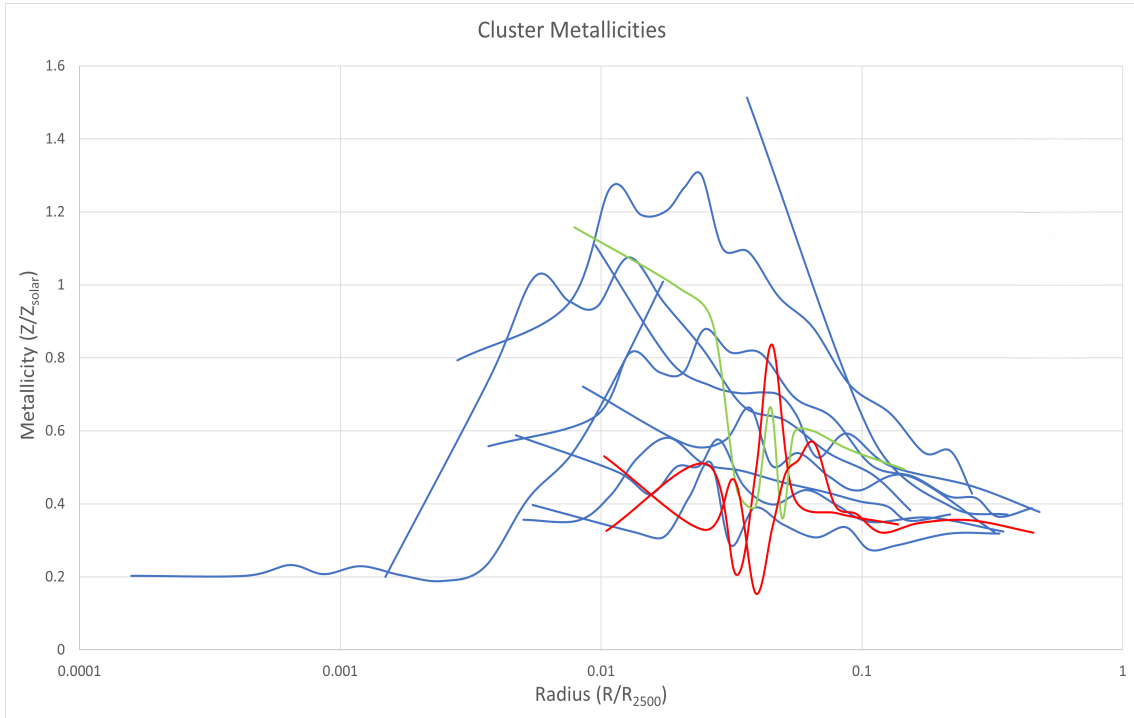


Figure 2.13: Radial cluster metallicities, cool-core clusters are represented by blue lines, non-cool-core clusters are represented by red lines and the "intermediate cluster" Abell 3571 is represented by a green line.

The metallicity profiles of non-cool-core clusters fluctuate around  $0.3 Z_{\odot}$ , flat profiles are expected from these clusters. Cool-core clusters appear to have a peak in metallicity between  $0.008 - 0.05 R/R_{2500}$ . At a radius of  $0.5 r_{2500}$  the cool-cores reach an abundance of  $\sim 0.3$ . Some larger cool-core clusters that have their innermost regions spatially resolved by CHANDRA show metallicity depletion at the core of the cluster. The largest clusters have abundances that fall below  $0.3 Z_{\odot}$  in these inner regions. The metallicities dropping below  $0.3$  may hint to other sources of metal depletion like dust grains, or metal displacement due to cavity uplift.

Other observations may be made by comparing radial abundance profiles to each cluster's mass and stellar formation rate [48, 67]. As the datasets do not fully contain all of the clusters observed the missing clusters will be removed for these comparisons. As seen in Fig. 2.14 there are no visible trends between the mass of the cluster (within  $r_{2500}$ ) and metallicity. The non-cool-core clusters are at opposite ends of the mass scale; while the cool-core clusters appear to be spread equally through the entirety of the scale. The stellar formation rate is obtained by McDonald (2018) [67] by observing the optical line luminosity of H $\alpha$ , UV flux, and the  $24 \mu\text{m}$  flux. The stellar formation rate values are given in logarithmic format, with SFR being the total amount of solar mass produced per year. As seen in Fig. 2.14 the stellar formation rate rarely exceeds  $1 M_{\odot}$  per year, with CygnusA being an extreme outlier containing a strong AGN. Centaurus appears to have the lowest star formation rate within the subset of clusters. Clusters with the highest metallicity peaks are on both ends of the stellar formation rate scale; there are no clear trends between stellar formation rate and metallicity in the cluster.

Errors may be found while extracting metallicity or temperature values in the central regions of clusters. The first source of error occurs with galaxy clusters that have very bright cores. The point source removal algorithm may fail to remove the AGN causing an increase in metallicity and temperature as AGN photons mix with the photons produced by the ICM. The other error occurs due to the pixel gaps in ACIS-I instrument. The location of the clusters imaged in this mode tends to be closer to the edge a chip, leading to a physical gap in photon information over 22 pixels. This occurs in extended non-cool-core clusters like the Coma cluster, as all 4 ACIS-I chips are used to capture the full cluster in one image. The Coma cluster's center is located near the intersection of the four ACIS-I chips. This causes the inner annulus to be larger than most clusters, which increases the radial error bars within both the temperature and the metallicity graphs.

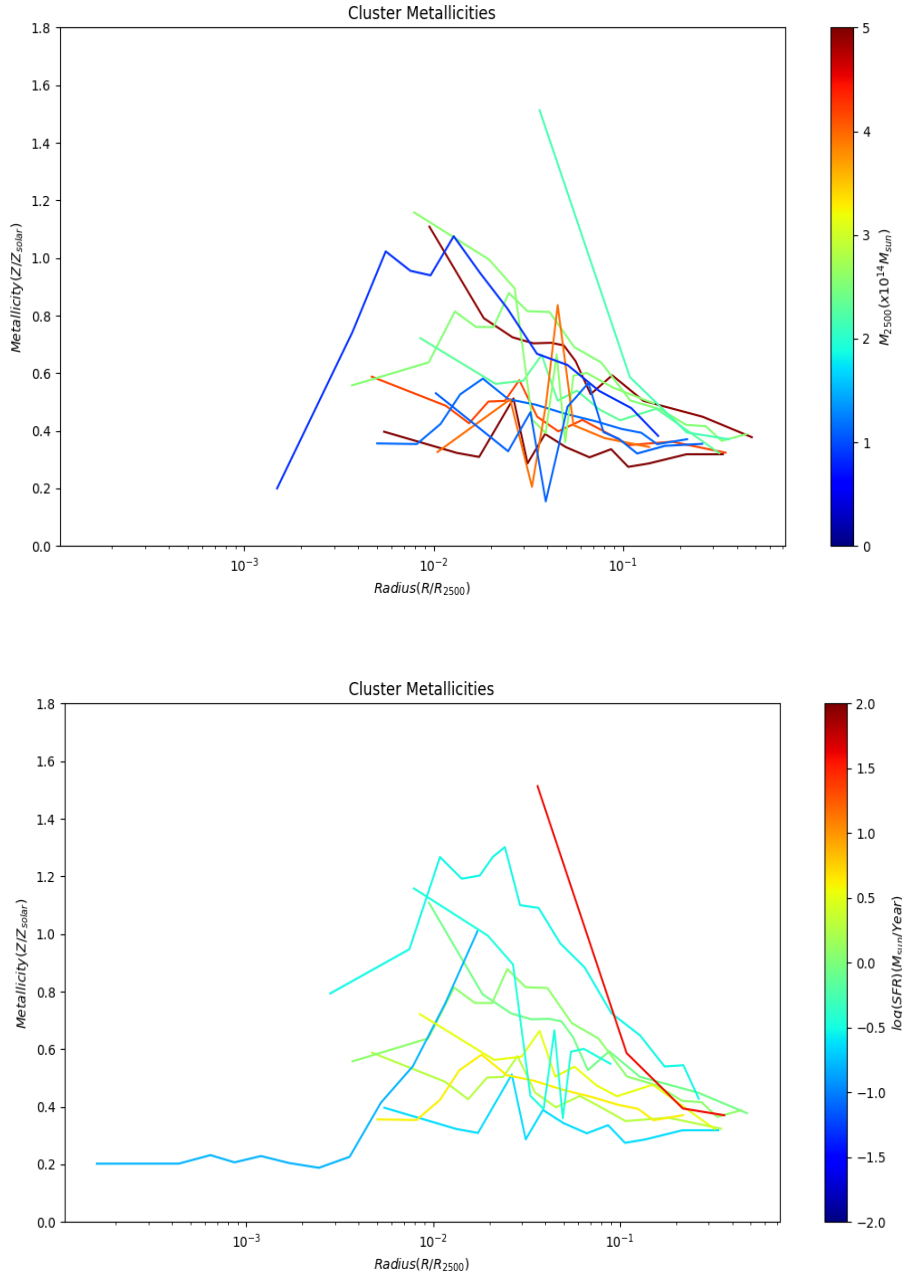


Figure 2.14: Galaxy cluster radial metallicity trends comparing between the cluster's mass (top image) and the cluster's star formation rate (bottom image). Data for these clusters were taken from Hogan (2017) and McDonald (2018) [48, 67].

## 2.5 Data Analysis: XRISM Region & Datasheets

Modelling can be repeated on a broadband spectrum of a cluster in the dimensions of XRISM’s Resolve footprint in anticipation for XRISM’s launch. Resolve’s footprint is a square with dimensions of 2.9 x 2.9 arcminutes; the region is centered on a cluster’s BCG for each cluster in the dataset. This spectrum provides an overall temperature, extrathermal velocity and metallicity which can be used to compare to values found by XRISM in the future. This can not observe structural changes within the cluster since it produces one spectrum of a large central region. This can extract the expected total luminosity of the inner region and the total photons emitted by different metals visible in the spectrum.

To obtain photon counts of each metal narrowbands must be defined in the spectrum to only cover its x-ray emission lines. The metals observed (in addition to the Fe-K complex between 6 keV – 7 keV) were the Mg-K alpha and beta complex spanning between 1.3 keV – 1.5 keV, the Si-K complex found at 1.8 keV – 2.4 keV, the S-K complex found at 2.4 keV – 2.9 keV, the Ar-K complex found between 3.1 keV – 3.4 keV, and finally the Ca complex found between 3.8 keV – 4.5 keV. The Mn and Cr complexes were too dim for any cluster to properly differentiate between their emission lines and the background continuum. These narrowbands will be used in Chapter 4 to measure abundances of different metals in M87. The results of Iron-K counts are used during the selection process for clusters that should be observed by XRISM, which will be expanded on in Chapter 3.

This data is reformatted into datasheets to highlight important information in the clusters. Key cluster values are: temperature within the region, the total exposure time required to produce the spectrum, the total number of photon counts, the average metallicity within the region and the specific flux of the Iron-K complex. The data found from the XRISM Resolve region and the radial profiles of each cluster can be compiled into a datasheet. These datasheets can be used as resources to compare CHANDRA values (such as the temperature, metallicity and flux) to XRISM findings. They can also be used as a resource to highlight outlier clusters, such as clusters with high metallicity, high temperature or odd radial profiles. Having values like high metallicity may provide target clusters for studies of early enrichment scenarios. Each datasheet may be found within the appendix of this thesis.

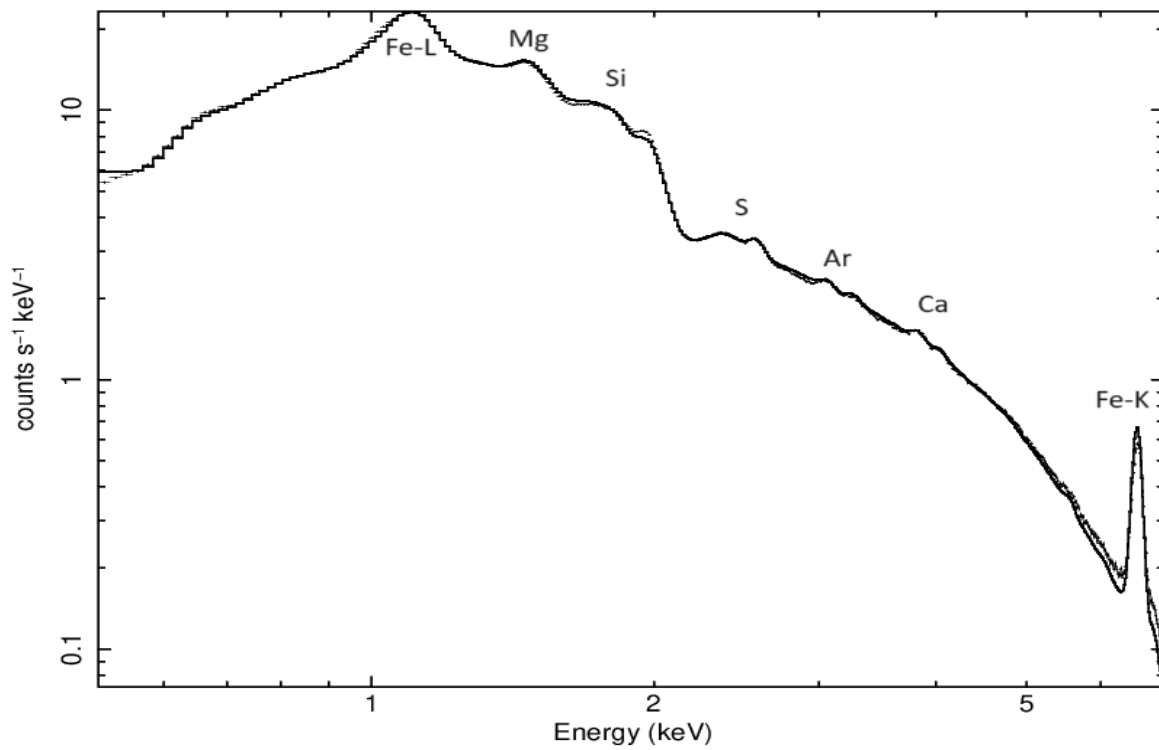


Figure 2.15: Locations of metal complexes in a broadband spectrum of the Perseus cluster. These denote the locations of the narrowbands used in Chapter 4.

Cluster Data					
Cluster	Exposure Time (ks)	Temp. (kT)	Metallicity (Solar)	Total Flux (erg cm <sup>-2</sup> s <sup>-1</sup> )	Fe-K Flux (erg cm <sup>-2</sup> s <sup>-1</sup> )
A426	768	3.64	0.558	$2.68 \times 10^{-10}$	$8.78 \times 10^{-12}$
A478	42	5.85	0.369	$7.46 \times 10^{-11}$	$2.02 \times 10^{-12}$
A754	138	7.31	0.338	$1.21 \times 10^{-11}$	$2.78 \times 10^{-13}$
A2029	77	7.19	0.539	$6.80 \times 10^{-11}$	$2.37 \times 10^{-12}$
A2142	155	7.94	0.318	$4.51 \times 10^{-11}$	$9.27 \times 10^{-13}$
A2199	158	3.74	0.532	$4.17 \times 10^{-11}$	$1.4 \times 10^{-12}$
A2319	90	8.46	0.367	$3.12 \times 10^{-11}$	$3.15 \times 10^{-13}$
A3571	34	8.11	0.53	$3.37 \times 10^{-11}$	$9.15 \times 10^{-13}$
A3667	494	6.59	0.352	$1.08 \times 10^{-11}$	$2.72 \times 10^{-13}$
AWM7	182	3.32	0.831	$1.98 \times 10^{-11}$	$8.61 \times 10^{-13}$
Centaurus	660	1.78	0.613	$3.89 \times 10^{-11}$	$4.66 \times 10^{-13}$
Coma	28	8.67	0.268	$1.28 \times 10^{-11}$	$1.42 \times 10^{-13}$
Cygnus A	99	7.42	0.882	$6.11 \times 10^{-11}$	$3.14 \times 10^{-12}$
Hydra A	215	3.59	0.419	$3.42 \times 10^{-11}$	$8.68 \times 10^{-13}$
MS0735	434	5.20	0.376	$6.05 \times 10^{-12}$	$1.49 \times 10^{-13}$
Ophiuchus	279	7.73	0.478	$9.39 \times 10^{-11}$	$2.86 \times 10^{-12}$

Table 2.3: Data extracted from models using the XRISM sized regions of each cluster. Every datapoint is placed in tables of the cluster datasheets found in the appendix of this thesis. The exposure time is in units of kiloseconds (ks) which represents  $10^3$  seconds.

## 2.6 Conclusion

16 commonly known clusters were obtained from CHANDRA's X-ray database. By extracting spectra in concentric annuli and using Xspec modelling radial temperature and abundance profiles were produced for each cluster.

By observing both abundance and temperature profiles, trends were discovered for both cool-core and non-cool-core clusters. Most of the non-cool-core clusters had a flat metallicity profile around  $0.3 Z_{\odot}$ , with flat temperature profiles. Cool-core clusters appear to have the metallicity peak at a radius between  $0.008 - 0.05 r_{2500}$ . The metallicity at this peak varies between clusters, with values ranging from  $0.5 - 2 Z_{\odot}$ . Cool-core clusters have a steady decrease in metallicity starting at radii larger than  $0.05 r_{2500}$ , asymptotically approaching  $0.3 Z_{\odot}$  at large radii. This implies that there must be an early enrichment scenario, as the clusters found at different redshifts ( $z = 0.01 - 0.54$ ) all approach  $0.3 Z_{\odot}$  at large radii. The edge of the cluster contains ICM gas that has not undergone cooling. The gas found at large radii should indicate the evolution of the cluster, but the observed values are higher than the metal production rate of standard supernovae. At radii below  $0.008 r_{2500}$ , several cool-core clusters appear to decrease in metallicity, some going below the observed outer limit of  $0.3 Z_{\odot}$ . This implies that there is a metal ion-removing component, such as dust, that combines with the cooled ions. This combination of dust and metal ions removes their ability to produce X-ray emission lines, causing the metals to appear as if they have been removed from the cluster. Other possibilities for this sudden extinction of metallicity may be related to the large cavities in these inner regions. These cavities may be displacing the metal-rich gas, pushing it into distant radii in the cluster.

There are a few unique clusters that do not follow the observed trends in the dataset. The two clusters that do not fit the standard cluster classification are Abell 3571 and Abell 2142. Abell 2142 is a cool-core cluster since the radial temperature of the cluster decreases towards the core. Unlike the other cool-core clusters, Abell 2142 appears to have a flat metallicity profile, a characteristic of non-cool-core clusters. The metallicity of Abell 3571 increases towards the center of the cluster, while the cluster's temperature profile appears to be almost flat. This suggests that Abell 3571 is an unusual non-cool-core cluster, as it has a metallicity signature of active cooling flows, but the temperature profile does not indicate cooling.

# Chapter 3

## Simulating XRISM Data

*This chapter includes original research, using data from the publicly available CHANDRA X-ray Observatory database, Hitomi data found publicly on NASA’s HEASARC website and XRISM tools available on HEASARC as well. All X-ray data within this chapter was analyzed and produced by Neo Dizdar unless stated otherwise.*

The turbulent motions of the gas in the ICM are expected to be proportional to the power of the AGN, but measuring the precise velocity dispersion proves to be difficult using low-energy resolution X-ray data. This leads X-ray astrophysics to turn to XRISM, a new X-ray mission that captures spectra at a resolution of 5eV. Prior to the launch of this mission, galaxy cluster data is simulated and modelled to select viable candidates to propose for observation time. This process uses the datasheets produced in Chapter 2 as initial values, then clusters are converted into simulations with XRISM’s high energy resolution. Candidate clusters are selected by observing the total photon counts and possible unique structures, as the observation time for the telescope is limited. Hydra A, MS0735 and Abell 2199 are clusters that emit enough Fe-K photons within the limited observation time to accurately model their simulated turbulent velocity speeds. As these three clusters are shown to produce enough photons to study their velocity structure, they were submitted for XRISM’s A01 Observation Cycle.

### 3.1 XRISM

XRISM is a soft X-ray mission done in collaboration with JAXA and NASA. It successfully launched on September 7th 2023, with the first-light images taken late-October 2023. The payload contains two scientific instruments: Xtend and Resolve.

Xtend is an imager that has a  $38 \times 38$  arcmin field of view, used for imaging X-ray data. Resolve is an X-ray spectrometer, having a smaller field of view at 2.9 arcmin but a high spectral resolution at 5eV at a bandpass of 0.3 - 12 keV [76]. Compared to CHANDRA’s ACIS instrument (95 eV resolution), XRISM’s spectrometer can resolve separate emission lines within a line complex in a smaller footprint in a larger bandpass. Resolve’s detector is a  $6 \times 6$  pixel microcalorimeter array, one pixel is turned off as a calibration pixel. X-ray microcalorimeters are thermal X-ray counting devices split into 3 components, an absorber, thermometer, and heat sink, this absorbs an X-ray and accurately measures the temperature of the incident photon to a precision of up to 5eV [39]. This spectral resolution is important to glean information about velocity changes within the ICM, as the widening of thin spectral lines due to Doppler broadening may be measured precisely. This increases the accuracy in models observing the motions of gas in clusters. The image resolution in microcalorimeters is limited to the number of physical “pixels” they are made of. Each pixel in Resolve covers  $\sim 30$  square arcseconds in the sky, implying that features smaller than 30 square arcseconds cannot be resolved. Using Xtend and Resolve in tandem can provide large high-resolution X-ray images with smaller important regions being provided with a high energy resolution spectrum.

Xtend and Resolve are built to be similar to the soft X-ray spectrometer (SXS) and soft X-ray imager (SXI) found on Hitomi. Hitomi is a previous mission that lost contact in 2016. During Hitomi’s short mission length it was able to obtain an image of the Perseus Cluster [78]. This image of Perseus is used as a template for simulations of XRISM, a method that allows simulated data to be generated before the launch of the mission. These simulations are generated through XSELECT, a tool used to generate spectra provided by NASA’s HEASARC. The spectrum of Perseus is used to test if precise metallicities and velocities may be obtained from high energy resolution instruments. Models will have to rely on the Fe-K complex as it has the highest signal-to-noise ratio of all visible lines in the SXS spectrum (see Fig 3.1). This chapter will focus on using Resolve (SXS) simulated spectra, Xtend (SXI) can produce a spectrum over a larger footprint but it’s energy resolution is poor ( $\sim 180$  eV) [74].

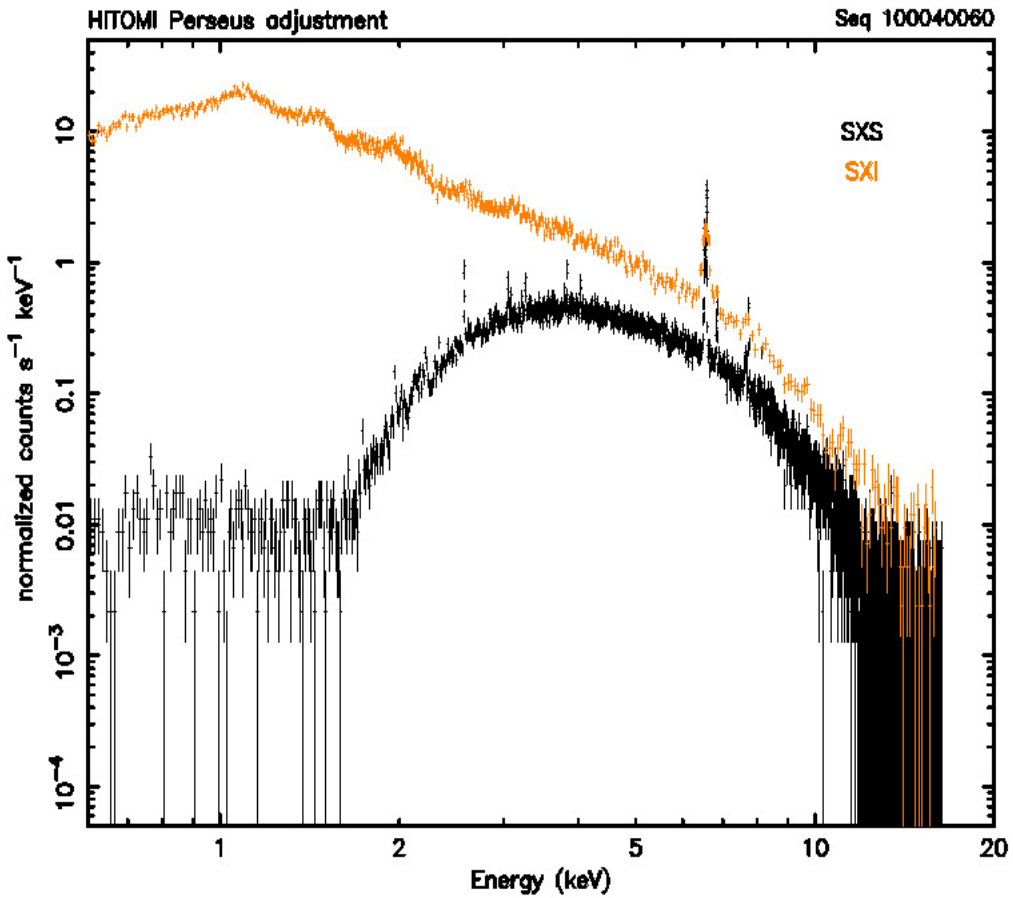


Figure 3.1: A spectrum of the Perseus cluster captured by Hitomi. The spectrum in black is captured by the SXS instrument whilst the orange is captured by the SXI instrument. The SXI spectrum has an overall lower spectral resolution, while the SXS image has an attenuated spectrum due to gate valve issues.

### 3.1.1 Gate Valve

A critical component, the gate valve, failed to open after XRISM reached its expected orbit. Gate valves protect the instruments behind the valve from outgassing within the telescope during the initial operation of the telescope. These valves may be considered as aperture doors within the telescope. Outgassing occurs when gas trapped within components is released through evaporation or sublimation within the telescope [44]. The valve contains a  $260\text{ }\mu\text{m}$  thick beryllium window, this material will absorb weak photons stopping their approach to the detector. Photons with energies below 1.7 keV will not reach the Resolve instrument as long as the gate valve is closed, but there will be noise in this attenuated region produced by the instrument. This filtering effect persists throughout the entirety of the spectrum, lowering the total photon counts beyond 1.7 keV. At high-energy key regions such as 6-7 keV (Fe-K complex), the attenuation of photons is minimal and should not affect abundance or velocity measurements within the visible metals (as seen in Fig 3.2). In Fig. 3.1 there are X-ray emission lines attenuated below this 1.7 keV limit, some of which are N (0.5 keV), O (0.65 keV), Ne (1.0 keV), Fe-L complex (1.1 keV) and Mg (1.5 keV) [32]. As Si lines appear between 1.8 keV (Si XIII) and 2.4 keV (Si XIV), it is a metal that is significantly affected by the attenuation of photons through the gate valve. Major Si lines (like Si XIV) will appear above the noise but the total photon counts will be diminished. Observing through a gate valve loses key information on cooler gases which may have different bulk motions in comparison to the warmer gases (at higher keV). Trends shown in Si and S lines may be missing correlated values with cooler metals by only observing a spectrum with data over 1.7 keV.

The effect of a gate valve on an X-ray spectrum is important to observe, since the Hitomi mission was lost before the gate valve could be opened. Therefore, the only data provided by Hitomi was data attenuated by a gate valve over the SXS instrument. The SXI instrument did not have a gate valve issue, and thus contains the full X-ray spectrum at a low spectral resolution. The gate valve has proven to be an issue for the XRISM mission as well, as the method of moving the gate valve has failed, with multiple attempts to open the valve door taken post mission launch. This means that Cycle 1 Resolve data will be provided with an attenuated spectrum, changing the expected energy range from 0.2 keV – 12 keV to 1.7 keV - 12 keV.

In this chapter, most simulations are generated to simulate the effects of a closed gate valve in order to accurately match early XRISM results. Initially, simulations were made emulating an open gate valve prior to the announcement of mechanical gate valve errors on the XRISM payload. All spectra simulated with the gate valve open were preserved to compare the effect of the gate valve on the shape of the overall spectrum. Simulations with the gate valve open will not be used for any further science. Observing the photon counts

within the X-ray emission lines in simulations with the gate valve closed provides an overall minimum expected luminosity. By selecting clusters using simulations with the gate valve closed as a threshold for exposure time, it is expected that most spectra will produce higher photon counts when the gate valve is opened. XRISM will prioritize brighter clusters while the gate valve remains closed. In the future, when the gate valve is successfully opened, clusters with lower luminosities can be observed with the Resolve instrument. While the gate valve attenuates low-energy X-ray data, hot gas science can still be performed on well-known clusters by observing high-energy X-ray data.

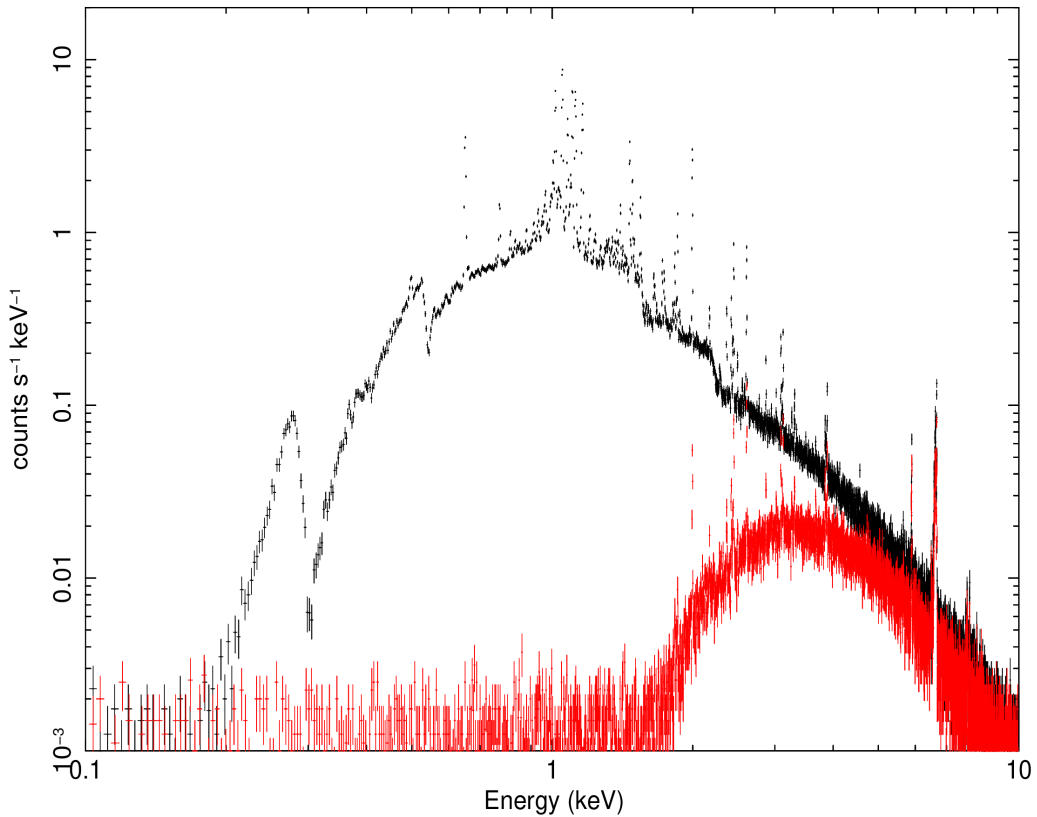


Figure 3.2: Simulation of M87 through XRISM’s Resolve instrument, with a 1 Ms exposure time. Red points represent a closed gate valve, black points represent an opened gate valve

## 3.2 Simulating Spectra

Since each cluster contains unique ratios of metals and velocity dispersion, the simulations of galaxy clusters require CHANDRA data. The data found in Chapter 2’s datasheets was extracted and converted to the spectral (and spatial) resolution of Resolve. The models were generated through Xspec, using key datapoints found on the datasheets such as temperature, abundance, redshift, photon normalization, and hydrogen column density. These components create a `phabs*bapec` model. As the simulations are made to test the sensitivity of velocity broadening on high-resolution X-ray emission lines a velocity broadening component was artificially added to the model. This is repeated several times per cluster; each iteration changes the velocity broadening parameter to test the effect of a range of turbulent velocities per cluster. The main turbulent velocities that were selected were  $100 \text{ km s}^{-1}$ ,  $200 \text{ km s}^{-1}$  and  $300 \text{ km s}^{-1}$ . Certain clusters with known higher velocity broadening effects were simulated with higher values such as  $600 \text{ km s}^{-1}$ ,  $1000 \text{ km s}^{-1}$  and even  $2000 \text{ km s}^{-1}$  turbulent speeds.

The spectrum is generated using the CHANDRA image and predicted model as a guide. Spectrum generation requires an image of a  $2.9 \times 2.9$  arcmin field of view over the selected cluster pointing. This field of view is represented as the green square in the datasheets. The simulation tools require an additional parameter, the exposure time in terms of kiloseconds (ks), before simulating spectra. The exposure time and velocity broadening values are the only variables that are adjusted between each simulation per cluster. XSELECT then requires the mission (XRISM) and instrument (Resolve) to be selected, prior to the launch of XRISM the mission variables were based off of Hitomi’s SXS instrument. The simulation software convolves the spectral model provided by Xspec, the characteristics of the selected instruments provided by XSELECT and the CHANDRA spectrum, generating a high energy resolution spectrum. The simulated spectrum requires an ARF and RMF to be converted into energy units. Hitomi’s ARF and RMF files may be found on the HEASARC website, the ARFs have gate valve open or closed options, while the RMFs have a range of energy resolutions (5-8eV) available. As the data from XRISM is captured at a resolution of 5eV and it’s gate valve remains closed the RMFs and ARFs that reflect this were selected.

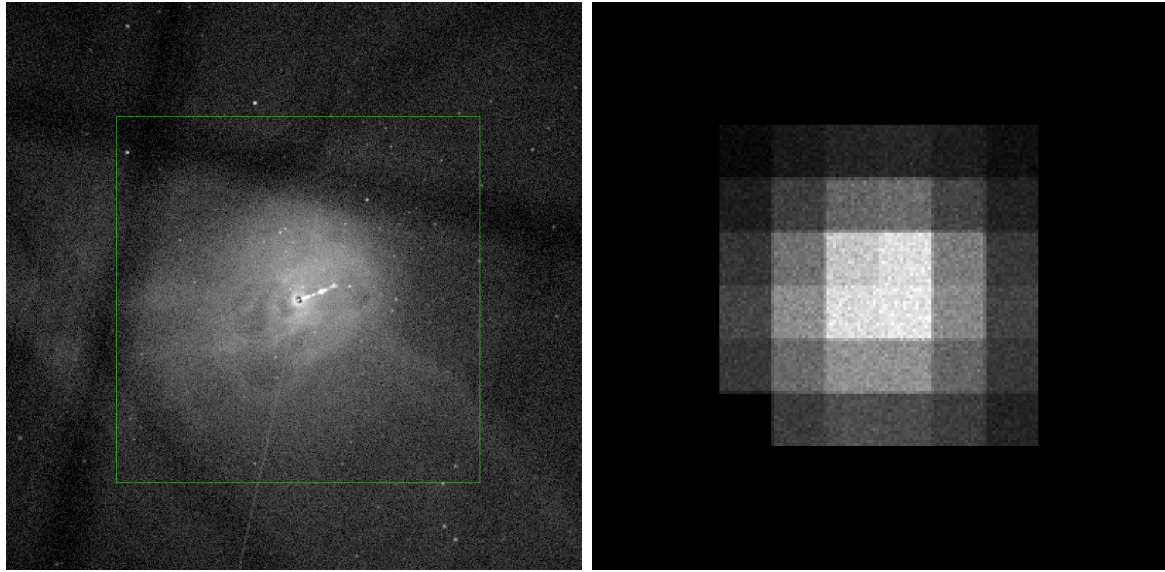


Figure 3.3: The image on the left is a summed CHANDRA image of M87 with the green square highlighting Resolve’s footprint. The image on the right is the simulated Resolve image of M87. There are  $6 \times 6$  pixels shown with the calibration pixel (pixel 9) removed in the bottom left of the simulation.

As seen in Fig. 3.3 the image resolution of XRISM’s Resolve instrument is poor. Due to this XRISM data cannot be extracted in tight concentric annuli as was done in Chapter 2 (see Fig 2.3). The simulated image can be partitioned into 3 square annuli but it will lose the capability of observing smaller structures. Radial profiles can be made by taking multiple exposures with the telescope pointing being moved radially outwards from the core. As the annuli would be larger and pseudo-circular it will introduce large radial errors on the radial profile. Proposing multiple exposures, particularly into the dimmer non-core regions of the cluster will use a large amount of instrument time. This may lead to proposals being denied early into the launch cycle of a new telescope. Therefore, it is expected that detailed radial profiles will not be produced with early XRISM data. Only clusters with significant features outside of the core will have simulations with multiple pointings. Since these pointings will be offset from the core they will require a significantly longer exposure time. Off-center pointings are heavily dependent on the luminosity of the cluster’s core. If the central pointing is too dim then it is unlikely that off-center pointings will have enough photon counts to be observed within the allotted observation time limit.

### 3.3 Selecting Clusters

The selection of clusters is controlled by the limitations of the instruments available on the XRISM mission. Early Cycle 1 proposals had their observation time limited to 200ks. This limit was in place before the gate valve opening failure was known, therefore clusters must have clear X-ray emission lines between 1.7 keV - 12 keV within 200ks to be selected. Each simulation was produced with an exposure time of 200ks as the upper limit. Photon counts are linearly scaled by changes to exposure time, thus an image with 100ks exposure time should on average be half the counts of a 200ks simulated exposure.

There is a list of known clusters that have already been selected as early release data, some of the clusters that appear on this list are: Abell 426 (Perseus), Abell 2029, Centaurus, Coma and M87. Clusters that are already on this list do not need to be simulated as their proposals have already been accepted. Any other cluster found in the datasheets can be simulated and tested to see if it is suitable for an observation proposal. Cluster candidates must have enough Fe-K photons to extract the injected turbulent velocity broadening value accurately with a `phabs*bapec` model. After testing, 150 non-bremsstrahlung photons in the He- $\alpha$  Fe-K resonance line is the lower limit to accurately model the Fe-K line. Below 150 photons the signal-to-noise ratio decreases and errors increase in modelling the turbulent velocity broadening parameter. If the cluster contains unique features found in off-center pointings they will be tested as separate exposures. The Fe-K complex is selected due to its high signal-to-noise ratio and being located at the least affected region by the gate valve. The 6 keV – 7 keV range is weakly attenuated by the gate valve as seen in Fig 3.2. This creates flexibility in producing proposals as the Fe-K counts will not change significantly if the gate valve is opened in-between proposal submission and the time of observation. The Fe-K complex was also selected for the Fe-K He- $\alpha$  w-line, a thin resonance line. This line has a higher emissivity compared to the other lines in the complex, which improves the accuracy of modelling the velocity broadening parameter since other lines do not strongly influence the w-line's width. The method of removing continuum photons under the Fe-K complex is similar to the process discussed in Section 2.3.2. The photon counts of smallest bins on either side of the Fe-K complex (bin size  $\sim 0.5\text{eV}$ ) were extracted and saved separately. Using these photon counts per bin the slope between the two bins was interpolated, creating a total background continuum photon count. This background continuum count was removed from the total Fe-K region, with the residuals representing the photons emitted in from the Fe-K complex.

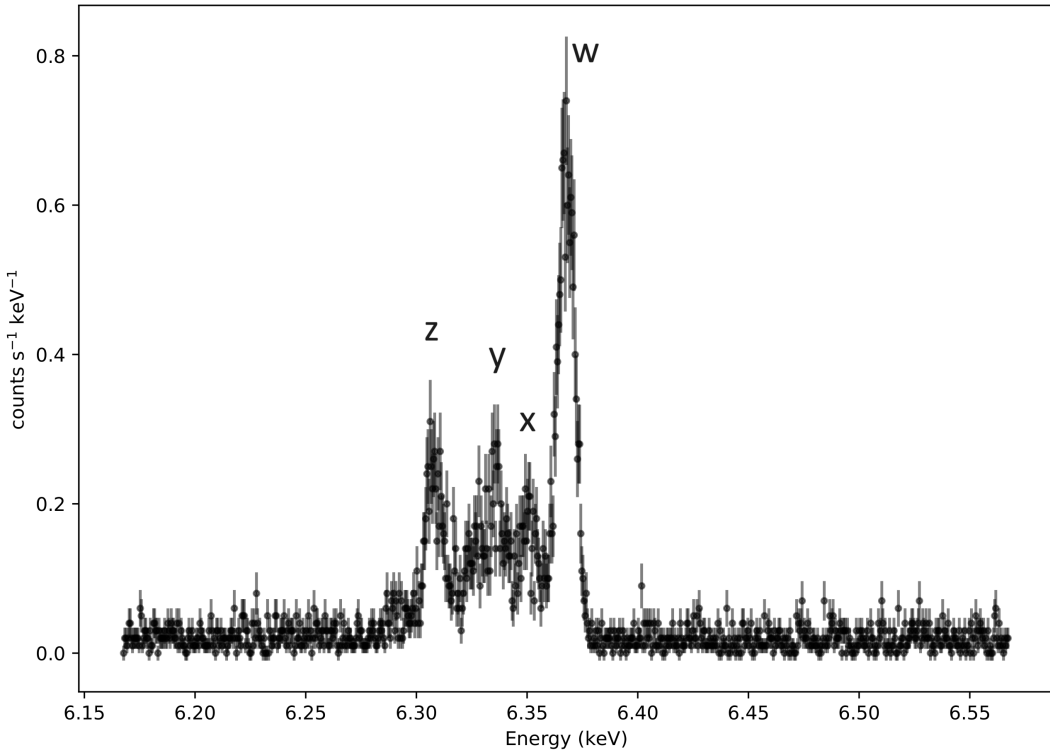


Figure 3.4: A simulated Fe-K narrowband of Hydra A. The major lines are labelled here from w to z, w represents the bright He-alpha like resonance line Fe XXV  $7 \rightarrow 1$ . The other major peaks labelled are also transitions in Fe XXV,  $6 \rightarrow 1$ ,  $5 \rightarrow 1$  and  $2 \rightarrow 1$  respectively. There are other weaker lines found within this complex, such as high energy level H-like (Fe XXIV) lines that may broaden the brighter He-like lines. [5, 32]

Each selected cluster was simulated with multiple different turbulent velocity values, a range between  $100 \text{ km s}^{-1}$  –  $2000 \text{ km s}^{-1}$  (dependent on the cluster). Each simulation requires a w-line photon count calculation due to the line broadening. Broadening emission lines lowers the amount of counts per energy bin but increases the bins the emission line encompasses. This broadening lowers the signal-to-noise ratio of the Fe-K complex and can cause photons from the emission line to appear as background x-ray continuum photons. As it can be difficult to accurately disentangle photons from broadened emission lines and the background continuum photons, the Fe-K complex and He- $\alpha$  w-line photon count will fluctuate.

If a dim cluster is found to fit the minimum photon count requirement it's "Iron Flux" value (in datasheet found in Appendix) is used as lower bound for selecting future clusters. It was found that MS0735 is a suitable dim candidate for a central pointing simulation emitting 250 – 300 Fe-K w-line photons. All clusters that emit more Fe-K photons than MS0735 can also be used for simulation testing. A2199 and Hydra A were selected as two clusters that were well beyond the minimum Fe-K flux. Each of the selected clusters are tested for the ability to extract particular velocity broadening values, with each testing a range of simulated turbulent velocities. Hydra A will be tested with two pointings, as it's dim outer cavities provides enough Fe-K photons. If Hydra A's offset pointing can produce more than 150 photon counts then it will be determined as usable pointing for the proposal.

Cygnus A is a cluster that fits the criteria for a XRISM A01 observation candidate, but another research team is producing their own proposal for the cluster. Instead, Cygnus A was simulated and used as a cluster to test the accuracy of modelling velocity broadening. Cygnus A is a bright and powerful cluster, having the highest Fe-K flux of candidate clusters available, as shown on Table 2.3. The Fe-K complex of Cygnus A is more defined than dimmer clusters and can be used as an expected baseline for a Fe-K rich cluster. Cygnus A simulations may be tested to show the effects of changing the exposure time while generating its spectrum. As will be seen in Table 3.1 Cygnus A exceeds the proposal luminosity threshold by 16x the minimum photon counts with 200 ks exposure time. This implies that Cygnus A is a great candidate cluster for early XRISM observations as it will require less than 20 ks to obtain enough information to accurately extract the turbulent broadening component of its hot atmosphere.

Simulated Cluster Data				
Cluster	Simulated Vturb (km/s)	Temperature (kT)	Net Fe-K w-line Counts	Fe-K Background Counts
Hydra A	100	3.64	1281	23
	200	3.64	1223	42
	300	3.64	1194	70
	600	3.64	1065	93
Hydra A (north)	100	3.93	131	23
	200	3.93	152	39
	300	3.93	154	40
	600	3.93	184	70
MS0735	100	5.14	251	38
	200	5.14	289	24
	300	5.14	283	45
	600	5.14	332	60
CygnusA	100	6.84	4041	450
	200	6.84	4273	448
	300	6.84	4852	500
A2199	100	3.52	1375	209
	200	3.52	1369	271
	300	3.52	1637	297

Table 3.1: Each cluster was simulated with 200ks exposure time. Fluctuations in the Fe-K w-line counts occur due to the line's edges convolving with the rest of the complex. Photon counts in simulations with lower turbulent velocity have a higher confidence value.

### 3.3.1 Hydra A

Hydra A contains one of the strongest Fanaroff-Riley 1 (FR-1) radio sources found in a galaxy cluster [29]. The classification FR-1 defines that the radio luminosity is brightest to the center of the emitting source with the jet lobes appearing as the dimmest portion of the structure. Hydra A's jet power is  $\sim 10^{61}$  ergs or  $\sim 2 \times 10^{45}$  erg s $^{-1}$  [70, 82, 110]. These calculations were done by observing the shockfronts of the cavities produced by the AGN.

The physical structure of this cluster is complex, another reason to observe Hydra A, there are 3 pairs of cavities being produced by the strong AGN. These cavities show an oscillation of the AGN, appearing as a chain of 3 cavities at different cluster radii and sizes. Due to the orientation in the sky and the brightness of the cluster this allows for the characteristics of the cavities to be easily quantifiable (energy, speed and volume). Through the size of the cavities, especially the outer pair found 200 kpc – 300 kpc from the BCG, may be large enough to be spatially resolved by Resolve. Further discoveries may be achieved by comparing the motion and metallicity within the cavity to the turbulence of the surrounding hot gas atmosphere. This creates a clearer comparison between jet kinetic energy and the surrounding atmospheric kinetic energy. By observing the 3 pairs of cavities separately we can measure both the bulk motion and turbulent velocity of hot and cool gas in large structures within Hydra A. While the cluster is good candidate for XRISM observations it will need at least two different exposures taken at different regions to fully encompass the outer cavities. A central pointing of the cluster can capture the central two pairs of cavities, and a northern pointing can fit one of the larger cavities fully within Resolve's footprint. Due to the radial decrease in surface brightness the central pointing would be expected to contain more Fe-K w-line counts than the northern pointing. As expected, the simulations of Hydra A's center pointing on average have 1200 counts in the Fe-K w-line, while the north pointing barely fits the requirement, having  $\sim 150$  counts in the Fe-K w-line. This suggests that the central pointing can have its exposure decreased from 200 ks to 100 ks while being above the 150 photon count threshold, while the north pointing must have a minimum of 200 ks exposure time.

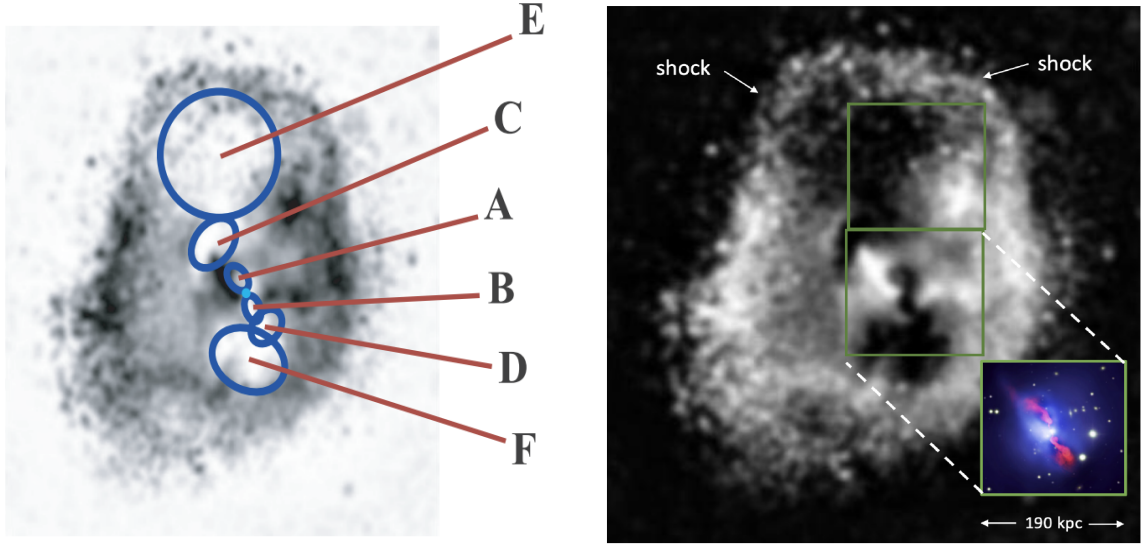


Figure 3.5: An example of Hydra A’s cavity locations and the two proposed exposures of the galaxy cluster. This shows that the center pointing covers the pair of cavities labelled A, B and D fully, with C and F having a majority of their structure within the FoV. The second north pointing observes the surrounding shock of the largest cavity E. - [110].

The churned motion within the centers of galaxy clusters is found to have an average turbulent velocity broadening of  $\sim 150 \text{ km s}^{-1}$ . Most clusters centers are found to be in a range between  $100 - 300 \text{ km s}^{-1}$  [36]. This implies that Hydra A’s central pointing should be simulated with a turbulent broadening component ranging from  $100 \text{ km s}^{-1}$  to  $300 \text{ km s}^{-1}$ . Three simulations are made to cover this range,  $100 \text{ km s}^{-1}$ ,  $200 \text{ km s}^{-1}$  and  $300 \text{ km s}^{-1}$ . A  $600 \text{ km s}^{-1}$  simulation is included in the case that this Hydra A has a higher velocity broadening than expected. The northern pointing of the cluster contains a  $210 \text{ kpc}$  wide cavity, the radius and expansion speed of the cavity should correlate to the motion of the surrounding shock front through work being done on the surrounding environment. This predicts that the motion of the surrounding gas should be between  $300 - 600 \text{ km s}^{-1}$  [110]. With this range two simulations may be made, using the minimum and maximum values to observe the accuracy in which our models may observe turbulent velocity broadening on a spectrum.

### 3.3.2 MS0735

MS0735 was selected due to the strength of the jets within the cluster, as contains a strong FR-1 radio source. The large inner cavities of the cluster have been measured to have  $\sim 10^{61}$  ergs injected by its jets [90]. MS0735 was selected to be a candidate cluster due to these cavities, as they are large enough to be spatially resolved by Resolve, and have documented jet energies. This will simplify measuring the relationship between atmospheric kinetic energy and jet energy. XRISM can also observe the bulk velocities of hotter and cooler gas in the cluster.

The angular size of MS0735's cooled core fits into the 2.9 x 2.9 arcminute footprint of Resolve. As it has the lowest Fe-K flux of the three clusters only a central pointing can be simulated. This central pointing will contain the pair of 200 kpc wide cavities and will be able to observe the strong shock front at the edges of the cool core. The cavity radius is expected to be proportional to this shock front, expanding the cavities at a rate of  $\sim 500$  km s $^{-1}$ . The surrounding atmosphere should show a similar turbulent broadening velocity. The expected maximum velocity is  $\sim 600$  km s $^{-1}$  while the central regions are expected to have a velocity of  $\sim 300$  km s $^{-1}$ . The simulations must test the accuracy of obtaining the correct turbulent velocity between these two values. These values are similar to Hydra A's northern pointing, which is a point that also observes a cavity of a similar radius. Two simulations were made observing the maximum (600 km s $^{-1}$ ) and minimum (300 km s $^{-1}$ ) expected turbulent broadening values. Simulations of MS0735's central exposure were selected to have 200 ks of exposure time, as both simulations obtain  $\sim 300$  Fe-K XXV w-line photon counts. While the exposure time can be lowered to 100 ks, a longer exposure time is preferable since it lowers the noise surrounding the Fe-K line, providing a clearer measurement of velocity dispersion.

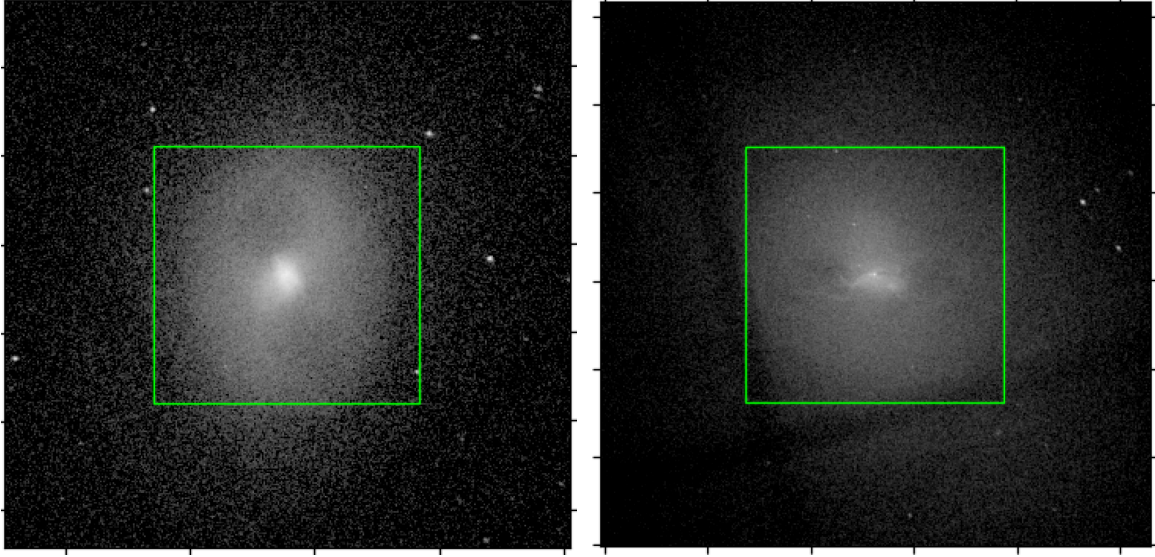


Figure 3.6: Unsmoothed CHANDRA images representing the suggested pointings of XRISM for both MS0735 and A2199. Both have central single pointings with a pair of large cavities located within each pointing. MS0735 is pictured on the left, A2199 is pictured on the right.

### 3.3.3 A2199

A2199 is a cluster with jets emitting  $3.98 \times 10^{43}$  erg s $^{-1}$  [80]. It is one of the brightest clusters in X-ray emissions, proving to be a good candidate cluster to observe with XRISM. In comparison MS0735's jets are  $\times 10^3$  stronger than A2199's [90, 83]. Observing a weaker jet is important as MS0735 and Hydra A are outliers, having extremely strong jets, meanwhile observing A2199 may provide data akin to a common galaxy cluster. A2199 was selected to have 1 pointing centered at the core of the cluster, as surrounding structures are too dim to obtain useful data. Within this center pointing the large pair of cavities are both fully encapsulated, the expected turbulence should be similar to the centers most common clusters, the range being from 100 - 300 km s $^{-1}$  [36]. Simulations were made using the minimum and maximum value within this range, and on average  $\sim 1400$  counts within the Fe-K w-line were observed with 200 ks of exposure. The exposure time can be lowered to 50 ks and still observe over 300 photon counts in the Fe-K w-line. This lowered exposure time can obtain the proper turbulent velocity broadening component within the spectral line.

## 3.4 Modelling Broadening

The goal of this chapter is to observe the kinetic energy being injected into the surrounding ICM by radio jets; suggesting that simulations must be produced with injected turbulent velocity broadening. This injected velocity is considered the true value of the spectrum, models are tested to see how accurate they are in extracting this value. This process can be done over the broadband spectrum but may cause larger errors especially on low emissivity spectral lines. To mitigate this source of error modelling was only done on the narrowband Fe-K complex located between 6 – 7 keV. Redshift will shift the Fe-K complex from 6.7 keV. As seen in Fig. 3.4 the Fe-K complex is comprised of multiple He-like Fe (Fe XXV) lines: the w-line, a resonance line, the z-line, a forbidden line and the x and y lines, two intercombination lines [5]. Photons from other lines under this complex do affect the lines above, but their emissivity is substantially weaker than the w-line. This may cause the other three major lines to appear broadened, which can overestimate the effect of turbulent broadening. This leads to the w-line driving the model’s calculation of turbulent broadening.

Observations over the 6 – 7 keV band may include photons from the H-like Fe lines (Fe XXVI), as there is a doublet located near 6.9 keV. This doublet is cropped out of the narrowband to further remove inaccuracies to the modelling software. This cropping process is done initially on the simulation with the highest injected turbulence as this would broaden the H-like Fe the most, this limit was then kept for each simulation of the same exposure to not alter models.

This leads to a system where only the w-line in the Fe-K complex is modelled with the nearby doublet removed. To model the effect of turbulent broadening the width of the spectral line must be broken-down into components. Three Gaussian broadening components are used: thermal Doppler broadening, instrumental broadening and turbulent broadening. To calculate the turbulent broadening component the other two components must be calculated, this is easily done as thermal broadening requires the temperature off the gas and the mass of the ion whilst the instrument broadening is equivalent to the spectral resolution limits of the instrument used. The full linewidths of each component may be calculated and subtracted from the full linewidth of the Fe-K w-line. Since this is equivalent to three stacked Gaussians the turbulent broadening component should equate to the residual linewidth, which is then converted into a velocity value. The equations for obtaining each component is shown below:

$$\sigma_{\text{therm}} = \sqrt{\frac{kT}{m_{\text{ion}}}} \quad (3.1)$$

$$\sigma_{\text{inst}} = \frac{5eV}{2\sqrt{2 \ln 2}} \quad (3.2)$$

$$\sigma_{\text{turb}} = \sqrt{\sigma_{\text{total}}^2 - \sigma_{\text{therm}}^2 - \sigma_{\text{inst}}^2} \quad (3.3)$$

$kT$  is the temperature of the cluster, this value is found in the datasheets of the cluster and  $m_{\text{ion}}$  is the mass of an electron. In the instrumental standard deviation the estimated FWHM of XRISM is considered to be 5eV and thus is used for the instrumental broadening calculation. This calculation was done on the Fe-K w-line. With the w-line centered, the turbulent velocity broadening is calculated by subtracting the other modelled components off of the w-line linewidth. This modelling process was approached in two different methods, the first being only modelling the Fe-K w-line while ignoring the rest of the complex, the other was applying similar models onto each spectral line within the complex and extracting the average velocity width of those. There are four main Fe XXV lines in the complex, six total high emissivity lines spanning from Fe XXIII to Fe XXV and over 110 total spectral lines, many with low emissivities that can affect the shape of the Fe-K complex [32]. This causes issues as a model with too many components may fail and provide unrealistic velocities in the other emission lines. Therefore only the He-like w-line was fitted and observed to define the turbulent broadening of a cluster.

A fourth component, the natural line width, is a broadening feature caused by the uncertainty principle, in which the transition between photon states is not perfectly at one energy and may shift up or down by a small offset. It is expected to be the weakest component within the model it should have little impact on the turbulent broadening calculation. Future work may require natural line widths testing if their impact on broadening calculations is significant, especially as instrumental spectral resolution reaches  $\sim 1$  eV.

The data is modelled using Python's `lmfit` library, a tool that utilizes least squares minimization for curve fitting. The Gaussian model of `lmfit` was used and the width is scaled with Eq 3.3. The `lmfit` is provided with line energy as the center of the Gaussian, this allows multiple Gaussians to be fit at once, as seen in Fig 3.7.

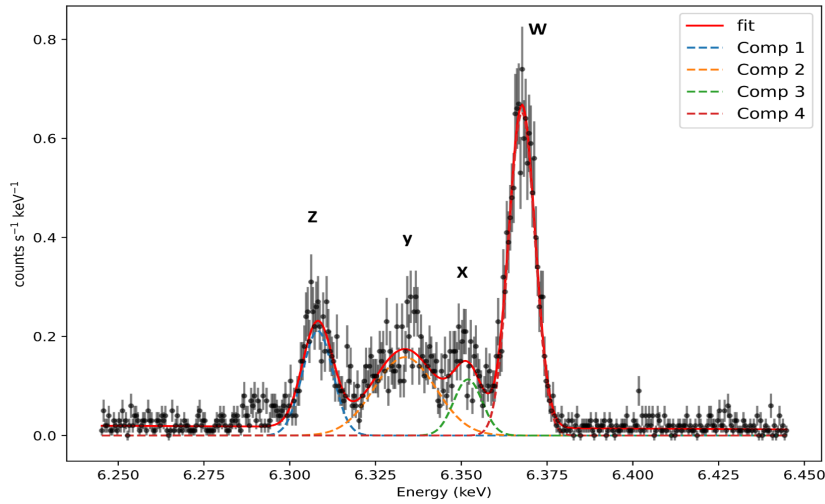


Figure 3.7: A model of Hydra A with 200 ks exposure time and  $100 \text{ km s}^{-1}$  turbulent velocity. The model contains the Fe-K complex with 4 components that relate to the 4 main He-like Fe spectral lines. This and another model with 6 lines were attempted. This model provides broadening velocities on each line, producing unphysical results for the y and x-line.

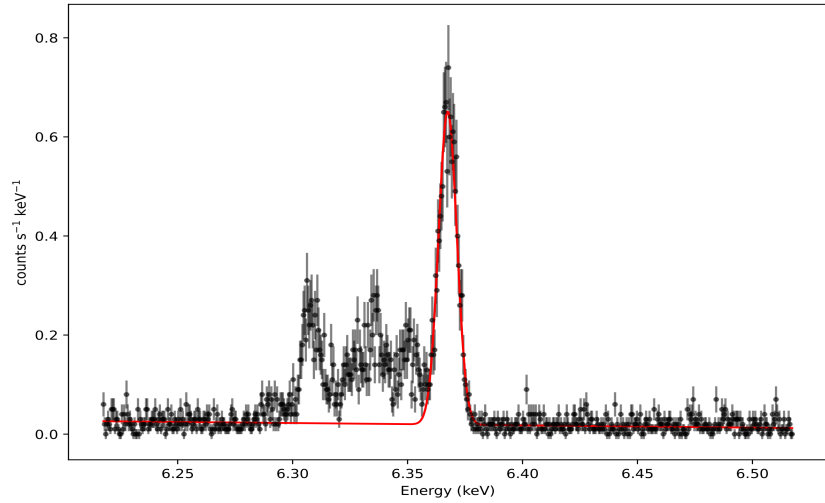


Figure 3.8: A single fit model on the same simulation, the bounds on the x-axis have changed to include more continuum. This will be used as the standard for fitting the w-line for future simulations.

The `lmfit` models were tested against `TBabs*bapec` models. It uses the provided hydrogen column density, redshift and temperature found from the datasheets produced in Chapter 2. This means that the abundance, normalization and velocity broadening are left as free parameters for the model. This was done to examine the differences between the two models, as `TBabs*bapec` uses the entirety of AtomDB on the spectrum, counting all of the different lines within the Fe-K complex. It is expected that models would be more accurate on systems with higher photon counts as this increases the signal-to-noise ratio, allowing the model to properly define a spectral line. SPEX was considered to be used as a method of testing this broadening effect, but early XRISM work appears to be standardizing the usage of Xspec for modelling.

Modelled Velocity Broadening Features						
Cluster	Simulated Vturb (km/s)	Modelled Vturb (km/s)	Modelled Vturb Error	Xspec Vturb (km/s)	Xspec Vturb Error	Fe-K w-line Counts
Hydra A	100	99	7	101	9	640
	300	268	16	280	16	597
	600	609	52	584	33	532
Hydra A (North)	300	337	30	259	29	154
	600	1080	135	482	63	184
MS0735	100	97	19	107	16	283
	300	366	32	303	25	324
A2199	100	104	7	120	6	687
	300	279	13	289	9	742

Table 3.2: A comparison between the injected turbulent velocity and the values that different models obtain from simulated data. The two models used were a scripted model, labelled as ‘Modelled’ in the table, and Xspec’s `TBabs*apec` model. The w-line counts were calculated by observing the photon counts within a narrowband where there was a clear drop in emissivity on both ends.

The data shows that both models appear to be close to the true value in lower velocity systems, with the `lmfit` model being within  $1\sigma$  for most  $100 \text{ km s}^{-1}$  systems. Clusters with lower w-line photon counts cause the models to struggle with obtaining the true velocity broadening value, as can be seen in all of Hydra A's north pointing models. It is expected that the model would struggle to obtain the correct value with a high velocity low photon count spectrum such as the Hydra A North pointing with  $600 \text{ km s}^{-1}$ . This occurs because the Fe-K complex contains multiple spectral lines with similar energies causing the lines to broaden into each other, deforming the shape of the complex, and causing photons from other Fe-K XXIII-XXVI transitions to appear as w-line photons (and vice versa). At greater velocities it is expected that the single Gaussian model will overestimate the velocity broadening component as it begins to include the x and y-line into the single Gaussian, this explains the  $\sim 400 \text{ km s}^{-1}$  overestimation with larger error bars than the Xspec model. The Xspec model should account for multiple lines within the complex and thus should be accurate in obtaining the initial injected turbulent velocity. Yet it appears that Xspec slightly underestimates the velocity broadening of most of the high velocity simulations. This table shows that both models appear to be accurate ( $1\sigma - 2\sigma$ ) at gauging the proper turbulent velocity broadening within a spectrum. As was expected the 150 photon limit in the Fe-K w-line proves as good a requirement to extract a clear value. This also shows that early XRISM with the gate valve closed, the exposure time is increased, will have to be biased towards bright sources.

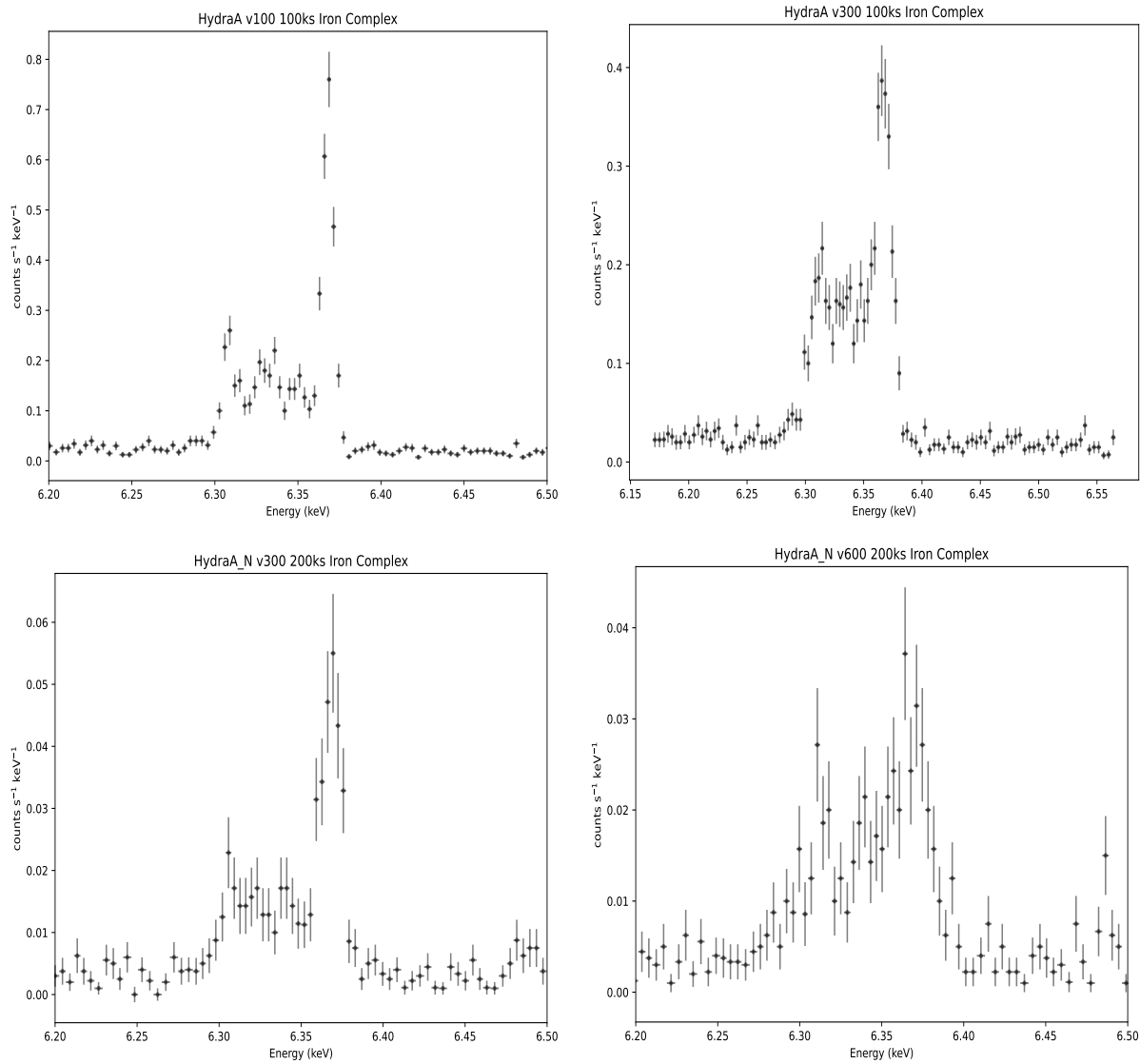


Figure 3.9: Four of five binned Hydra A simulations referenced in 3.4, the upper two figures are central pointing simulations, the lower two are the north pointing. The y-axis represents the counts per second and does change between the figures, thus higher turbulent figures have broader lines and dimmer totals. This showcases the difficulty in obtaining a proper broadening value at higher velocities as the w-line becomes less and less distinct.

## 3.5 Conclusions & Proposal Outcomes

The rate at which AGN radio jet energy converts into the kinetic energy of the surrounding ICM is still considered unsolved. As such XRISM's high spectral resolution instrument (Resolve) will be used to observe the motions of the X-ray emitting gas. To be able to find a relationship between these two components a large dataset of multiple clusters must be made with accurate velocity measurements in the surrounding ICM. To achieve this with a new instrument the cluster selection must go through a proposal process to obtain any instrument time. As expected a proposal with a large dataset of clusters would take too much instrument time, therefore three specific clusters were selected as an initial batch for the first open cycle of proposals.

These three clusters: Hydra A, MS0735 and A2199, were selected due to their high jet power and high X-ray luminosity. The high luminosity allows for a lower exposure time required to obtain enough photons to observe the effects of turbulent velocity broadening on spectral lines. Hydra A emits enough in X-ray photons that an offset northern pointing was added to the proposal. To prove that these are useful clusters to observe they must be simulated and modelled. This process was done by upscaling the spectral resolution of CHANDRA data (from 95eV to 5eV) and producing a simulation of the data with different exposure times and different turbulent broadening speeds. The Fe-K complex of the simulated spectra is then modelled to observe if the models can accurately extract the injected turbulent broadening component. Two different models were used to test if this value can be extracted, the first model being an Xspec **TBabs\*apec** model while the second is an internal **lmfit** model extracting the three major broadening components of a spectral line. The **lmfit** model only observed the bright resonance Fe-K line due to its emissivity in comparison to the other spectral lines in the complex.

The models were tested on at least two simulations per cluster pointing. Each simulation was defined by the expected range of turbulent motion within the ICM, with the simulations representing the maximum and minimum expected turbulent broadening. With Hydra A having two pointings, central and north, separate sets of simulations were done for each. Prior to modelling these clusters it was expected that pointings with an overall lower photon count (Hydra A North and MS0735) and simulations with a higher injected broadening would both cause the accuracy of the models to decrease. This is because the Fe-K resonance line would be less defined in both cases, and as it is the main line in the complex that both models obtain the linewidth from the measured turbulent velocity component decreases in accuracy. Between these two models a trend seems to appear, wherein the **lmfit** model appears more accurate than the Xspec model at low simulated velocities. This is seen in A2199's  $100 \text{ km s}^{-1}$  and Hydra A North's  $300 \text{ km s}^{-1}$  models where the

`lmfit` model extracted  $104 \pm 7 \text{ km s}^{-1}$  and  $337 \pm 30 \text{ km s}^{-1}$  respectively. Using Xspec both measurements were well out of range of the  $1\sigma$  error given by the model. When observing systems with the maximum expected turbulent velocity the Xspec model is consistently within  $1\sigma$  or  $2\sigma$  of the true value while the `lmfit` model is not. The inaccuracies of both models appear to increase as the total number of photons decrease, as seen on the Hydra A North pointing. Even so it consistently shows that using the `lmfit` model is better for low velocity regions in clusters while Xspec should be used for high velocity regions in clusters. Since most of the injected values have been extracted within  $1\text{-}2\sigma$  error we have showcased the ability for models to be accurate in obtaining this data.

Each cluster is packaged in a separate proposal, each with different exposure times for differing pointings: MS0735 at 200ks, Hydra A at 100ks, Hydra A North at 200ks and A2199 at 50ks. Each proposal is under the total limit of 600ks per cluster and 300ks per pointing. These proposals were observed and graded in a rate of priority, with A2199 approved with an A rank under a different principal investigator, Hydra A's central pointing was approved with a B rank and its north pointing was given a C rank with both having Brian McNamara as the principal investigator. Unfortunately MS0735 was not put in the A01 Cycle approval list and will require another proposal in the next cycle. The Hydra A proposal was successful in showing that important data can be extracted from its pointings as it was approved and will be expected to produce data in the first quarter of 2025.

Both Hydra A and A2199 will be observed and added to the database of clusters. This database will be used to calculate the conversion of energy between radio jet power to the turbulent gas motions in the hot atmospheres of galaxy clusters. These clusters will be added to the data obtained from early XRISM target clusters such as M87, Perseus and A2029.

## 3.6 Future Work

As XRISM’s mission length is targeted to be 3 years this process of finding good candidate clusters must be repeated throughout the mission’s lifespan. These simulations must be made to observe if the luminosity of the Fe-K complex in clusters will be able to accurately measure the turbulent velocity broadening. If the gate valve opens this will increase the photon count in the Fe-K complex and can allow the usage other major lines, like the Fe-L complex or bright Si lines, as another method calculating the turbulent broadening within the cluster.

The `lmfit` model may require an update, the time constraints of the A01 cycle of proposals the model did not account for the natural line width of each Fe-K line. This needs to be studied to observe if there is a substantial effect adding the natural line width to the final turbulent velocity. The model requires adjustments to map out the other Fe-K lines within the complex, as previous iterations showed failures when attempting to model the complex in high turbulent velocity systems. This may explain the accuracy decrease in simulations with higher speeds.

# Chapter 4

## XRISM: A Study of M87 & Virgo's Intracluster Medium

*This chapter includes original research, using early access data from XRISM's first light, in particular from the M87 team headed by Aurora Simionescu. All X-ray data within this chapter was analyzed and produced by Neo Dizdar unless stated otherwise. As this chapter discusses data that is a current work in progress within internal teams results may change before these results are published.*

M87, a bright central galaxy located in the Virgo A subclump of the Virgo Cluster, is a high-priority performance verification phase target for XRISM. Brian McNamara and I are members of the M87 XRISM team, this team is provided access to the new data seen in this Chapter. The spectrum produced by M87 reveals emission lines of different metals with high spectral resolution with XRISM's microcalorimeter. Abundances, line widths, velocities, and bulk motions of each separate metal are observed. Some observations show that metals may be distributed inhomogeneously, depending on the temperature that the line forms at the gas may be moving at different velocities. This suggests that the conversion of the injected AGN jet energy to the gas motion kinetic energy depends on the temperature. Due to multiple available exposures of the Virgo cluster, radial and structural information of its hot atmosphere may be extracted from this data. The exposures obtained are centered on M87, on two extended arms, and on a shock front.

## 4.1 M87

The Virgo Cluster and M87 are objects that have caught the eye of the public in recent years due to the imaging of M87’s central black hole by the Event Horizon Telescope Collaboration [1]. M87 itself has been observed by multiple research teams, as it is one of the first extragalactic objects observed to emit X-rays. Different telescopes have observed M87 with a range of bandpasses, including CHANDRA, XMM-Newton and the Einstein Observatory. Its close proximity at  $16.7 \pm 0.9$  Mpc, and its large and distinct radio jets make it a key structure to study [6, 98, 109].

M87 hosts a FR-1 radio source. The centermost portion of the jet contains synchrotron “knots”. These knots appear as brighter X-ray sources in the jets, all extending radially away from the center. This cannot be resolved structurally in XRISM’s microcalorimeter as this structure is smaller than the pixels of the instrument (below 30 arcsec or 2.4 kpc). XRISM must observe a larger footprint. Four pointings were observed, with the positioning shown in Fig 4.1. The first pointing is centered on M87. The second and third are centered on two bright metal-rich outflows following the radio jets, which are structurally different in the X-ray spectrum. The fourth focuses on a shock front in the north-west; it is a low surface brightness region with slower turbulent motions. Lower luminosity regions will cause issues modelling the broadening components due to the lower signal-to-noise ratio. See Chapter 3 for examples.

Similarly to the selection criteria of the proposals in the previous chapter, M87 was selected because of its high X-ray luminosity and prominent radio source. M87’s jet power is  $8_{-3}^{+7} \times 10^{42}$  ergs s<sup>-1</sup> [30]. This jet power is expected to be comparable to the kinetic energy of the surrounding ICM.

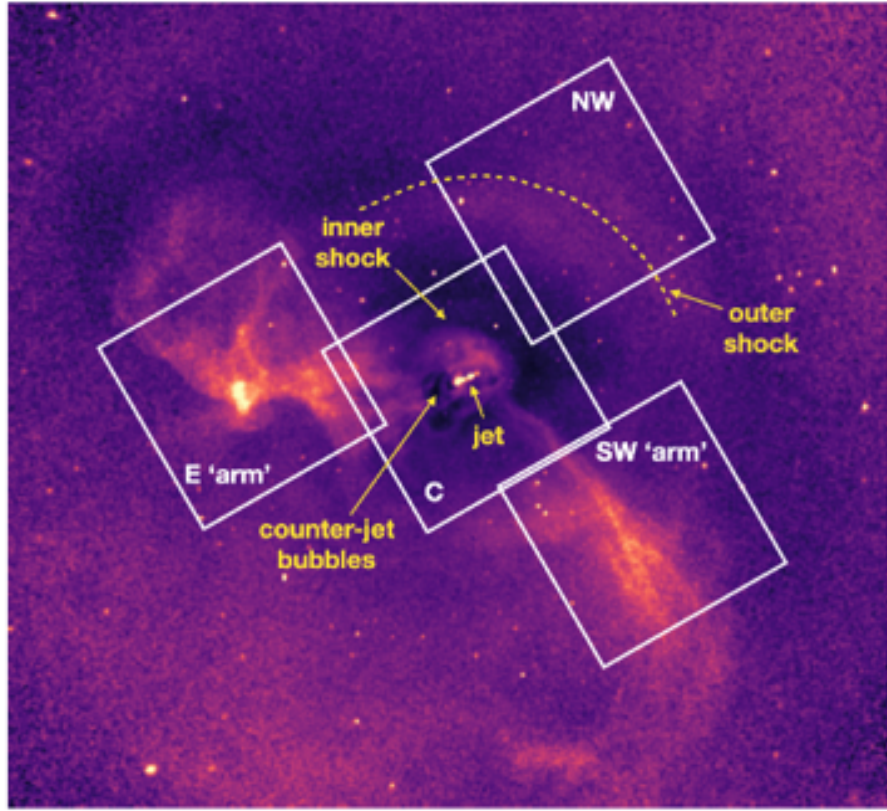


Figure 4.1: The four separate pointings of the early access data in for M87. Each pointing was selected to observe different components within the cluster: two dense arms in the surrounding ICM, a slow moving shock front and the central region of the cluster. As is expected the exposure time will vary between pointings, and some pointings will take multiple exposures which will be stacked to produce a long exposure. The south-west arm is currently missing an exposure, the second is scheduled for early 2025 and thus only has a single 70 ks spectrum taken. Image shown is produced by CHANDRA.

## 4.2 Data Extraction

The XRISM data are composed of five separate exposures ranging between 80 ks – 180 ks. Two exposures of the north-west shockfront were added together and reformatted in a single file. The extracted spectral data relates counts to energy channels. These energy channels are converted to electron volts by using a redistribution matrix file (RMF), which translates a channel to a unit of energy. Each pointing has a separate RMF and ARF associated with the data.

The ancillary response file (ARF) defines the weighting of photons on each pixel, accounting for the effective area of the telescope, failing pixels, gain, and pixel quantum effectiveness. Pixels may be removed to focus on specific extended structures. For example, on the north-west pointing it can roughly separate the inner and outer shock, allowing each component to be studied separately. ARFs must be defined before reading and calculating the data, as issues with gain histories on pixels may create artifacts.

Pixel 12, the calibration pixel, is turned off. Pixel 27 has issues with gain history and is removed from all observations. This reduces the available pixels for observation from 36 to 34 which removes  $\sim 6\%$  of the instrument’s footprint. Future proposals must take into account which pixels are faulty and adjust their roll angles to observe key structures. Once the RMF and ARF have been convolved with the initial unprocessed data, the spectrum can be modelled using thermal model spectra. The M87 team has created a set of RMFs, ARFs and spectral data files to be used mitigating possible sources of error between team members.

## 4.3 Observing Metals

Resolve’s spectral resolution is  $\sim 5$  eV. Metals that have visible spectral lines between 1.7 keV – 10 keV are Si, S, Ca, Ar, Fe, and Ni. These lines may have different velocities depending on where the spectral lines are found. Lower energy lines are produced by cooler gas. The cool gas is defined by a narrow bandpass of 2 keV – 3 keV, which includes mainly Si and S, while the hot gas is defined by a narrow bandpass of 6 keV – 7 keV, which is mainly Fe with some Ni. A clear difference in velocity, turbulent motion, or abundance between the metals found in the two bandpasses represents the differences in the motion between hot and cool gas.

Ar is the only noble gas in Resolve’s full bandpass. A noble gas is an important tool for searching for the depletion of metals in the cores onto dust grains. Because noble gases are inert and will not combine with other particles, the abundance of Ar should increase

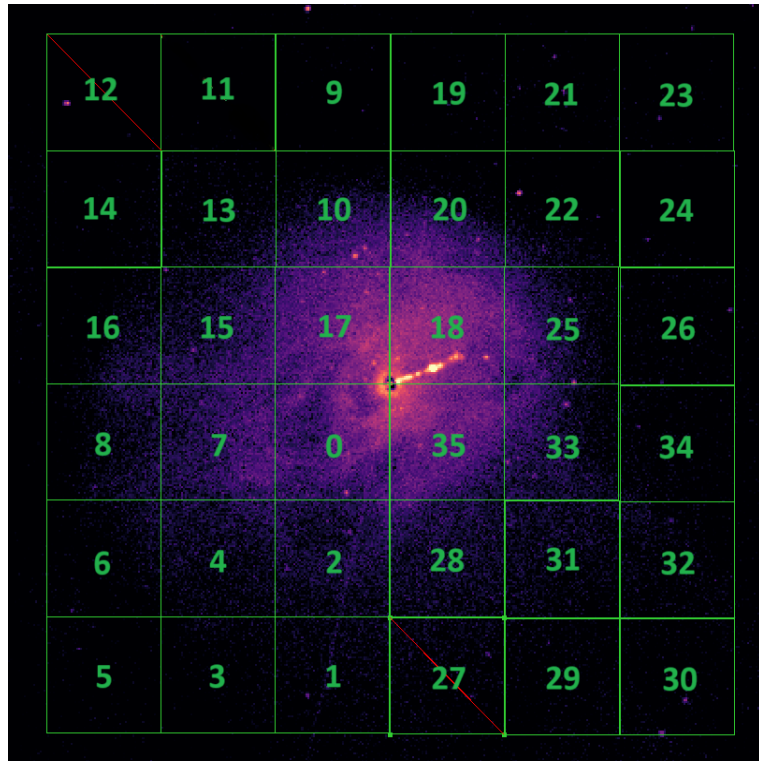


Figure 4.2: This is the format of the pixel names in Resolve, pixel 12 is taken out as an orientation pixel, while 27 is crossed out due to gain history issues. As this is over the centered pointing of a dimmed M87 it can be seen that small structures cannot be resolved with this instrument.

toward the core while the other metals show a drop in strength as they deplete onto dust grains.

Although modelling software can be used to obtain separate metal abundances over a broadband fit, a broadband fit does not account for the separate motion between metals. Models like `bvape` produce a single velocity broadening value and a single redshift for the entirety of the single pointing. To observe the motions of specific metals, separate models must be made on narrow bands that contain only the characteristic lines of that metal. Singular metal models are prone to overfitting or adjusting the rest of the cluster's components (like photon normalization) to unphysical levels. To mitigate overfitting an initial broadband fit with all abundances, photon normalization, temperature, velocity broadening, and redshift values are left to vary. Once an initial broadband model is produced, narrow band models are constructed off of these values, freezing the normaliza-

tion and other abundances not found in the narrow band limits. This process is repeated for each metal, yielding their redshift, velocity broadening, and abundance. Each narrow band contains an emission line with 100 eV – 150 eV surrounding the line. This bandpass accounts for clusters with high turbulent velocities or bulk velocity changes. Narrow band limits are shifted by the redshift of the cluster, and thus the broadband redshift must be calculated by the model first before producing the narrow band models. This is done by converting the redshift into a difference in wavelength and then using the photoelectric effect to convert this difference in wavelength to a shift in the eV limits. Repeating over each metal provides seven different models, one broadband model, and one for each metal: Si, S, Ar, Ca, Fe, and Ni. Each model yields the velocity broadening, the bulk velocity, and the abundance.

Narrow band Limits ( $z = 0$ )		
Element	Minimum keV	Maximum keV
S	1.8	2.4
Si	2.4	3.0
Ar	3.0	3.7
Ca	3.7	4.7
Fe	6	7
Ni	7.4	8.2

Table 4.1: Bandpasses that encompass emission lines of each metal. The energies are restframe values. [32]

## 4.4 Model Selection

A baseline model was tested, with the self made lm\_fit model from Chapter 3 not discussed as it has yet to be used on a full spectrum. The two tools are Xspec, an X-ray fitting package developed by NASA’s Heasarc team, and SPEX, an X-ray fitting package developed by SRON. Both are used for high-resolution spectral modelling. Due to slight differences in models available and databases available, it is expected that values between the two packages will differ.

With Xspec the selected model type is the `TBabs*(bvapc+powerlaw)` model, which allows separate abundances for each metal to be measured and to measure the total broadening of the spectrum. The AGN adds a non-apc component onto the model, and these

nonthermal photons produced by the AGN can be modelled as a powerlaw instead. The powerlaw component is scaled by two variables, the photon index and the normalization. Due to known modelling issues between the two components, the photon index is fixed at a value of 2.38, with the normalization allowed to vary. The `TBabs` model only requires a hydrogen density value to account for X-ray absorption, which is provided by HEASARC’s H column density tool. This hydrogen column density value is calculated from line-of-sight observations in IR and H I line measurements. Most components are dependent on the AGN normalization and `bvapec`’s abundances and velocities. The free parameters of the `bvapec` model are: the six metal abundances, the turbulent broadening velocity, the temperature, the normalization, and the redshift of the cluster. One broadband fit was made between 1.7 keV – 10 keV, then using the values produced by the broadband and Table 4.1 narrow band limits, the additional narrow band models were produced. For each narrow band the other abundances were frozen; the model provides the turbulence, gas temperature, and redshift values of that metal. The redshift can be used to extrapolate a bulk velocity, obtaining the bulk velocity of the entire cluster and the bulk velocity of specific metals through this process. This model does not yet contain a non-X-ray background component, since it is faint and can be ignored.

For the SPEX model, the selected model was `reds hot cie` with a powerlaw component to account for the AGN emission. The `reds` component defines the redshift of the model and scales the other three components. With the initial redshift being defined by the NASA Extragalactic Database’s value of the BCG, the component would be left free to vary around 0.004283 [46]. The `hot` component defines the collisional ionization equilibrium absorption model, similar to `TBabs`, wherein the hydrogen column density must be defined and left frozen. The `cie` component defines the emission of gas at collisional ionization equilibrium, similar to the `bvapec` component in the Xspec model. The difference between the two models is that `cie` can define the temperature broadening of a line and can produce a two-temperature model. For preliminary testing, the models have been restricted to 1-temperature models, which means that the `cie` model must combine the 2-temperature variables, transforming the 2-T model into a 1-T model. There are multiple abundance tables available to relate the metals to solar values, and as a standard within the team, the Lodders (2009) abundance table will be used [60]. With the same tables it is still expected that there will be differences output the two models due to the spectral line databases used: AtomDB for Xspec and SPEX’s internal database.

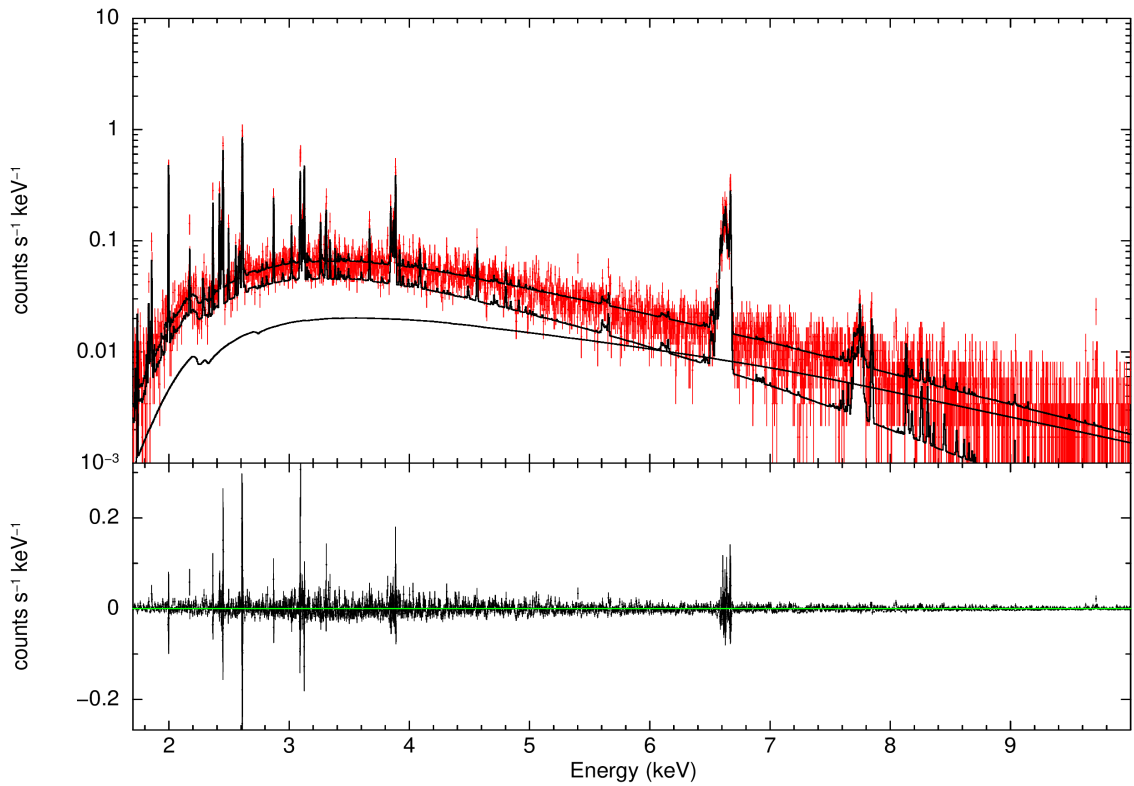


Figure 4.3: The model components of Xspec onto the central pointing of M87. The upper black line is the combination of both components, the lower line with now line features represents the powerlaw component and the TBabs\*bvape component is the middle black line. The lower graph shows the residual between the model and the spectral data.

## 4.5 Data Analysis

Post-processing data are provided as five different exposures: two exposures for the north-west pointing and one exposure for the others. Exposure times: 120 ks central, 160 ks eastern arm, 180 ks north-west pointing, and 80 ks south-west arm. The south-west arm was allocated a 150 ks exposure, but time constraints required a second exposure to be taken in early 2025. The northwestern pointing contains a combination of two different exposures, totaling 180 ks.

For each pointing several iterations of Xspec and SPEX models were produced. Both created a broadband model yielding values for metal abundances, total turbulent broadening, gas temperature, and redshift. This process was repeated using the values of the broadband model as initial conditions and applied to the bandpasses defined in Table 4.1. The narrow band spectra provided data on the motions and abundance of each metal line.

The models apply Poisson statistics (cstat) to define goodness of fit, producing a  $1\sigma$  error estimation for each free parameter. Initial tests varied the AGN photon index, but varying the AGN photon normalization yielded unphysical abundances. Other tests included allowing the temperature to vary in the narrow band fits or fixing it to the broadband fit. Both methods provided unphysical velocity widths for specific metals with low photon counts, therefore all tests were run with varying gas temperature values and a fixed AGN photon index.

The redshift is used to define the bulk velocity of the gas with respect to the cluster. This is done using the redshift of M87:  $0.004283 \pm 1.7 \times 10^{-5}$ . The comparison of redshifts in broadband and narrow bands provided the average bulk motion and specific motions of different metals. This method can be used to observe whether the motion of cooler gas is decoupled from the motion of warmer gas in the four different pointings.

### 4.5.1 SPEX or Xspec

Prior to defining final values of the cluster's metallicity and motion, a modelling package must be chosen. Although both Xspec and SPEX provide individual values for the cluster and the model types are similar, there are distinct differences in their outputs. Comparing the Fe narrow band values of the central pointings shows this difference best:

M87 Center Pointing (Fe Narrow band)			
Model	Redshift ( $\times 10^{-3}$ )	Fe $Z_{\odot}$	$\sigma_{\text{turb}}$ (km/s)
SPEX	$4.32 \pm 0.04$	$0.98 \pm 0.06$	$163 \pm 15$
Xspec	$4.32 \pm 0.04$	$1.49 \pm 0.04$	$125 \pm 13$

Table 4.2: Output parameters for SPEX and Xspec Fe narrow band models. Shown above is the redshift, metallicity and turbulent velocity observed between 6-7 keV in the center pointing. Note the differences in abundance and turbulence.

The two models output values that do not show an overlap within  $1\sigma$  and in many cases  $3\sigma$  as can be seen in Table 4.2 and Fig 4.4. Selecting a model is important because they define the metallicity and velocity values of the cluster. Modelling the spectrum produced by M87 CHANDRA data provides an abundance between  $1.5Z_{\odot} - 1.7Z_{\odot}$  in the central pointing. This is expected as the central 7 kpc of M87 is a metal rich region, thus super solar values from Xspec ( $1.49 Z_{\odot}$ ) should be trusted over the SPEX value ( $0.98 Z_{\odot}$ ). This in conjunction with the M87 team presenting findings that the central pointing has a broadband turbulent velocity of  $130 \pm 14$  km s $^{-1}$  suggests errors in the SPEX build. This difference is unexpected, as a SPEX `hot cie` model should be very similar to an Xspec `TBabs*bvapec` model, especially since they both start with the same initial conditions. SPEX data will not be used due to these differences; all future models will be produced by Xspec until a new SPEX build is released.

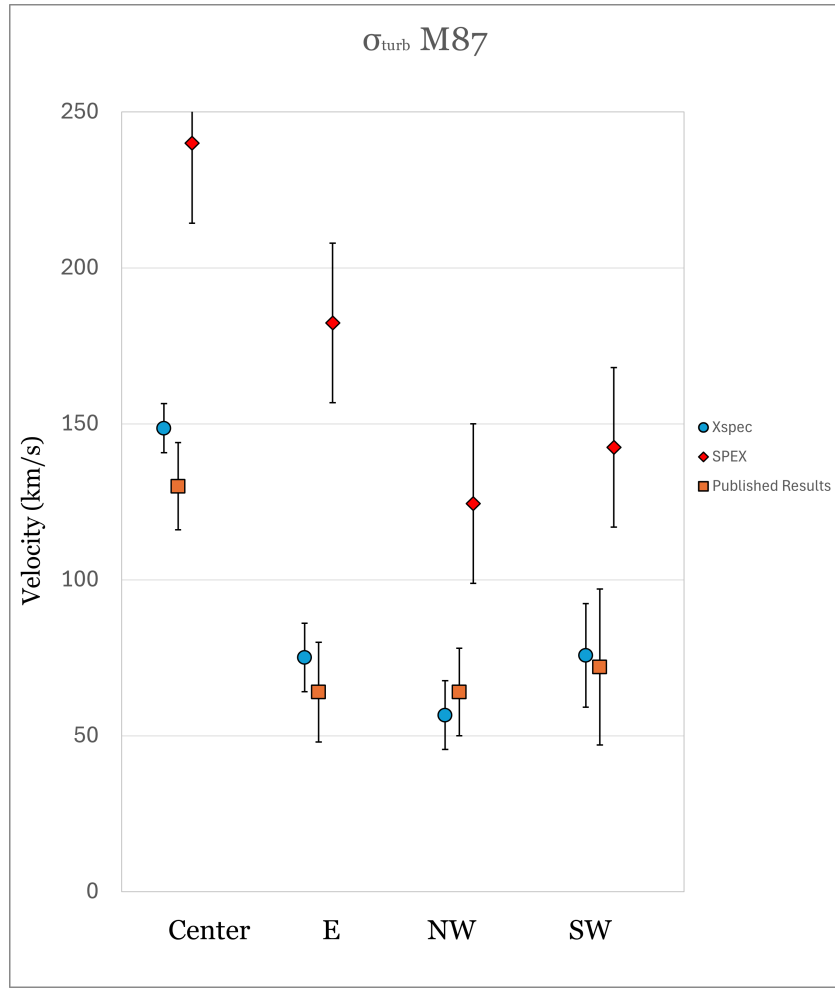


Figure 4.4: Broadband turbulent velocities in each pointing. The orange points are presented findings from other members in the M87 XRISM team. Both SPEX and Xspec models should reproduce these values, but it appears that the SPEX model is not within  $1\sigma$  of these findings.

#### 4.5.2 Metallicities

Each spectrum contains emission lines for S, Si, Ar, Ca, Fe, and Ni. The Xspec model uses the Lodders (2009) abundance table to redefine abundances to Solar values [60]. By producing a model for a broadband and a narrow band spectrum two sets of metallicities are produced for each element.

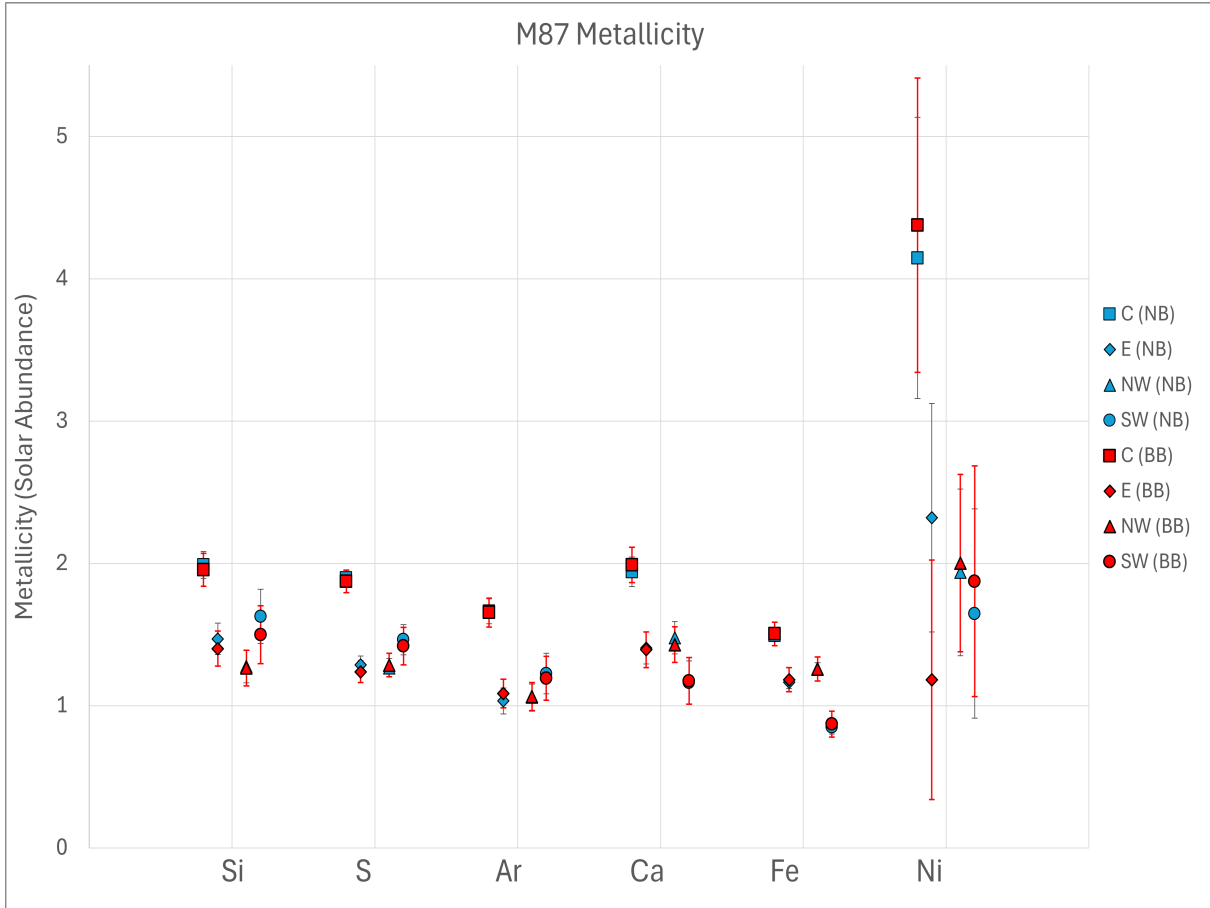


Figure 4.5: The metallicities of the four pointings with six elements. The pointings go in order from left to right: Center (C), East arm (E), North-west (NW) and south-west arm (SW). The blue datapoints represent the narrow band values, while the red represent the broadband values.

The gas metallicity within the central pointing has a higher metallicity than the outer pointings. This is consistent with the trends found in cool core clusters. Fig 4.5 shows the effects of using narrow bands for abundance measurements. Most values are found within  $1\sigma$  of the broadband. But the narrow band errors are smaller. The only points in which the narrow band and broadband abundances diverge beyond  $1\sigma$  are regions that have lower total photon counts, such as Ni. This systematic effect on Ni will consistently yield unrealistic values, Ni values can be ignored. All observed metals have super solar values, this is expected in the center pointing but in the outer pointings there should be a greater decline towards  $0.3 Z_{\odot}$ . A steeper decrease towards  $0.3 Z_{\odot}$  should be seen if more pointings were proposed further from the center.

The south-west arm shows a metallicity trend. Metals forming in cooler gas, Si, S, and Ar, have higher abundances than the east arm and north-west shockfront, two pointings at the same radial distance away from the center of the cluster. The metals formed in hotter gas, Ca and Fe, appear to be diminished within this region in relation to the other pointings. The south-west arm appears to be a separate structure that has a higher ratio of cooler metals than the rest of the cluster.

Argon's abundance ratio probes for a dusty core. Dust may be the cause of the extinction of metals in the core of a cluster. Ar does not form a compound with dust as a result of its inert properties. Observations of depletion in other metals as the Ar abundance increases would suggest a dusty core. The central pointing values do not show this depletion, suggesting that there is no dusty core or that it cannot be seen using XRISM's footprint. Chandra observations show depletion within the inner 3 kpc and cannot be observed using XRISM's footprint, which encompasses the inner 7 kpc of the cluster. Dividing the central pointing and observing the inner 4 pixels may show a depletion in metallicity. Decreasing the number of pixels used does increase the error on abundances due to lower photon counts.

### 4.5.3 Turbulent Broadening

M87 Velocity Width							
Pointing	Broadband (km/s)	Si (km/s)	S (km/s)	Ar (km/s)	Ca (km/s)	Fe (km/s)	Ni (km/s)
Center	$149 \pm 8$	$148 \pm 29$	$166 \pm 14$	$166 \pm 19$	$124 \pm 21$	$126 \pm 13$	$149 \pm 50$
E arm	$75 \pm 11$	$149 \pm 49$	$153 \pm 25$	N/A	$68 \pm 37$	$59 \pm 14$	N/A
NW	$57 \pm 11$	$64 \pm 100$	N/A	N/A	$120 \pm 30$	$56 \pm 12$	N/A
SW arm	$76 \pm 17$	$127 \pm 85$	$109 \pm 46$	$41 \pm 98$	$86 \pm 53$	$62 \pm 20$	N/A

Table 4.3: Extra thermal velocity values produced by a TBabs\*bvape Xspec model. Each value is a separate model, showing the turbulent velocity broadening on each separate metal. N/A is attributed to unphysical values and can be ignored.

The central pointing has a higher turbulent velocity in both broadband and narrow band values compared to the outer pointings. This increase correlates with the injection of kinetic energy from the AGN and is consistent with the data of clusters from other XRISM teams. The turbulent speeds of the central region are  $149 \pm 8 \text{ km s}^{-1}$ . The outer arms have an atmospheric turbulent speed lower than  $\sim 75 \text{ km s}^{-1}$ , a value expected from a cluster with a jet power of  $8 \times 10^{42} \text{ erg s}^{-1}$ . The north-west pointing shows the narrowest velocity width with an average velocity of  $57 \pm 11 \text{ km s}^{-1}$ . This test also shows that Ni is a poor probe of metallicity and motion. The outer pointings have too few photons to provide a successful fit. The N/A values define velocities with unphysical error bars due to low photon counts. This implies weak lines for S, Ar, and Ni in the outer pointings.

There is a contrast between the lines produced by hotter and cooler gases in their turbulent motions. Si and S, with emission lines that are produced by cooler gas, both have similar turbulent velocities in all four pointings. Ca and Fe, with emission lines that are produced by hotter gas, appear to have similar separate turbulent velocities. The broadening value of Fe is consistently within  $1\sigma$  of Ca for all pointings except the north-west shock. This further implies that the motions of cooler and hotter gases are separate, as the hotter gas shows a slower turbulent velocity.

#### 4.5.4 Bulk Motions

The bulk velocity is a measure of gas flow in the intracluster medium. To find the bulk velocity of Virgo cluster's ICM the speed of different regions of gas is given with respect to the redshift of M87. This process is done by fitting a model upon the spectra of different pointings and extracting the model's calculated redshift. XRISM's high spectral resolution is unique to this calculation, as it can also obtain the redshifts of the separate metals in a spectrum. This provides insight into the total motion of gas and the motions of specific metals within the cluster. As there may be bulk velocity in the central X-ray gas, the baseline of the proper motion of the cluster is at a heliocentric redshift of  $0.004283 \pm 0.000017$ , the redshift of the BCG [46].

Virgo Cluster Bulk Motion with respect to M87							
Pointing	Broadband (km/s)	Si (km/s)	S (km/s)	Ar (km/s)	Ca (km/s)	Fe (km/s)	Ni (km/s)
Center	$-8 \pm 7$	$-20 \pm 18$	$-18 \pm 11$	$-31 \pm 14$	$15 \pm 15$	$10 \pm 12$	$77 \pm 39$
E arm	$4 \pm 8$	$46 \pm 28$	$11 \pm 17$	$11 \pm 18$	$41 \pm 18$	$-15 \pm 10$	$-36 \pm 25$
NW	$-23 \pm 8$	$-55 \pm 30$	$-40 \pm 16$	$7 \pm 17$	$-24 \pm 21$	$-16 \pm 9$	$-76 \pm 24$
SW arm	$-56 \pm 11$	$-141 \pm 41$	$-58 \pm 23$	$-70 \pm 24$	$-18 \pm 30$	$-46 \pm 15$	$-63 \pm 39$

Table 4.4: Velocity speeds produced by converting the fitted redshifts of the cluster's spectra. This was produced by a TBabs\*bvape model on broadband and narrow band data. The errors are c-stat  $1\sigma$  model errors convolved with the redshift error found in the NASA Extragalactic Database.

The calculated bulk motions do not take into account the orbital speed of the telescope. A heliocentric correction must be made to offset the effects of the orbit of Earth and the orbit of the telescope. Using the orbital velocity formula and XRISM's orbital altitude of 575 km [112] the correction range is found to be between  $\pm 37.4 \text{ km s}^{-1}$ . Inputting the observation times tied to the exposures into astropy's velocity correction tool provides a heliocentric correction from  $-28.4 - -24.9 \text{ km s}^{-1}$ . Since the north-west pointing is made of two combined exposures on different days, the correction was averaged between the two dates.

Virgo Cluster Heliocentric Bulk Motion with respect to M87							
Pointing	Broadband (km/s)	Si (km/s)	S (km/s)	Ar (km/s)	Ca (km/s)	Fe (km/s)	Ni (km/s)
Center	-37 ± 7	-48 ± 18	-46 ± 11	-60 ± 14	-13 ± 15	-18 ± 12	48 ± 39
E arm	-22 ± 8	19 ± 28	-15 ± 17	-15 ± 18	15 ± 18	-41 ± 10	-61 ± 25
NW	-48 ± 10	-80 ± 32	-65 ± 18	-18 ± 19	-49 ± 23	-40 ± 11	-99 ± 26
SW arm	-83 ± 11	-168 ± 41	-85 ± 23	-96 ± 24	-45 ± 30	-72 ± 15	-89 ± 39

Table 4.5: Heliocentric corrected bulk velocities of the ICM in different pointings. The correction was between -28 and -24 depending on the observation time. The north-west pointing is a combination of two exposures, increasing the error in the velocity correction.

$$v_{\text{bulk}} = (z_{\text{obs}} - z)c + v_{\text{corr}} \quad (4.1)$$

Using the heliocentric velocity correction shows that a majority of the gas in all four pointings is blueshifted in relation to the known position of the BCG. The arms of the cluster show that they were fired in opposing directions in the plane of the sky. This is shown by the south-west arm being the most blueshifted ( $-83 \pm 11 \text{ km s}^{-1}$ ) while the east arm is the least blueshifted ( $-22 \pm 8 \text{ km s}^{-1}$ ) with some narrow band values like Si and Ca showing slight redshifts. It appears that the cooler softband metals (Si and S) move at a higher bulk velocity than the warmer metals (Fe and Ca). This trend can be seen in the central and north-west pointings but also appears in the south-west arm to a lesser extent.

Nickel also proves to be a poor probe for obtaining bulk velocity information. This is expected as the model failed to fit its turbulent velocities in most pointings. The only fit that was successful was in the central pointing, yet the bulk motion of Ni is the only heavily redshifted value ( $48 \pm 39 \text{ km s}^{-1}$ ). Being an outlier suggests that the values found for Nickel should be removed.

## 4.6 Jet Energetics

The energy conversion of the injected AGN jet energy to the gas motion requires the values of turbulent broadening speed in the gas and a mean jet power. Forman's (2003) results state that the power driving M87's shock, the minimum jet power, is injected at a rate of  $\sim 2.4 \times 10^{43}$  ergs s<sup>-1</sup> [31]. This value will be compared to the center pointing, a region where jets dominate gas motion. Since the kinetic energy of an ideal gas is proportional to the total gas mass, this requires a mass profile of the Virgo cluster. Using a M87 mass profile in the ACCEPT database, it is found that the inner 7 kpc (the radius of the central pointing) of the Virgo cluster contains  $(6.8 \pm 0.3) \times 10^{11} M_{\odot}$ , and the gas mass was estimated to be  $(1.3 \pm 0.2) \times 10^{10} M_{\odot}$  of gas [13, 45, 65]. The kinetic energy of a gas is defined by:

$$E_{\text{gas}} = \frac{1}{2} M v_{\text{rms}}^2. \quad (4.2)$$

This assumes that the velocity is a value in 3-dimensional space. The turbulent velocity found in Section 4.5.3 is a projected value, therefore it is a 1-dimensional value and does not account for motions parallel to the plane of the sky. With no external forces, the turbulent gas motions can be approximated to be spherically symmetric, simplifying Eq. 4.2 to:

$$E_{\text{gas}} = \frac{1}{2} M (\sigma_x^2 + \sigma_y^2 + \sigma_z^2) = \frac{3}{2} M \sigma_{\text{turb}}^2. \quad (4.3)$$

Assuming that the velocity width represents only isotropic turbulence, this equates to a total of  $(8.7 \pm 0.5) \times 10^{57}$  ergs of turbulent kinetic energy in the gas. The comparison of total turbulent kinetic energy to jet power requires an energy injection timescale for turbulent motions of the gas. Since it is assumed that the kinetic energy in the gas offsets the cooling, the cooling timescale of the gas can be used as the timescale of turbulent motions. The cooling timescale of this observation changes depending the distance from the center of the cluster (see Fig 4.6), therefore the selection of the timescale will change the overall power in turbulent motions. Using the cooling time at the maximum radius of the center pointing (7.04 kpc):  $1.9 \times 10^{16}$  s, the kinetic energy in the gas is  $(4.5 \pm 0.1) \times 10^{41}$  erg s<sup>-1</sup>. This overestimates the cooling time for the gas located in the inner 7 kpc. Instead, by taking the average of each measured point within 7 kpc in Fig. 4.6 provides a flux-weighted average cooling time:  $1.0 \times 10^{16}$  s. This cooling time produces  $(8.5 \pm 0.2) \times 10^{41}$  erg s<sup>-1</sup> of turbulent power in the atmosphere. This would imply a poor conversion rate between jet power and the kinetic energy in the gas, as only  $\sim 3\%$  of the minimum jet power used to drive the shock in M87 is converted into turbulent kinetic energy. Rafferty

(2006) instead suggests that the power found in M87’s cavities, a proxy for mechanical jet power, is  $6 \times 10^{42}$  ergs s $^{-1}$  [90].

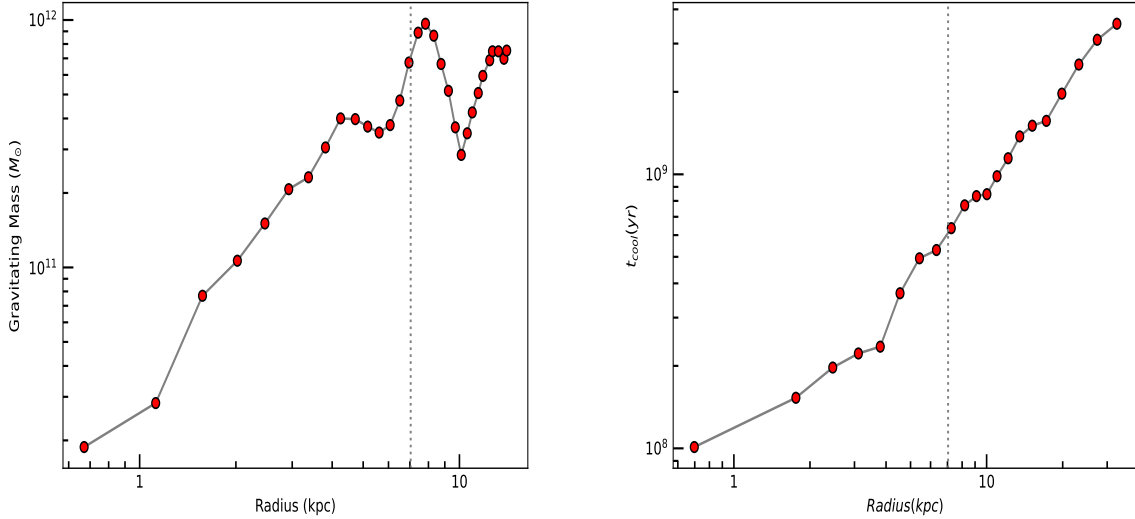


Figure 4.6: Total mass and gas cooling time profiles of the Virgo Cluster. Both graphs denote the radius of the center pointing with a dotted vertical line. Data for the cooling time profile (right) was obtained from the internal database, data for the mass profile (left) was provided by the ACCEPT database [13].

Another approach is to use the jet timescale, an equation that requires measured jet length. CHANDRA observations find the jet length to be around  $\sim 1.6$  kpc [100]. Since the jet can be observed within the center pointing, this length scale is expected.

$$\tau_{\text{jet}} = \frac{l_{\text{jet}}}{\sigma_{\text{turb}}} \quad (4.4)$$

The jet timescale is equivalent to  $(3.4 \pm 0.3) \times 10^{14}$  s. Using this timescale for the injected energy equates to a total of  $(2.8 \pm 0.4) \times 10^{43}$  ergs s $^{-1}$ . A value within the range of the minimum jet power found in Forman (2003) [31]. It is uncertain which timescale is correct to calculate the turbulent kinetic power in the atmosphere surrounding M87. A final method of comparing values can be done by comparing the total calculated energy of the gas and the jet. Rafferty finds  $8 \times 10^{56}$  ergs assuming a 4pV cavity, while Forman states that  $8 \times 10^{57}$  ergs was injected to push the outer shocks. This aligns with Forman’s

values, suggesting that the jet-length timescale was used to define the power of the jets. As these results use an estimated mass within the inner 7 kpc they may be incorrect, and future studies will require a clear gas mass profile of M87.

## 4.7 Conclusion

Utilizing XRISM’s IFU over four major structures in M87 provides high-resolution data to extrapolate the metallicity and motions of the gas within the cluster. The four pointings are aligned with the center of the cluster, the two offset x-ray arms, and a shock front. With XRISM’s high spectral resolution of 5 eV, the abundances and motions of separate metals can be observed. The metals above the gate valve filtering limit of 1.7 keV are S, Si, Ar, Ca, Fe and Ni. Each spectrum is modelled with a single temperature `TBabs*(bvape + powerlaw)` model to account for both the emissions of the ICM and the photons produced by the AGN. Nickel does not have enough photons to properly fit its characteristic x-ray emission lines and will not be further discussed.

All pointings show that the metallicity is above solar values, with the center of the cluster having the highest abundance of metals. This is consistent with previous observations of cool core clusters, wherein the metallicity rises towards the core and may drop within the inner 1-3 kpc of some clusters. The east arm and north-west pointing show similar abundances in every metal. The south-west arm shows a change in the metallicity trend, it has a higher abundance of cooler metals: Si, S and Ar, while the hotter metals have a lower abundance than the other pointings. This shows that the south-west arm is comprised of a higher ratio of cooler metals than the rest of the cluster. Observations of Ar do not show the signature of a dusty core; this may be due to the footprint of XRISM’s pointings being too large to observe the central drop in the abundances of the other metals.

The broadband turbulent broadening velocity shows higher speeds in the center pointing at  $\sim 149 \text{ km s}^{-1}$ . The outer pointings have a lower turbulent velocity, with the arms of the cluster both at  $\sim 75 \text{ km s}^{-1}$  and the outer shock being the most relaxed at  $\sim 57 \text{ km s}^{-1}$ . The extrathermal velocity of the gas in M87 is very low compared to other clusters, such as Cygnus A, with its expected turbulent broadening velocity of  $2000 \text{ km s}^{-1}$ . The narrow band values show that the cooler softband metals are more turbulent than Ca and Fe in the center, north-west and south-west pointings. This difference is consistently between  $20 - 40 \text{ km s}^{-1}$ , which implies a systematic difference between the motions of hotter and cooler gases in the ICM.

The bulk velocity of the ICM is obtained by relating the difference between the redshift of the gas and the known redshift of the BCG. The ICM is completely blueshifted as it has

a negative bulk velocity in all four pointings. The south-west arm is the most blueshifted with a bulk velocity of  $-83 \pm 11$  km s $^{-1}$  and the east arm is the least blueshifted with a bulk velocity of  $-22 \pm 9$  km s $^{-1}$ . The central and north-west pointings appear to have a similar bulk velocity around -40 km s $^{-1}$ , suggesting that the arms are not fully parallel to the plane of the sky. The small bulk velocities also imply that the BCG might be oscillating around the center of the gravitational well, causing the atmosphere to be blueshifted in comparison to its position. Again, there is a distinction between the cool softband metals and the warmer metals, the softband metals appear to be moving at a higher speed. This can be seen in the central, north-west, and south-west pointings, where the softband metals flow 15 – 30 km s $^{-1}$  faster than the hotter metals.

The south-west arm is a unique structure with a higher ratio of softband metals flowing at a higher bulk velocity than the rest of the cluster. The data also shows that in most pointings, aside from the east arm, the cooler metals and hotter metals must be grouped separately. This is due to their differences in motion as the cooler softband metals (Si, S and Ar) have higher turbulent speeds and higher bulk velocities than the hotter metals (Fe and Ca). This further suggests a need for two temperature modelling to account for changes in metallicity between the two groups of metals observed. An open gate valve may further highlight this difference as cooler gases with higher emissivity will assist in modelling lower energies, unfortunately they have been attenuated.

Observations of the jet and gas energetics show that the gas motions have a kinetic energy of  $(8.7 \pm 0.5) \times 10^{57}$  ergs. This is reflected in the jet energy used to drive the outer shocks of the cluster,  $\sim 8 \times 10^{57}$  ergs. The power of the gas motions depends on the selected timescale, relating the timescale to the cooling time of the gas shows a poor conversion of energy, and using the jet-length timescale instead shows equivalent powers between the jet and gas. These results are heavily dependent on the mass of the gas within the central pointing, and therefore gas mass profiles are required for future work in this field.

# Chapter 5

## Conclusion

In this thesis I studied the abundances of metals and flows of X-ray photon-emitting gas in galaxy clusters. This thesis focuses on the transition from CHANDRA data to XRISM, allowing for a deeper analysis of X-ray spectra through its high spectral resolution. I show the process of extracting CHANDRA data, converting to simulated XRISM data and doing a analysis of early XRISM images. In each instance the spectra produced is studied and modelled using different fitting programs (Xspec, SPEX, and lmfit) to obtain metal abundance values and turbulent gas velocities. By understanding the metallicities and flows of the intracluster medium, we begin to produce data that can be used to gain information about the evolution of clusters.

Using CHANDRA, a subset of 16 clusters was studied using radial spectral extraction. Annular rings were made around clusters, each producing a spectrum that was fitted using Xspec. Each spectrum provides metallicity, temperature, and flux, creating multiple radial trends per cluster. The cool core clusters in the dataset have metallicities that peak at a radius between  $0.008 - 0.05 r_{2500}$ , while the metallicity asymptotes to  $0.3 Z_{\odot}$  in the outer regions of all clusters. This result is consistent between clusters and is independent of the cluster redshifts (between  $z = 0.01 - 0.54$ ). This bolsters early enrichment theories since the metallicity is higher than what standard supernova metal production rates would predict. Six out of eleven cool core clusters show a significant depletion of metals in their cores. This result suggests that there are dust grains in the central regions of the cluster that can combine with the cooled-out ions. These particles would not emit high-energy photons, removing the metals from being detected by CHANDRA. This dataset also showed no clear trends between the metallicity and the star formation rates of clusters. With this small subset of clusters, it was also discovered that Abell 3571 and Abell 2142 show radial metallicity trends that do not align with standard clusters in their core temperature category.

Abell 3571 shows an increase of metal abundance towards the core with a temperature profile similar to most non-cool core clusters, while Abell 2142 shows the opposite, a cool core cluster with no increase in metallicity.

Using XRISM's 2.9 x 2.9 arcmin footprint on the 16 clusters in the dataset, I obtained the expected amount of flux and metallicity that would be observed by XRISM. Simulations of Hydra A, MS0735 and Abell 2199 were produced by upscaling the spectra extracted from this footprint, improving the spectral resolution from 95 eV to 5 eV. The three clusters were selected due to their flux, known jet energies, and theoretical turbulent motions. Using a limit of  $\geq 150$  Fe-K photons in simulations under 200 ks, it was found that Hydra A outputs enough photons in an additional offset pointing (centered on a large cavity) to propose two pointings. The modelling software was tested by injecting a known turbulent velocity into the simulation, fitting the model on the simulated Fe-K complex, and comparing the model's turbulent velocity output. These simulations found that the `lmfit` model can extract within  $1\sigma$  the turbulent velocity at lower speeds ( $\sim 100$  km s $^{-1}$ ) in the 3 clusters, while Xspec is a better tool for simulations at higher speeds ( $\geq 300$  km s $^{-1}$ ). These findings were reformatted into proposals for the A01 cycle of the XRISM mission. Both Hydra A pointings were proposed and accepted with a higher priority on the central pointing, Abell 2199 was accepted under a different principal investigator, and MS0735 will need to go through the next cycle of proposals.

Finally, I provided a deep analysis of early-release XRISM data for the Virgo cluster. There are 4 pointings in the cluster, a central pointing, and 3 pointings radially equidistant from the center observing different structures in the cluster. The inner pointing showed an increase in metallicity for all 6 observed metals (Si, S, Ar, Ca, Fe, and Ni), which is consistent with expected results for a cool core cluster. The metallicities in the outer pointings were mostly super-Solar, with only the south-west arm showing sub-Solar values for non-softband metals (Ca and Fe). There were no results showing a depletion of metals in the core of the cluster; this suggests that there are no dust grains that block X-ray emissions. The image resolution limits the preliminary results to observing the entirety of the inner 8 kpc. The signature depletion of metals in the inner 1 kpc – 3 kpc for a dusty core may be drowned out by the surrounding metal rich environment.

The turbulent velocity of the center of the Virgo cluster is  $146 \pm 8$  km s $^{-1}$ , which is produced by a jet with a power of  $8 \times 10^{42}$  erg s $^{-1}$ . Beyond the central churned regions, the ICM's turbulent speeds lower to  $\sim 75$  km s $^{-1}$  in the arms and  $57 \pm 11$  km s $^{-1}$  in the shock front. These speeds are very low in comparison to the simulated clusters, as is expected due to its weaker jet power. The narrowband broadening values show that, in the center pointing and the arms, the softband metals found in cooler gas (Si, S and Ar) are moving at a higher turbulent velocity than Fe and Ca: a  $20 - 90$  km s $^{-1}$  difference.

This separation between metals found in hotter and cooler gases appears in the bulk velocity of the gas, as the cooler gas appears to be more blueshifted (by  $15 - 30 \text{ km s}^{-1}$ ) than the hotter gases in the center, southwest arm and northwest shock. The cluster has a small blueshifted bulk flow in comparison to the position of the BCG, implying that the BCG is oscillating around the center of the cluster's gravitational potential well. The south-west arm is the most blueshifted ( $\sim -80 \text{ km s}^{-1}$ ) while the east arm is the least ( $\sim -20 \text{ km s}^{-1}$ ) suggesting they were fired in opposing directions into the plane of the sky. These observations show that it is necessary to separate the motions of hotter and cooler gas in the cluster.

The gas motions near M87 have a total kinetic energy of  $(8.7 \pm 0.5) \times 10^{57} \text{ ergs}$ . This is equivalent to the jet power calculated by Forman (2003),  $8 \times 10^{57} \text{ ergs}$ , and above the jet power calculated by Rafferty (2006):  $8 \times 10^{56} \text{ ergs}$ . This suggests that the conversion of energy between the jet and gas motions is efficient; therefore, turbulence is a strong contender to offset cooling in clusters.

# References

- [1] Kazunori Akiyama, Antxon Alberdi, Walter Alef, Juan Carlos Algaba, Richard Anantua, Keiichi Asada, Rebecca Azulay, Uwe Bach, Anne-Kathrin Bacsko, David Ball, et al. The persistent shadow of the supermassive black hole of m 87-i. observations, calibration, imaging, and analysis. *Astronomy & Astrophysics*, 681:A79, 2024.
- [2] Edward Anders and Nicolas Grevesse. Abundances of the elements: Meteoritic and solar. *Geochimica et Cosmochimica acta*, 53(1):197–214, 1989.
- [3] Keith Arnaud, Ben Dorman, and Craig Gordon. An x-ray spectral fitting package, 2003.
- [4] M Arnaud, R Rothenflug, O Boulade, L Vigroux, and E Vangioni-Flam. Some constraints on the origin of the iron enriched intracluster medium. *Astronomy and Astrophysics, Vol. 254, NO. FEB (I), P. 49*, 1992, 254:49, 1992.
- [5] Stefano Bianchi, Giorgio Matt, Fabrizio Nicastro, Delphine Porquet, and Jacques Dubau. Fe xxv and fe xxvi lines from low-velocity, photoionized gas in the x-ray spectra of active galactic nuclei. *Monthly Notices of the Royal Astronomical Society*, 357(2):599–607, 2005.
- [6] Sarah Bird, William E Harris, John P Blakeslee, and Chris Flynn. The inner halo of m 87: a first direct view of the red-giant population. *Astronomy & Astrophysics*, 524:A71, 2010.
- [7] L Bîrzan, David A Rafferty, BR McNamara, Michael W Wise, and Paul EJ Nulsen. A systematic study of radio-induced x-ray cavities in clusters, groups, and galaxies. *The Astrophysical Journal*, 607(2):800, 2004.

- [8] Roger D Blandford and Roman L Znajek. Electromagnetic extraction of energy from kerr black holes. *Monthly Notices of the Royal Astronomical Society*, 179(3):433–456, 1977.
- [9] Hans Böhringer, Gayoung Chon, and Masataka Fukugita. The extended rosat-eso flux-limited x-ray galaxy cluster survey (reflex ii)-vii. the mass function of galaxy clusters. *Astronomy & Astrophysics*, 608:A65, 2017.
- [10] Hans Böhringer and Norbert Werner. X-ray spectroscopy of galaxy clusters: studying astrophysical processes in the largest celestial laboratories. *The Astronomy and Astrophysics Review*, 18:127–196, 2010.
- [11] Marcus Brüggen, Evan Scannapieco, and Sebastian Heinz. Evolution of x-ray cavities. *Monthly Notices of the Royal Astronomical Society*, 395(4):2210–2220, 2009.
- [12] CL Carilli, DE Harris, L Pentericci, HJA Röttgering, GK Miley, JD Kurk, and Wil van Breugel. The x-ray-radio alignment in the  $z=2.2$  radio galaxy pks 1138–262. *The Astrophysical Journal*, 567(2):781, 2002.
- [13] Kenneth W. Cavagnolo. Accept - archive of chandra cluster entropy profiles - m87, 2009.
- [14] Yi-Hao Chen, Sebastian Heinz, and Torsten A Enßlin. Jets, bubbles, and heat pumps in galaxy clusters. *Monthly Notices of the Royal Astronomical Society*, 489(2):1939–1949, 2019.
- [15] Baolian Cheng, Bowen Jing, Paul Andrew Bradley, Joshua Paul Sauppe, and Rebecca R Roycroft. Evolution of highly multimodal rayleigh–taylor instabilities. *High Energy Density Physics*, 52:101131, 2024.
- [16] Aline Chu, Florence Durret, and Isabel Márquez. Physical properties of brightest cluster galaxies up to redshift 1.80 based on hst data. *Astronomy & Astrophysics*, 649:A42, 2021.
- [17] Renato Colle, S Simonucci, et al. Deep level spectroscopy and auger spectra. In *Encyclopedia of Condensed Matter Physics Volume One*,, pages 369–378. ELSEVIER, Academic Press, 2005.
- [18] Barbara Comis, Marco De Petris, Andrea Conte, Luca Lamagna, and Simone De Gregori. X-ray calibration of sunyaev–zel’dovich scaling relations with the accept catalogue of galaxy clusters observed by chandra. *Monthly Notices of the Royal Astronomical Society*, 418(2):1089–1101, 2011.

- [19] John E Davis. The formal underpinnings of the response functions used in x-ray spectral analysis. *The Astrophysical Journal*, 548(2):1010, 2001.
- [20] Miguel A de Avillez, Gervásio J Anela, and Dieter Breitschwerdt. Variability of the adiabatic parameter in monoatomic thermal and non-thermal plasmas. *Astronomy & Astrophysics*, 616:A58, 2018.
- [21] Sabrina De Grandi, Stefano Ettori, Marcella Longhetti, and Silvano Molendi. On the iron content in rich nearby clusters of galaxies. *Astronomy & Astrophysics*, 419(1):7–18, 2004.
- [22] Sabrina De Grandi and Silvano Molendi. Metallicity gradients in x-ray clusters of galaxies. *The Astrophysical Journal*, 551(1):153, 2001.
- [23] Steven Diehl, Hui Li, Christopher L Fryer, and David Rafferty. Constraining the nature of x-ray cavities in clusters and galaxies. *The Astrophysical Journal*, 687(1):173, 2008.
- [24] VI Dokuchaev. Self-similar spherical shock solution with sustained energy injection. *Astronomy & Astrophysics*, 395(3):1023–1029, 2002.
- [25] Xiaodong Duan and Fulai Guo. Metal-rich trailing outflows uplifted by agn bubbles in galaxy clusters. *The Astrophysical Journal*, 861(2):106, 2018.
- [26] A. C. Fabian. Cooling flows in clusters of galaxies, 1994.
- [27] AC Fabian, Jeremy S Sanders, S Ettori, GB Taylor, SW Allen, CS Crawford, K Iwasawa, RM Johnstone, and PM Ogle. Chandra imaging of the complex x-ray core of the perseus cluster. *Monthly Notices of the Royal Astronomical Society*, 318(4):L65–L68, 2000.
- [28] AC Fabian, JS Sanders, GJ Ferland, BR McNamara, C Pinto, and SA Walker. Hidden cooling flows in clusters of galaxies–iii. accretion on to the central black hole. *Monthly Notices of the Royal Astronomical Society*, 524(1):716–730, 2023.
- [29] Bernard L Fanaroff and Julia M Riley. The morphology of extragalactic radio sources of high and low luminosity. *Monthly Notices of the Royal Astronomical Society*, 167(1):31P–36P, 1974.
- [30] Jianchao Feng and Qingwen Wu. Constraint on the black hole spin of m87 from the accretion-jet model. *Monthly Notices of the Royal Astronomical Society*, 470(1):612–616, 2017.

- [31] William Forman, P Nulsen, S Heinz, F Owen, J Eilek, A Vikhlinin, M Markevitch, R Kraft, E Churazov, and C Jones. Reflections of agn outbursts in the gaseous atmosphere of m87. *arXiv preprint astro-ph/0312576*, 2003.
- [32] Adam Foster, Randall Smith, Nancy S Brickhouse, Patrick D Mullen, Renata S Cumbee, Phillip C Stancil, and Xiaohong Cui. Atomdb 3.1-atomic data and new models for x-ray spectroscopy. In *American Astronomical Society Meeting Abstracts # 231*, volume 231, pages 253–03, 2018.
- [33] Fabio Gastaldello, Aurora Simionescu, Francois Mernier, Veronica Biffi, Massimo Gaspari, Kosuke Sato, and Kyoko Matsushita. The metal content of the hot atmospheres of galaxy groups. *Universe*, 7(7):208, 2021.
- [34] M Gendron-Marsolais, RP Kraft, A Bogdan, J Hlavacek-Larrondo, WR Forman, C Jones, Y Su, P Nulsen, SW Randall, and E Roediger. Uplift, feedback, and buoyancy: Radio lobe dynamics in ngc 4472. *The Astrophysical Journal*, 848(1):26, 2017.
- [35] Ian M George and Rehana Yusaf. The ogip format for radial point spread function datasets. 1995.
- [36] Marie-Joëlle Gingras, Alison L Coil, BR McNamara, Serena Perrotta, Fabrizio Brighenti, HR Russell, and S Peng Oh. Complex velocity structure of nebular gas in active galaxies centred in cooling x-ray atmospheres. *arXiv preprint arXiv:2404.02212*, 2024.
- [37] Vitaly Lazarevich Ginzburg and SI Syrovatskii. Cosmic magnetobremssstrahlung (synchrotron radiation). *Annual Review of Astronomy and Astrophysics*, vol. 3, p. 297, 3:297, 1965.
- [38] TA Gomez, T Nagayama, PB Cho, David Parker Kilcrease, Christopher John Fontes, and Mark Christian Zammit. Introduction to spectral line shape theory. *Journal of Physics B: Atomic, Molecular and Optical Physics*, 55(3):034002, 2022.
- [39] Luciano Gottardi and Kenichiro Nagayashi. A review of x-ray microcalorimeters based on superconducting transition edge sensors for astrophysics and particle physics. *Applied Sciences*, 11(9):3793, 2021.
- [40] Daniel Greenberger, Klaus Hentschel, and Friedel Weinert, editors. *Compendium of Quantum Physics: Concepts, Experiments, History and Philosophy*. Springer, 2009.

- [41] James E Gunn and J Richard Gott III. On the infall of matter into clusters of galaxies and some effects on their evolution. *Astrophysical Journal*, vol. 176, p. 1, 176:1, 1972.
- [42] Fulai Guo. The shape of x-ray cavities in galaxy clusters: probing jet properties and viscosity. *The Astrophysical Journal*, 803(1):48, 2015.
- [43] Fulai Guo and S Peng Oh. Feedback heating by cosmic rays in clusters of galaxies. *Monthly Notices of the Royal Astronomical Society*, 384(1):251–266, 2008.
- [44] H Hamacher. The effectiveness of gas purging to reduce contamination under thermal vacuum conditions. *Vacuum*, 35(4-5):189–194, 1985.
- [45] Gretchen LH Harris, Iu V Babyk, William E Harris, and Brian R McNamara. Globular cluster systems and x-ray atmospheres in galaxies. *The Astrophysical Journal*, 887(2):259, 2019.
- [46] George Helou, BF Madore, M Schmitz, MD Bicay, X Wu, and J Bennett. The nasa/ipac extragalactic database. *Databases & On-Line Data in Astronomy*, pages 89–106, 1991.
- [47] MT Hogan, BR McNamara, F Pulido, PEJ Nulsen, HR Russell, AN Vantyghem, AC Edge, and RA Main. Mass distribution in galaxy cluster cores. *The Astrophysical Journal*, 837(1):51, 2017.
- [48] MT Hogan, BR McNamara, FA Pulido, PEJ Nulsen, AN Vantyghem, HR Russell, AC Edge, Iu Babyk, RA Main, and M McDonald. The onset of thermally unstable cooling from the hot atmospheres of giant galaxies in clusters: constraints on feedback models. *The Astrophysical Journal*, 851(1):66, 2017.
- [49] Philip F Hopkins, Paul Torrey, Claude-André Faucher-Giguère, Eliot Quataert, and Norman Murray. Stellar and quasar feedback in concert: effects on agn accretion, obscuration, and outflows. *Monthly Notices of the Royal Astronomical Society*, 458(1):816–831, 2016.
- [50] Murat Hudaverdi, Kunieda Yamashita, and Akihiro Furuzawa. Study of the structure of abell 3571: An xmm-newton view. *Advances in Space Research*, 36(4):643–649, 2005.
- [51] H-Th Janka, K Langanke, Andreas Marek, G Martínez-Pinedo, and B Müller. Theory of core-collapse supernovae. *Physics Reports*, 442(1-6):38–74, 2007.

- [52] Thomas W Jones and DS De Young. Magnetohydrodynamic simulations of relic radio bubbles in clusters. *The Astrophysical Journal*, 624(2):586, 2005.
- [53] Christian R Kaiser, Georgi Pavlovski, Edward CD Pope, and Hans Fangohr. The stability of buoyant bubbles in the atmospheres of galaxy clusters. *Monthly Notices of the Royal Astronomical Society*, 359(2):493–503, 2005.
- [54] Roy Kilgard. Acis back-illuminated ccds, Dec 1997.
- [55] Chiaki Kobayashi, Amanda I Karakas, and Maria Lugaro. The origin of elements from carbon to uranium. *The Astrophysical Journal*, 900(2):179, 2020.
- [56] Anuradha Koratkar and Omer Blaes. The ultraviolet and optical continuum emission in active galactic nuclei: the status of accretion disks. *Publications of the Astronomical Society of the Pacific*, 111(755):1, 1999.
- [57] Daniel Lecoanet, Ian J Parrish, and Eliot Quataert. The dynamics of rayleigh–taylor stable and unstable contact discontinuities with anisotropic thermal conduction. *Monthly Notices of the Royal Astronomical Society*, 423(2):1866–1882, 2012.
- [58] Hui Li, Giovanni Lapenta, John M Finn, Shengtai Li, and Stirling A Colgate. Modeling the large-scale structures of astrophysical jets in the magnetically dominated limit. *The Astrophysical Journal*, 643(1):92, 2006.
- [59] Elliott H Lieb and Horng-Tzer Yau. A rigorous examination of the chandrasekhar theory of stellar collapse. *Astrophysical Journal, Part 1 (ISSN 0004-637X)*, vol. 323, Dec. 1, 1987, p. 140-144., 323:140–144, 1987.
- [60] K Lodders, H Palme, and H-P Gail. 4.4 abundances of the elements in the solar system: 4 the solar system. *Solar system*, pages 712–770, 2009.
- [61] Katharina Lodders. Solar system abundances and condensation temperatures of the elements. *The Astrophysical Journal*, 591(2):1220, 2003.
- [62] Michael Loewenstein. On iron enrichment, star formation, and type ia supernovae in galaxy clusters. *The Astrophysical Journal*, 648(1):230, 2006.
- [63] Maxim Lyutikov. Magnetic draping of merging cores and radio bubbles in clusters of galaxies. *Monthly Notices of the Royal Astronomical Society*, 373(1):73–78, 2006.

- [64] Adam B Mantz, Steven W Allen, R Glenn Morris, Aurora Simionescu, Ondrej Urban, Norbert Werner, and Irina Zhuravleva. The metallicity of the intracluster medium over cosmic time: further evidence for early enrichment. *Monthly Notices of the Royal Astronomical Society*, 472(3):2877–2888, 2017.
- [65] Adam B Mantz, R Glenn Morris, Steven W Allen, Rebecca EA Canning, Lucie Baumont, Bradford Benson, Lindsey E Bleem, Steven R Ehlert, Benjamin Floyd, Ricardo Herbonnet, et al. Cosmological constraints from gas mass fractions of massive, relaxed galaxy clusters. *Monthly Notices of the Royal Astronomical Society*, 510(1):131–145, 2022.
- [66] William G Mathews and Fabrizio Brighenti. Creation of x-ray cavities in galaxy clusters with cosmic rays. *The Astrophysical Journal*, 660(2):1137, 2007.
- [67] Michael McDonald, Massimo Gaspari, BR McNamara, and GR Tremblay. Revisiting the cooling flow problem in galaxies, groups, and clusters of galaxies. *The Astrophysical Journal*, 858(1):45, 2018.
- [68] BR McNamara, F Kazemzadeh, DA Rafferty, L Bîrzan, PEJ Nulsen, CC Kirkpatrick, and MW Wise. An energetic agn outburst powered by a rapidly spinning supermassive black hole or an accreting ultramassive black hole. *The Astrophysical Journal*, 698(1):594, 2009.
- [69] BR McNamara and PEJ Nulsen. Heating hot atmospheres with active galactic nuclei. *Annu. Rev. Astron. Astrophys.*, 45(1):117–175, 2007.
- [70] BR McNamara, M Wise, PEJ Nulsen, LP David, CL Sarazin, M Bautz, M Markevitch, A Vikhlinin, WR Forman, C Jones, et al. Chandra x-ray observations of the hydra a cluster: an interaction between the radio source and the x-ray-emitting gas. *The Astrophysical Journal*, 534(2):L135, 2000.
- [71] Riddhi Mehta. *Magnetohydrodynamics of magnetars' high-energy and radio emissions: A simulation study*. PhD thesis, Purdue University, 2021.
- [72] François Mernier, Jelle de Plaa, Jelle S Kaastra, Y-Y Zhang, Hiroki Akamatsu, Liyi Gu, Peter Kosec, Junjie Mao, Ciro Pinto, Thomas H Reiprich, et al. Radial metal abundance profiles in the intra-cluster medium of cool-core galaxy clusters, groups, and ellipticals. *Astronomy & Astrophysics*, 603:A80, 2017.
- [73] François Mernier, Jelle de Plaa, Norbert Werner, Jelle S Kaastra, Anton JJ Raassen, Liyi Gu, Junjie Mao, Igone Urdampilleta, Nhut Truong, and Aurora Simionescu.

Mass-invariance of the iron enrichment in the hot haloes of massive ellipticals, groups, and clusters of galaxies. *Monthly Notices of the Royal Astronomical Society: Letters*, 478(1):L116–L121, 2018.

- [74] Koji Mori, Hiroshi Tomida, Hiroshi Nakajima, Takashi Okajima, Hirofumi Noda, Hiroyuki Uchida, Hiromasa Suzuki, Shogo Benjamin Kobayashi, Tomokage Yoneyama, Kouichi Hagino, et al. Status of xtend telescope onboard x-ray imaging and spectroscopy mission (xrism). In *Space Telescopes and Instrumentation 2024: Ultraviolet to Gamma Ray*, volume 13093, pages 434–443. SPIE, 2024.
- [75] RF Mushotzky and Michael Loewenstein. Lack of evolution in the iron abundance in clusters of galaxies and implications for the global star formation rate at high redshift. *The Astrophysical Journal*, 481(2):L63, 1997.
- [76] J. D. Myers. X-ray imaging and spectroscopy mission (xrism), Jul 2023.
- [77] J. D. Myers. Nicer data analysis threads - nicer responses (arfs and rmfs), Feb 2024.
- [78] Hiroshi Nakajima, Yoshitomo Maeda, Hiroyuki Uchida, Takaaki Tanaka, Hiroshi Tsunemi, Kiyoshi Hayashida, Takeshi G Tsuru, Tadayasu Dotani, Ryo Nagino, Shota Inoue, et al. In-orbit performance of the soft x-ray imaging system aboard hitomi (astro-h). *Publications of the Astronomical Society of Japan*, 70(2):21, 2018.
- [79] Masanori Nakamura, Hui Li, and Shengtai Li. Structure of magnetic tower jets in stratified atmospheres. *The Astrophysical Journal*, 652(2):1059, 2006.
- [80] Rodrigo S Nemmen and Alexander Tchekhovskoy. On the efficiency of jet production in radio galaxies. *Monthly Notices of the Royal Astronomical Society*, 449(1):316–327, 2015.
- [81] John Nousek. Science instrument (si) operations handbook for the axaf ccd imaging spectrometer (acis), Nov 1997.
- [82] Paul EJ Nulsen, BR McNamara, Michael W Wise, and LP David. The cluster-scale agn outburst in hydra a. *The Astrophysical Journal*, 628(2):629, 2005.
- [83] FN Owen and JA Eilek. The complex core of abell 2199: The x-ray and radio interaction. *The Astrophysical Journal*, 493(1):73, 1998.
- [84] EK Panagoulia, AC Fabian, and JS Sanders. Searching for the missing iron mass in the core of the centaurus cluster. *Monthly Notices of the Royal Astronomical Society*, 433(4):3290–3296, 2013.

- [85] Electra K Panagoulia, Jeremy S Sanders, and Andy C Fabian. A volume-limited sample of x-ray galaxy groups and clusters–iii. central abundance drops. *Monthly Notices of the Royal Astronomical Society*, 447(1):417–436, 2015.
- [86] William Parrish. Escape peaks in x-ray diffractometry. *Advances in X-Ray Analysis*, 8:118–133, 1964.
- [87] Fabio Pizzolato and Noam Soker. On the rayleigh–taylor instability of radio bubbles in galaxy clusters. *Monthly Notices of the Royal Astronomical Society*, 371(4):1835–1848, 2006.
- [88] Deovrat Prasad, Prateek Sharma, and Arif Babul. Cool-core clusters: The role of bcg, star formation, and agn-driven turbulence. *The Astrophysical Journal*, 863(1):62, 2018.
- [89] Faerlin Pulido. On the origin of cold molecular gas in giant elliptical galaxies. Master’s thesis, University of Waterloo, 2017.
- [90] David A Rafferty, BR McNamara, PEJ Nulsen, and MW Wise. The feedback-regulated growth of black holes and bulges through gas accretion and starbursts in cluster central dominant galaxies. *The Astrophysical Journal*, 652(1):216, 2006.
- [91] Christopher S Reynolds, Barry McKernan, Andrew C Fabian, James M Stone, and John C Vernaleo. Buoyant radio lobes in a viscous intracluster medium. *Monthly Notices of the Royal Astronomical Society*, 357(1):242–250, 2005.
- [92] Mariachiara Rossetti and Silvano Molendi. Cool core remnants in galaxy clusters. *Astronomy & Astrophysics*, 510:A83, 2010.
- [93] Ashley J Ruiter. Type ia supernova sub-classes and progenitor origin. *Proceedings of the International Astronomical Union*, 15(S357):1–15, 2019.
- [94] Mateusz Ruszkowski, TA Enßlin, M Brüggen, S Heinz, and C Pfrommer. Impact of tangled magnetic fields on fossil radio bubbles. *Monthly Notices of the Royal Astronomical Society*, 378(2):662–672, 2007.
- [95] George B Rybicki and Alan P Lightman. *Radiative processes in astrophysics*. John Wiley & Sons, 1991.
- [96] Joana S Santos, Paolo Tozzi, Piero Rosati, and Hans Böhringer. The evolution of cool-core clusters. *Astronomy & Astrophysics*, 521:A64, 2010.

- [97] Craig L Sarazin. X-ray emission from clusters of galaxies. 1988.
- [98] Ethan J Schreier, PAUL Gorenstein, and ERIC D Feigelson. High-resolution x-ray observations of m87-nucleus, jet and radio halo. *Astrophysical Journal, Part 1, vol. 261, Oct. 1, 1982, p. 42-50.*, 261:42–50., 1982.
- [99] Randall K Smith, Nancy S Brickhouse, Duane A Liedahl, and John C Raymond. Collisional plasma models with apec/aped: emission-line diagnostics of hydrogen-like and helium-like ions. *The Astrophysical Journal*, 556(2):L91, 2001.
- [100] Bradford Snios, Paul EJ Nulsen, Ralph P Kraft, CC Cheung, Eileen T Meyer, William R Forman, Christine Jones, and Stephen S Murray. Detection of superluminal motion in the x-ray jet of m87. *The Astrophysical Journal*, 879(1):8, 2019.
- [101] Assaf Sternberg and Noam Soker. Explaining the energetic agn outburst of ms 0735+7421 with massive slow jets. *Monthly Notices of the Royal Astronomical Society*, 398(1):422–428, 2009.
- [102] Yuanyuan Su, Francoise Combes, Valeria Olivares, Gianluca Castignani, Pablo Torne, and Reinout van Weeren. The composition and thermal properties of a cool core lacking a brightest cluster galaxy. *Monthly Notices of the Royal Astronomical Society*, 526(4):6052–6058, 2023.
- [103] Rosie Y Talbot, Martin A Bourne, and Debora Sijacki. Blandford–znajek jets in galaxy formation simulations: method and implementation. *Monthly Notices of the Royal Astronomical Society*, 504(3):3619–3650, 2021.
- [104] Roland Timmerman, Reinout J van Weeren, Andrea Botteon, HJA Röttgering, BR McNamara, Frits Sweijen, Laura Bîrzan, and Leah K Morabito. Measuring cavity powers of active galactic nuclei in clusters using a hybrid x-ray–radio method—a new window on feedback opened by subarcsecond lofar-vlbi observations. *Astronomy & Astrophysics*, 668:A65, 2022.
- [105] Ondrej Urban, Norbert Werner, SW Allen, Aurora Simionescu, and A Mantz. A uniform metallicity in the outskirts of massive, nearby galaxy clusters. *Monthly Notices of the Royal Astronomical Society*, 470(4):4583–4599, 2017.
- [106] Sylvain Veilleux, Roberto Maiolino, Alberto D Bolatto, and Susanne Aalto. Cool outflows in galaxies and their implications. *The Astronomy and Astrophysics Review*, 28:1–173, 2020.

- [107] T Venturi, S Bardelli, M Zagaria, I Prandoni, and R Morganti. Radio emission from the a3571 cluster complex: The final stage of a cluster merger? *Astronomy & Astrophysics*, 385(1):39–54, 2002.
- [108] Yanghua Wang. The ricker wavelet and the lambert w function. *Geophysical Journal International*, 200(1):111–115, 2015.
- [109] AS Wilson and Y Yang. Chandra x-ray imaging and spectroscopy of the m87 jet and nucleus. *The Astrophysical Journal*, 568(1):133, 2002.
- [110] Michael W Wise, BR McNamara, PEJ Nulsen, JC Houck, and LP David. X-ray supercavities in the hydra a cluster and the outburst history of the central galaxy’s active nucleus. *The Astrophysical Journal*, 659(2):1153, 2007.
- [111] SE Woosley and Robert D Hoffman. The alpha-process and the r-process. *Astrophysical Journal, Part 1 (ISSN 0004-637X)*, vol. 395, no. 1, p. 202-239., 395:202–239, 1992.
- [112] Team XRISM. The xrism proposers’ observatory guide - heasarc, Feb 2024.
- [113] Robert M Yates, Guinevere Kauffmann, and Qi Guo. The relation between metallicity, stellar mass and star formation in galaxies: an analysis of observational and model data. *Monthly Notices of the Royal Astronomical Society*, 422(1):215–231, 2012.
- [114] Feng Yuan, Zhaoming Gan, Ramesh Narayan, Aleksander Sadowski, Defu Bu, and Xue-Ning Bai. Numerical simulation of hot accretion flows. iii. revisiting wind properties using the trajectory approach. *The Astrophysical Journal*, 804(2):101, 2015.
- [115] Feng Yuan and Ramesh Narayan. Hot accretion flows around black holes. *Annual Review of Astronomy and Astrophysics*, 52(1):529–588, 2014.
- [116] Claudio Zanni, Giuseppe Murante, Gianluigi Bodo, Silvano Massaglia, Paola Rossi, and Attilio Ferrari. Heating groups and clusters of galaxies: the role of agn jets. *Astronomy & Astrophysics*, 429(2):399–415, 2005.

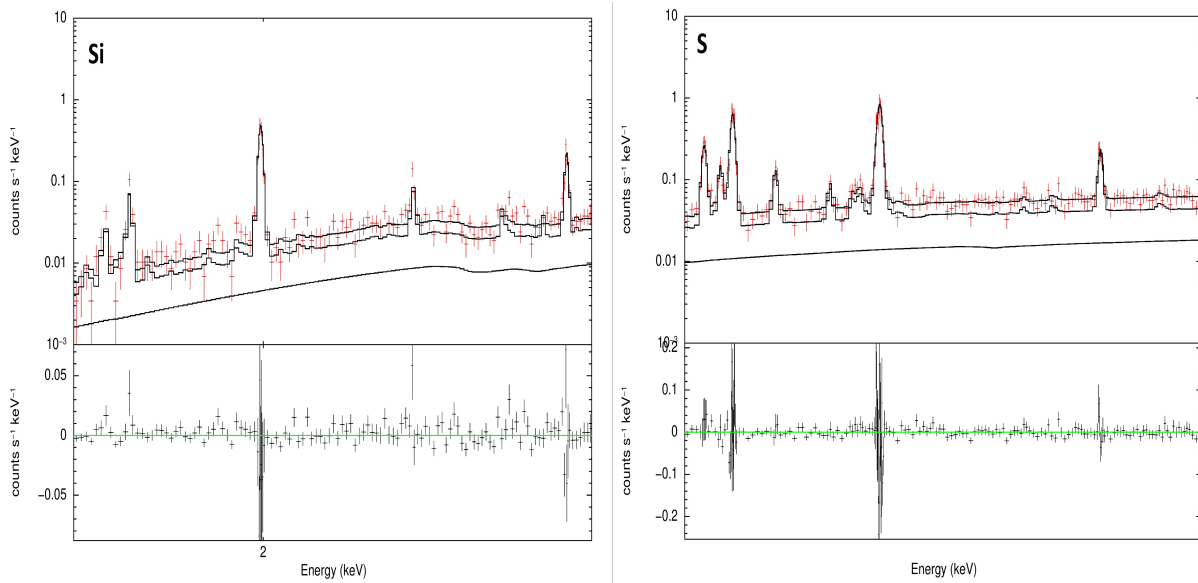
# APPENDICES

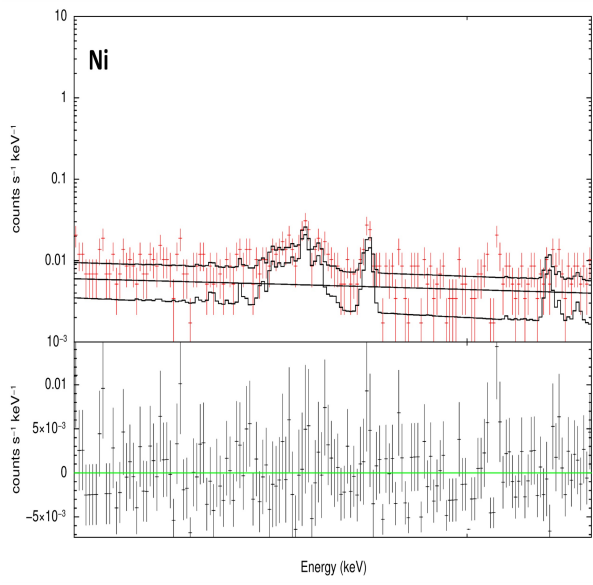
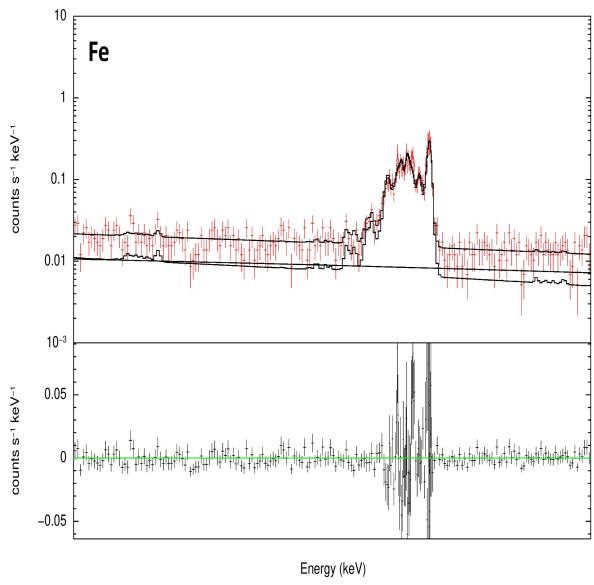
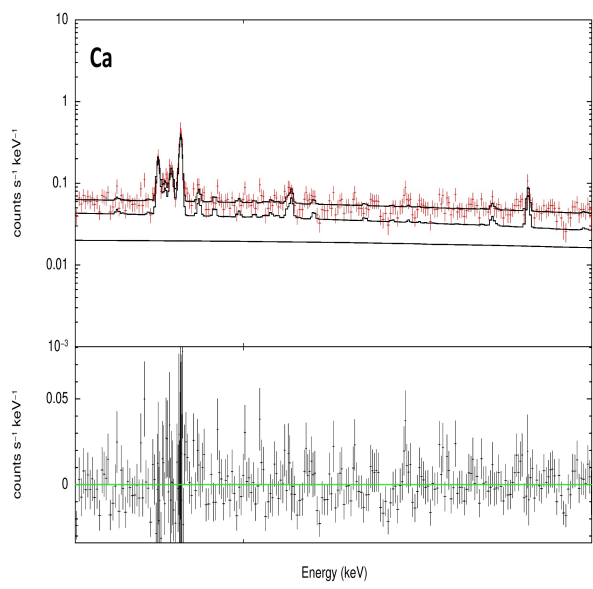
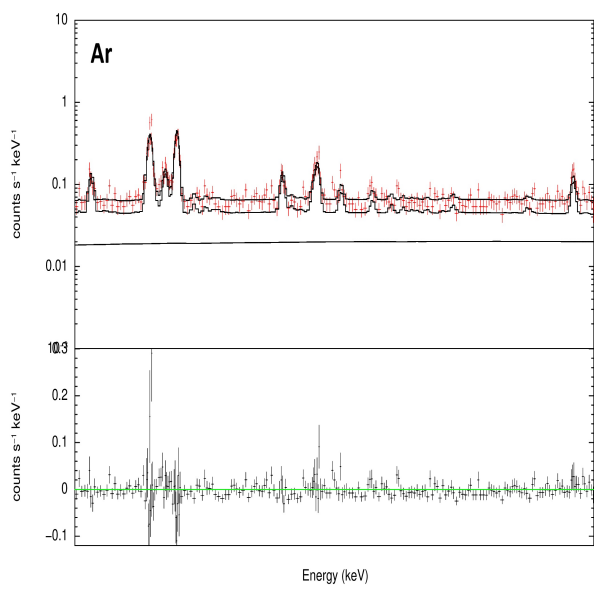
# Appendix A

## Chandra Cluster Datasheets

### A.1 XRISM Narrowbands

Narrowband spectra used in M87 observations. The selected images are from the central pointing, using a TBabs\*(bapec+powerlaw) model. The residuals between the model and data are shown in the bottom graph.



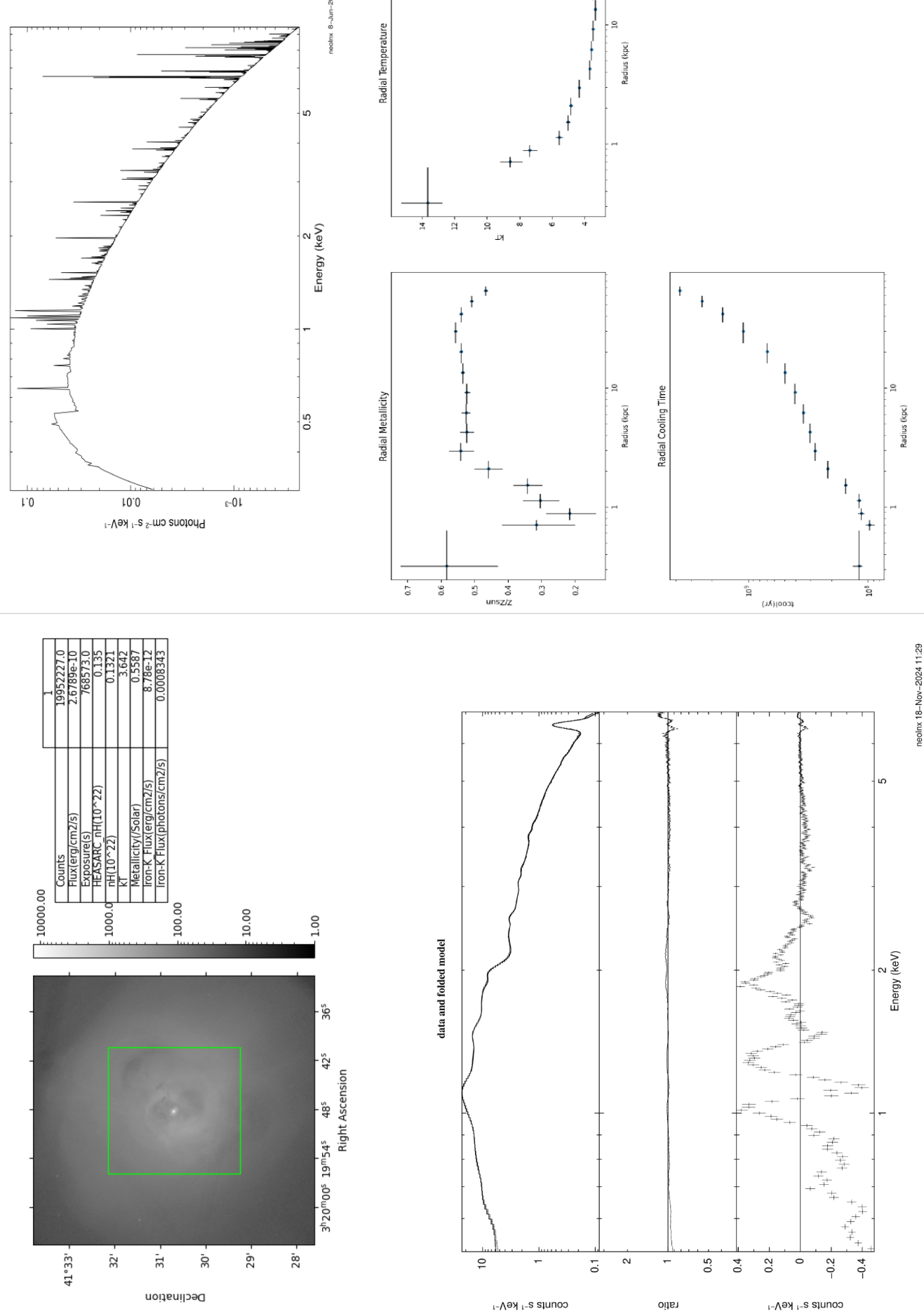


## A.2 The Datasheets

The datasheets are produced by extracting a spectrum from a Chandra image. The datasheets consist of an image of the cluster, centered on the core of the cluster, with a green box showing the 2.9 x 2.9 arcmin footprint of XRISM. It contains a table of data extracted from the XRISM sized region, including flux, exposure time, hydrogen column density, temperature, metallicity and the flux produced by the Iron-K complex. Below there is a graph showing the XRISM footprint spectrum with an Xspec model on top of the data, the second and third portions of the graph are the residuals between the model and the data. The second page contains the raw model without data attributed to it and the radial profiles of the cluster. The radial profiles are not produced using the XRISM footprint, rather using concentric annular regions beginning from the center. Each region produces a spectrum and is modelled to obtain metallicity and temperature values. The cooling time graph is produced by using the inner and outer radii of the annulus, the flux and the temperature of the annular region through Eq 2.3 in Chapter 2.

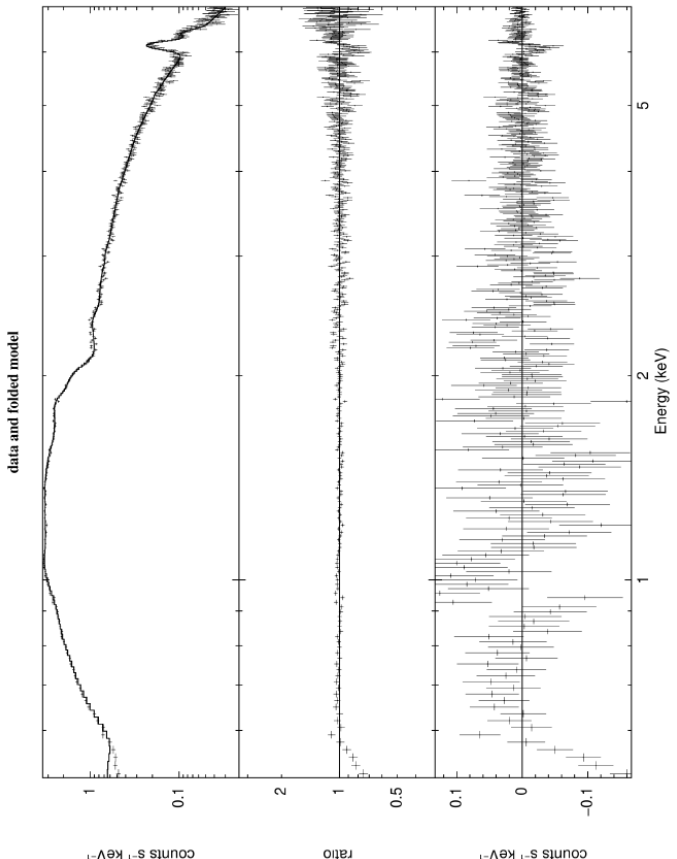
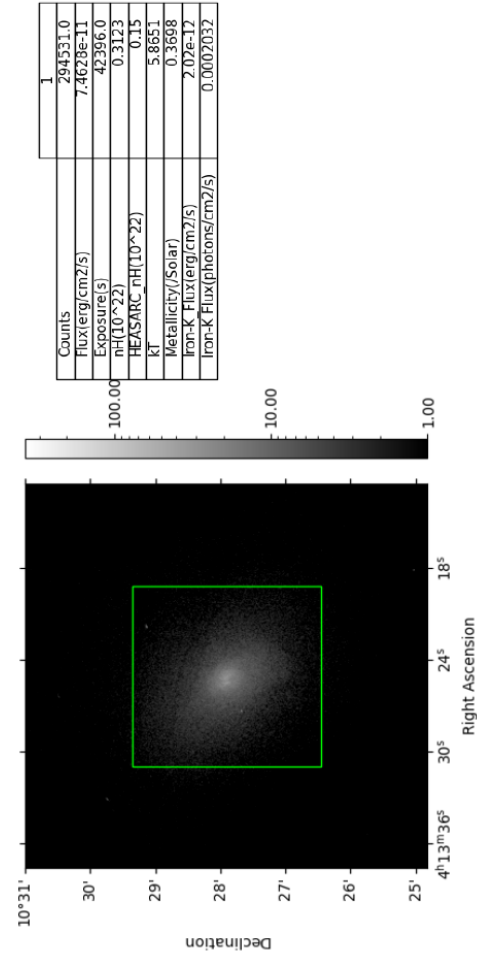
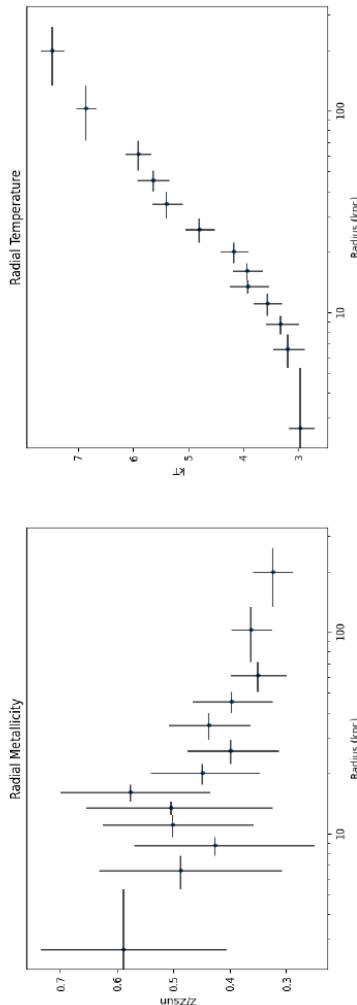
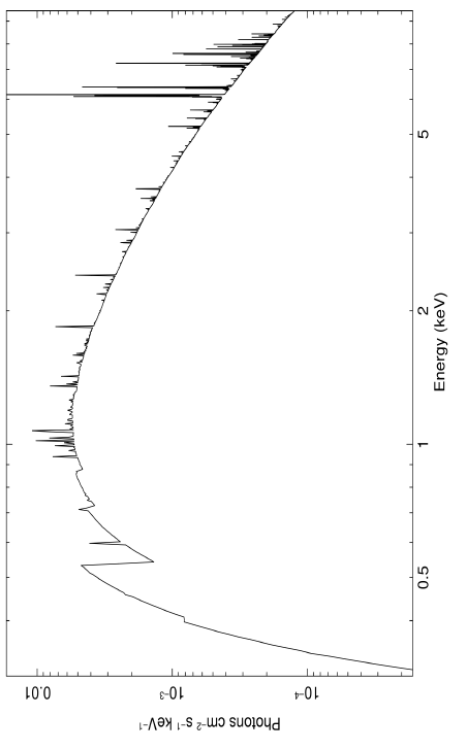


Galaxy Cluster: A426

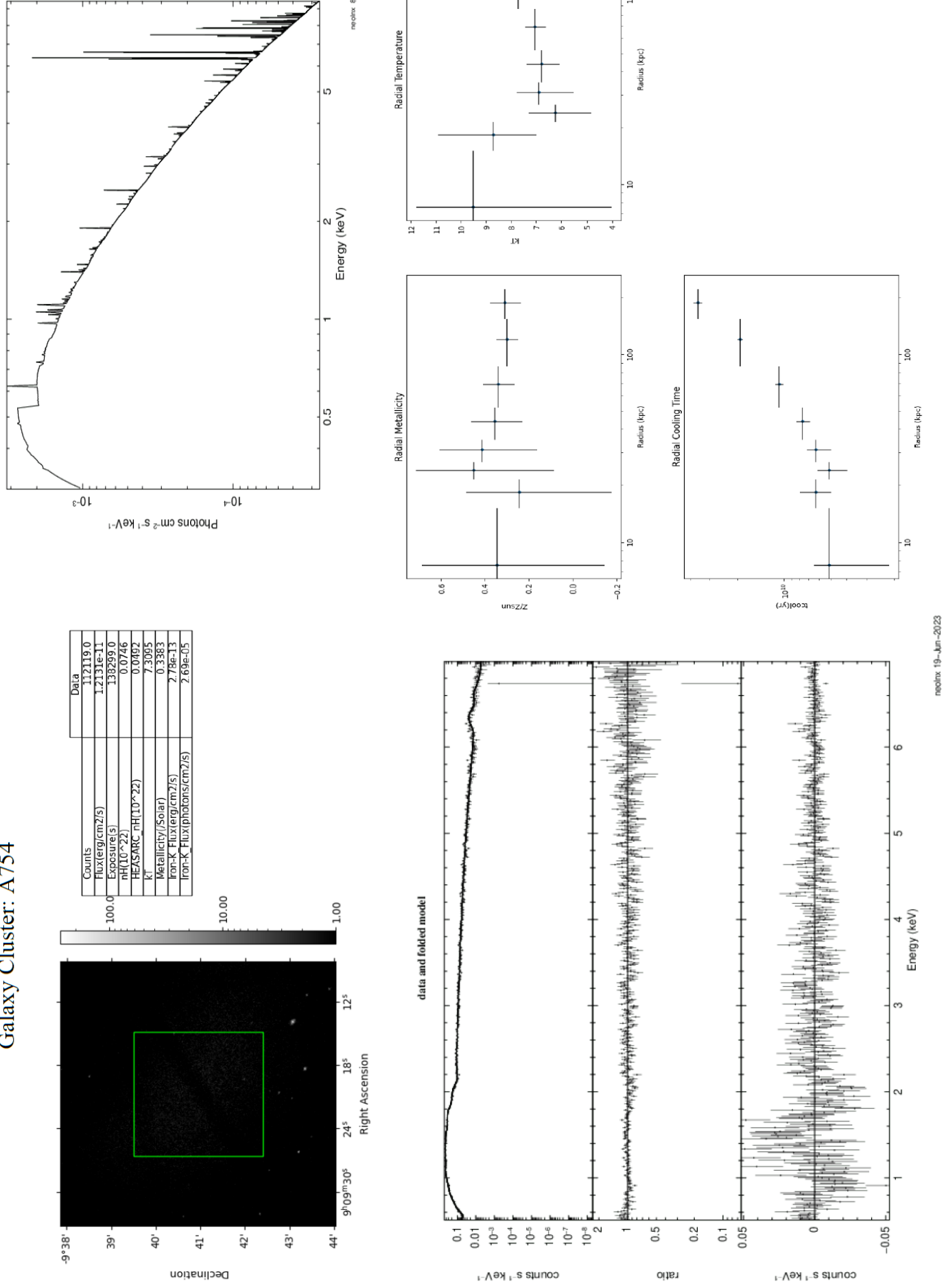


# Galaxy Cluster: A478

Current Theoretical Model

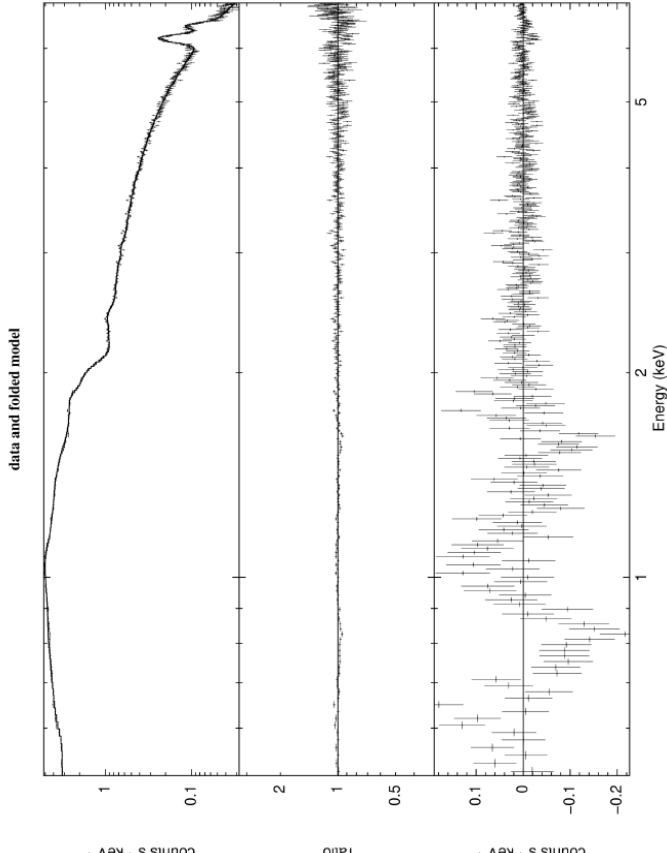
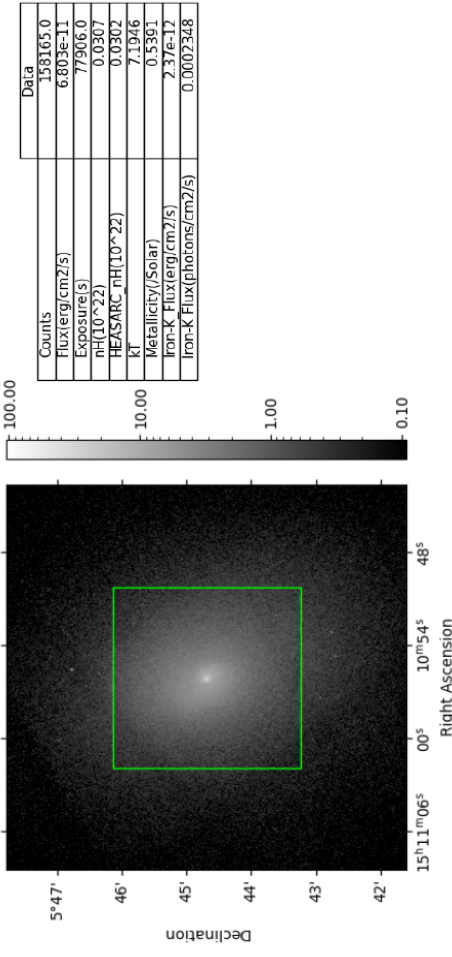
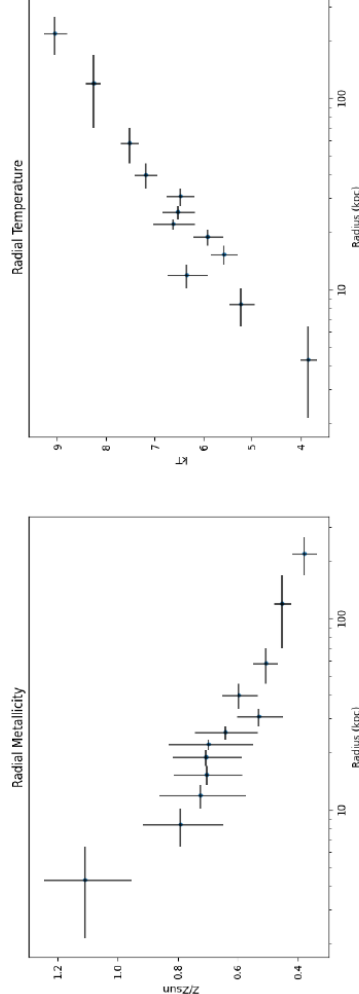
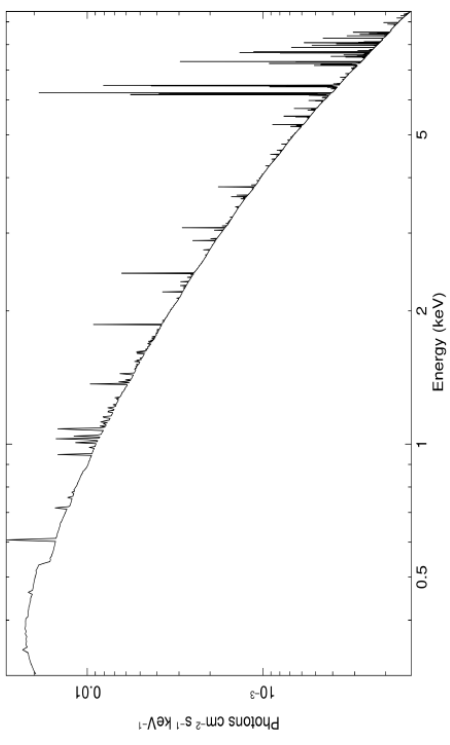


# Galaxy Cluster: A754



# Galaxy Cluster: A2029

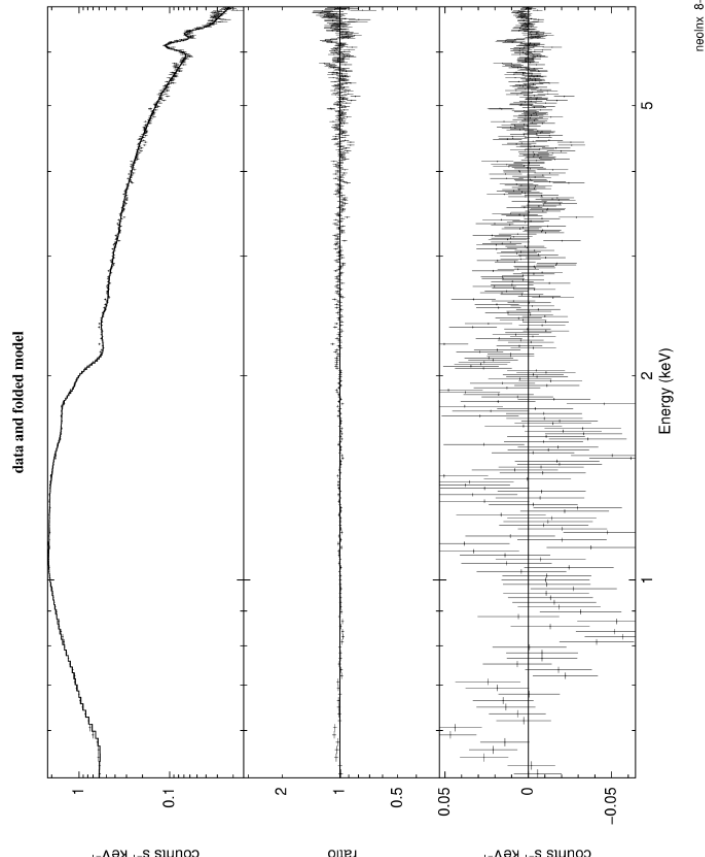
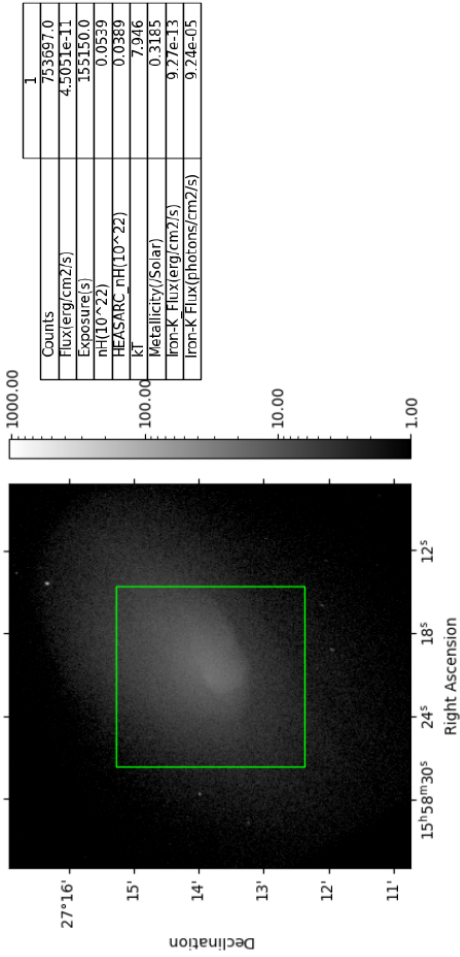
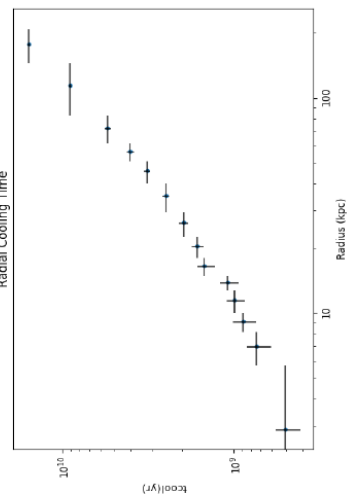
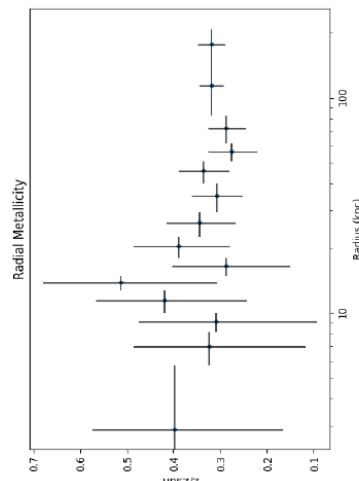
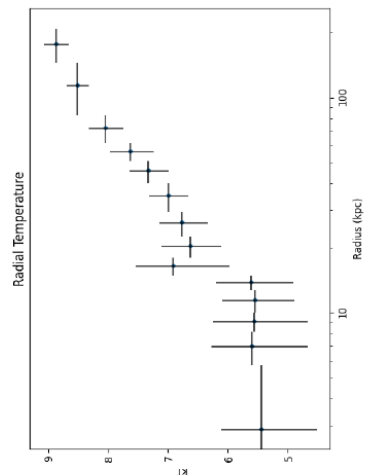
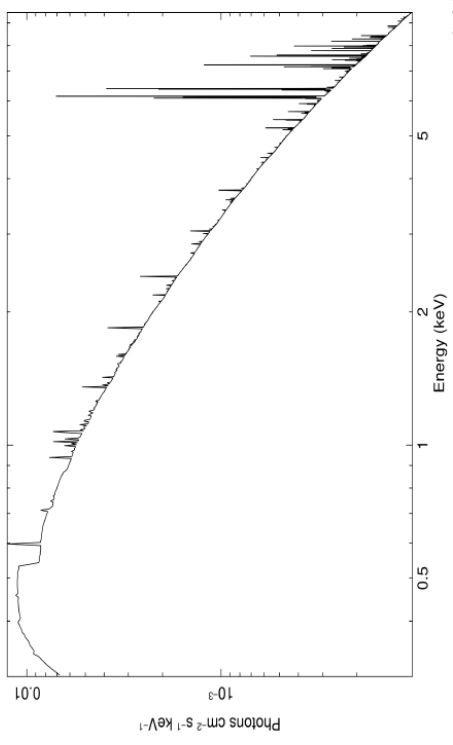
Current Theoretical Model



neulinx 30-May-2023 10:47

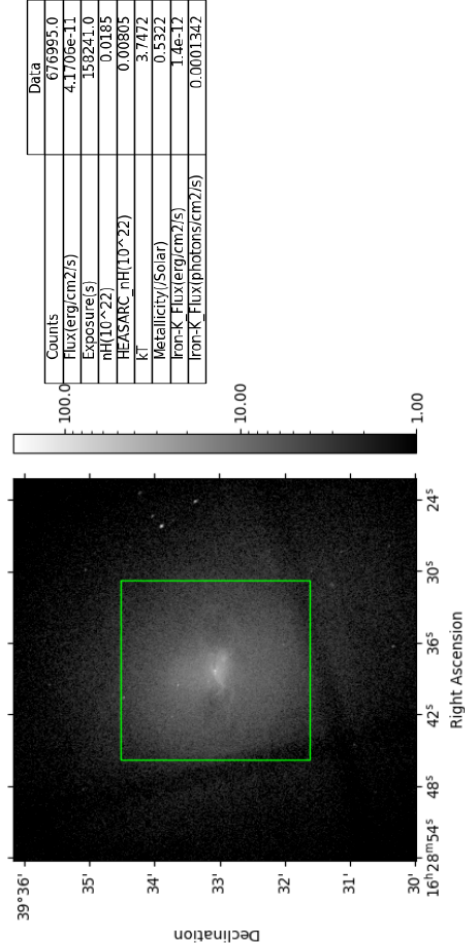
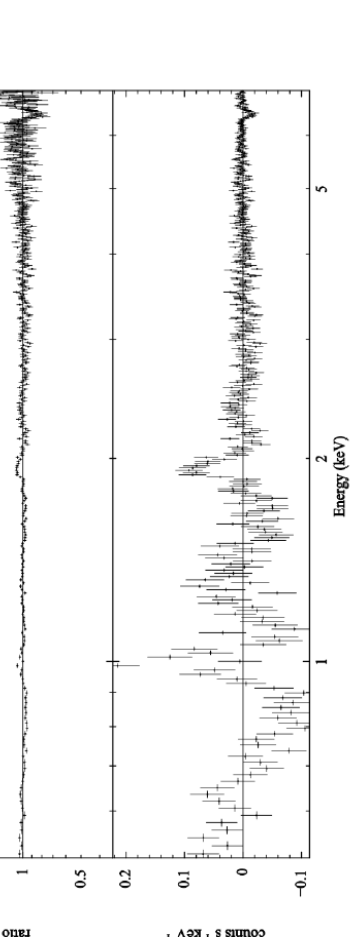
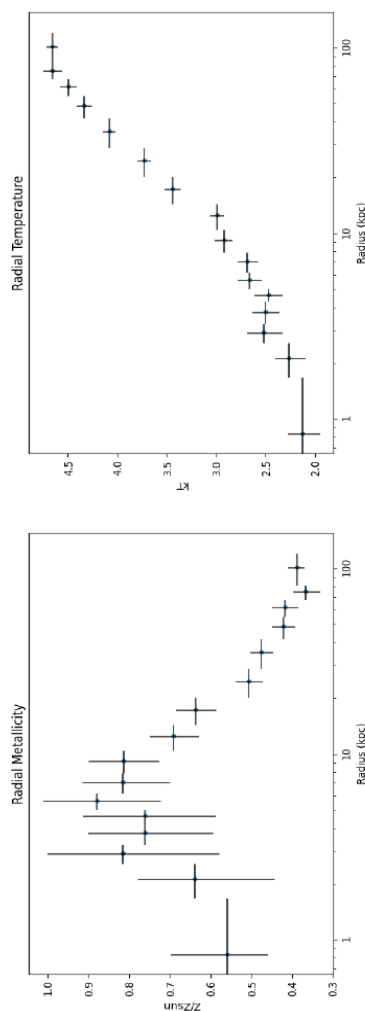
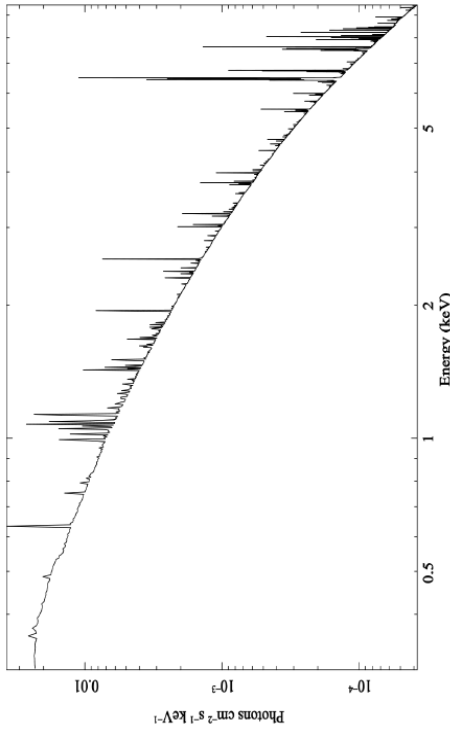
## Galaxy Cluster: A2142

Current Theoretical Model



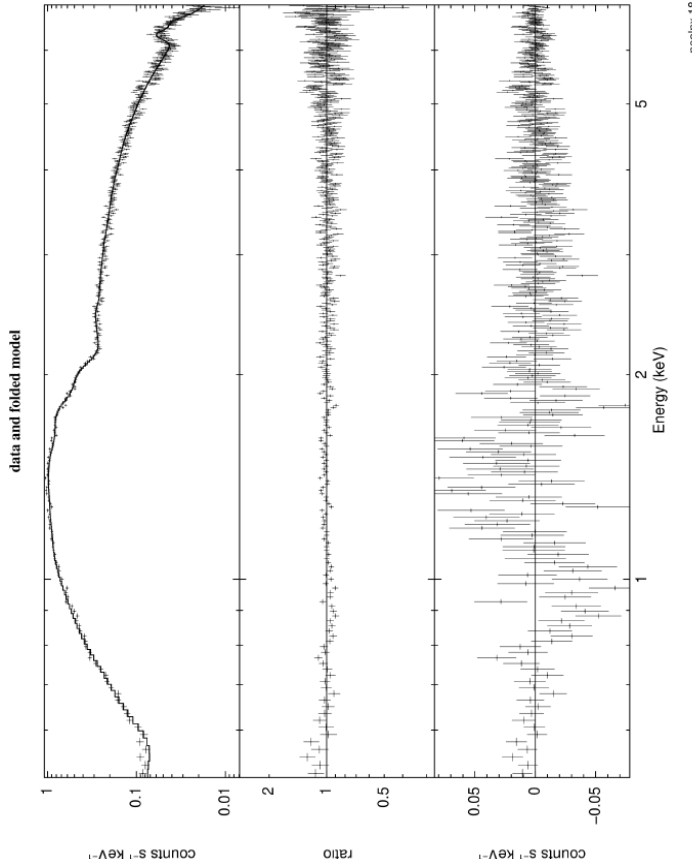
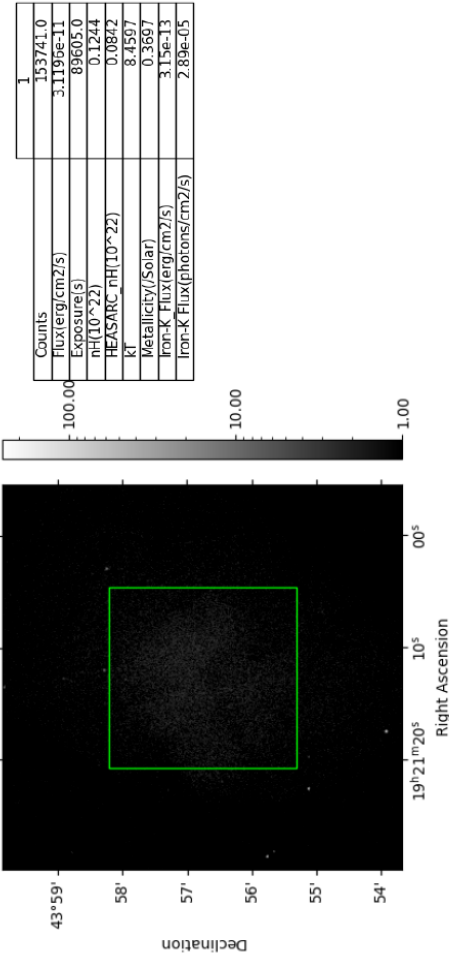
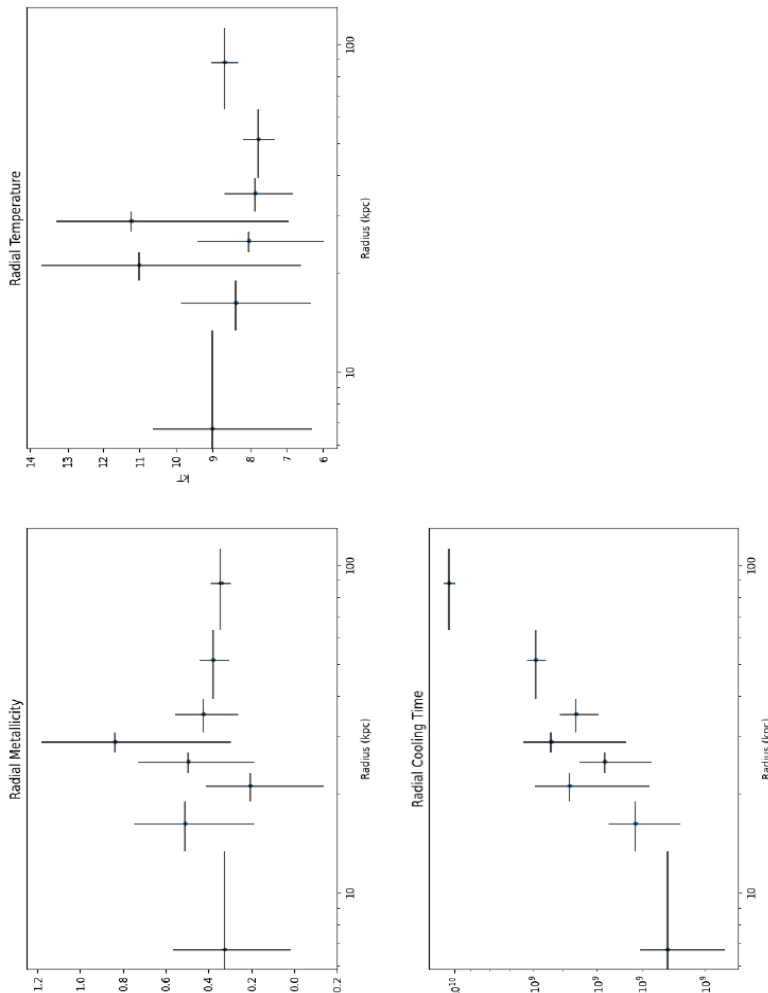
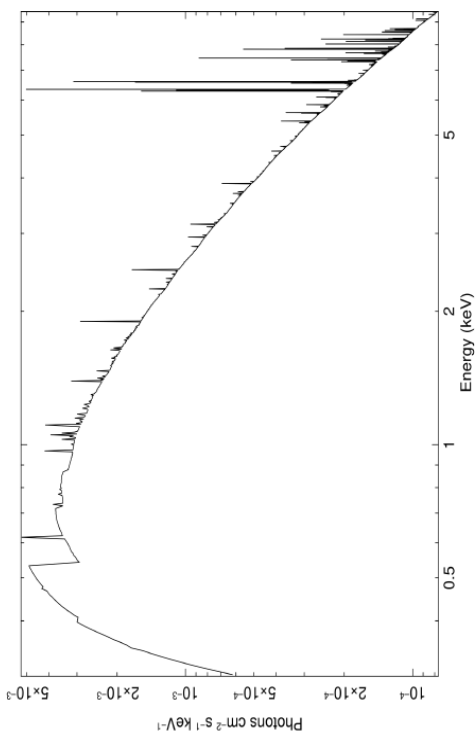
# Galaxy Cluster: A2199

Current Theoretical Model



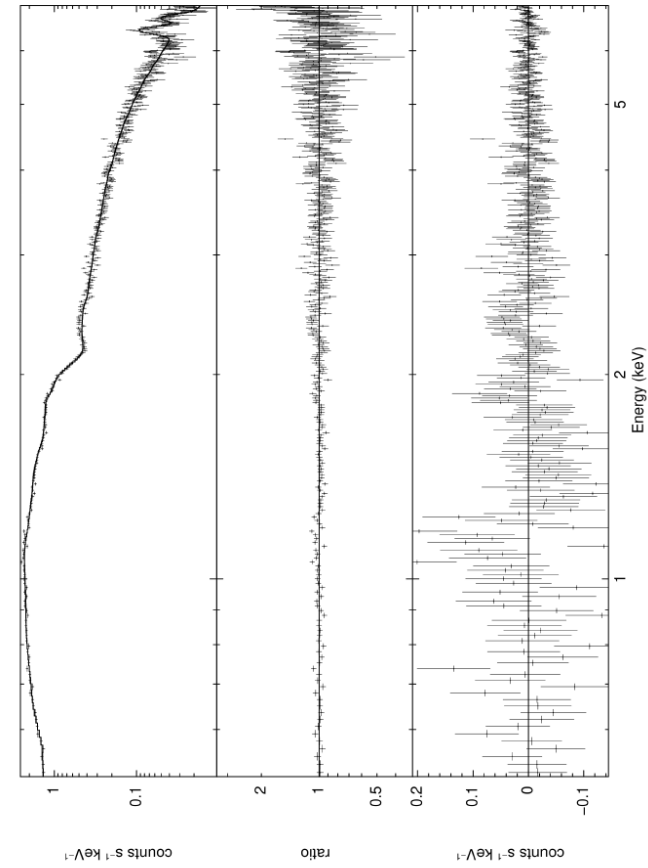
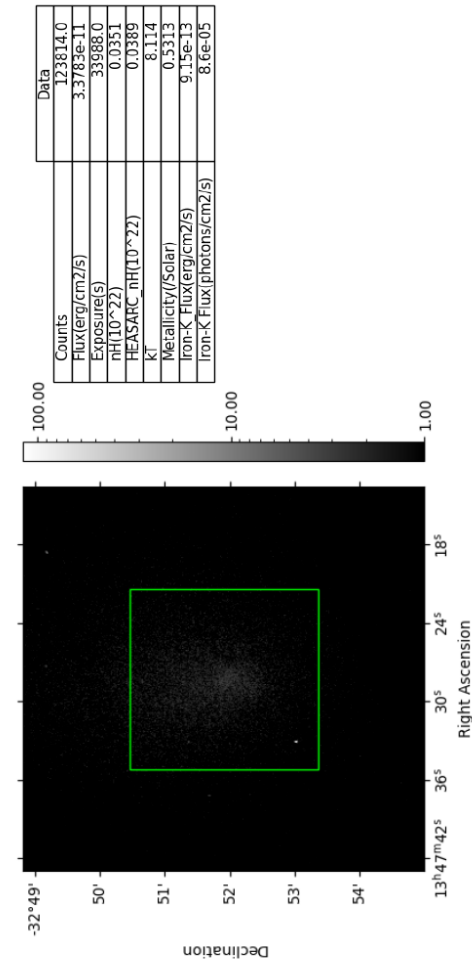
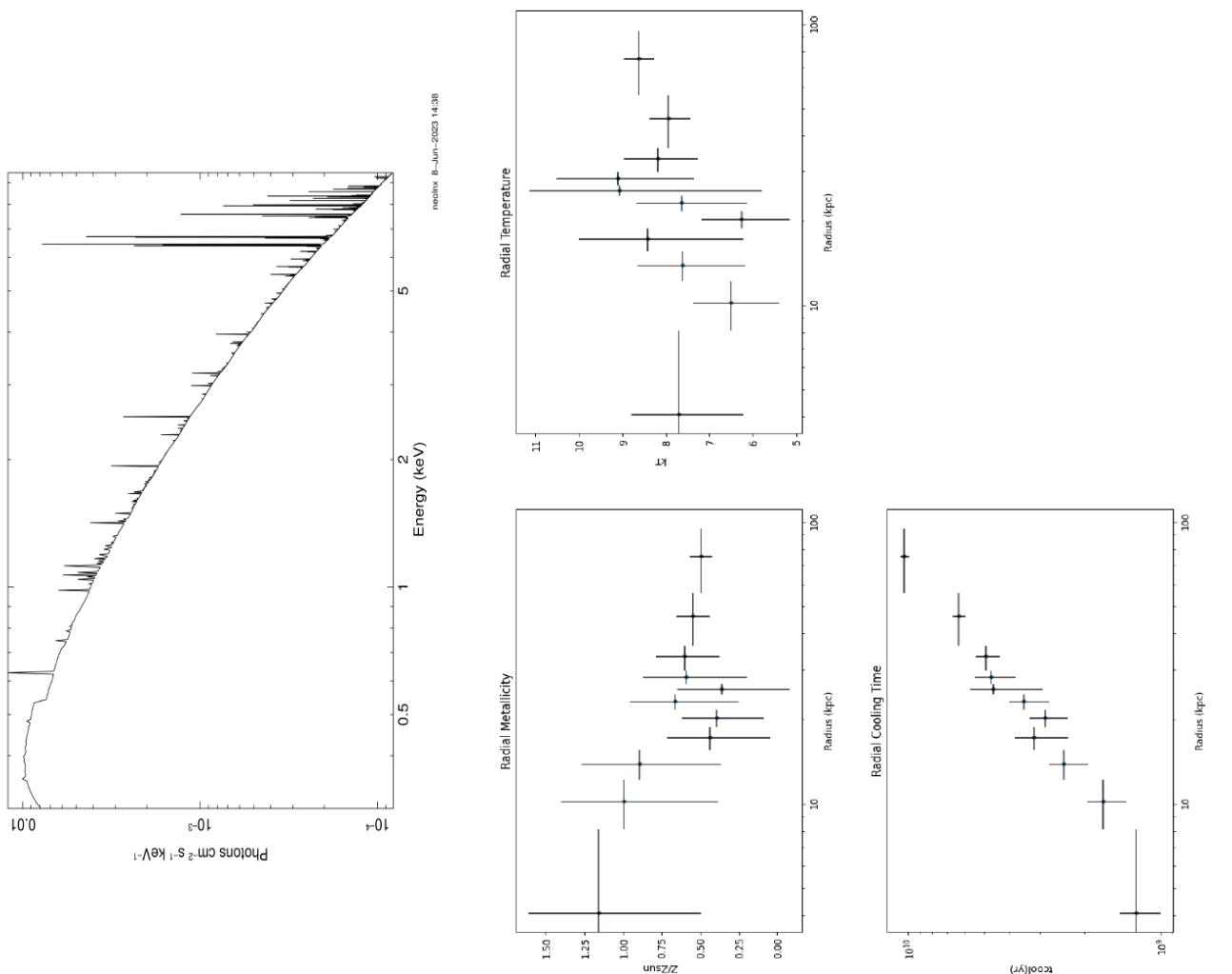
# Galaxy Cluster: A2319

Current Theoretical Model



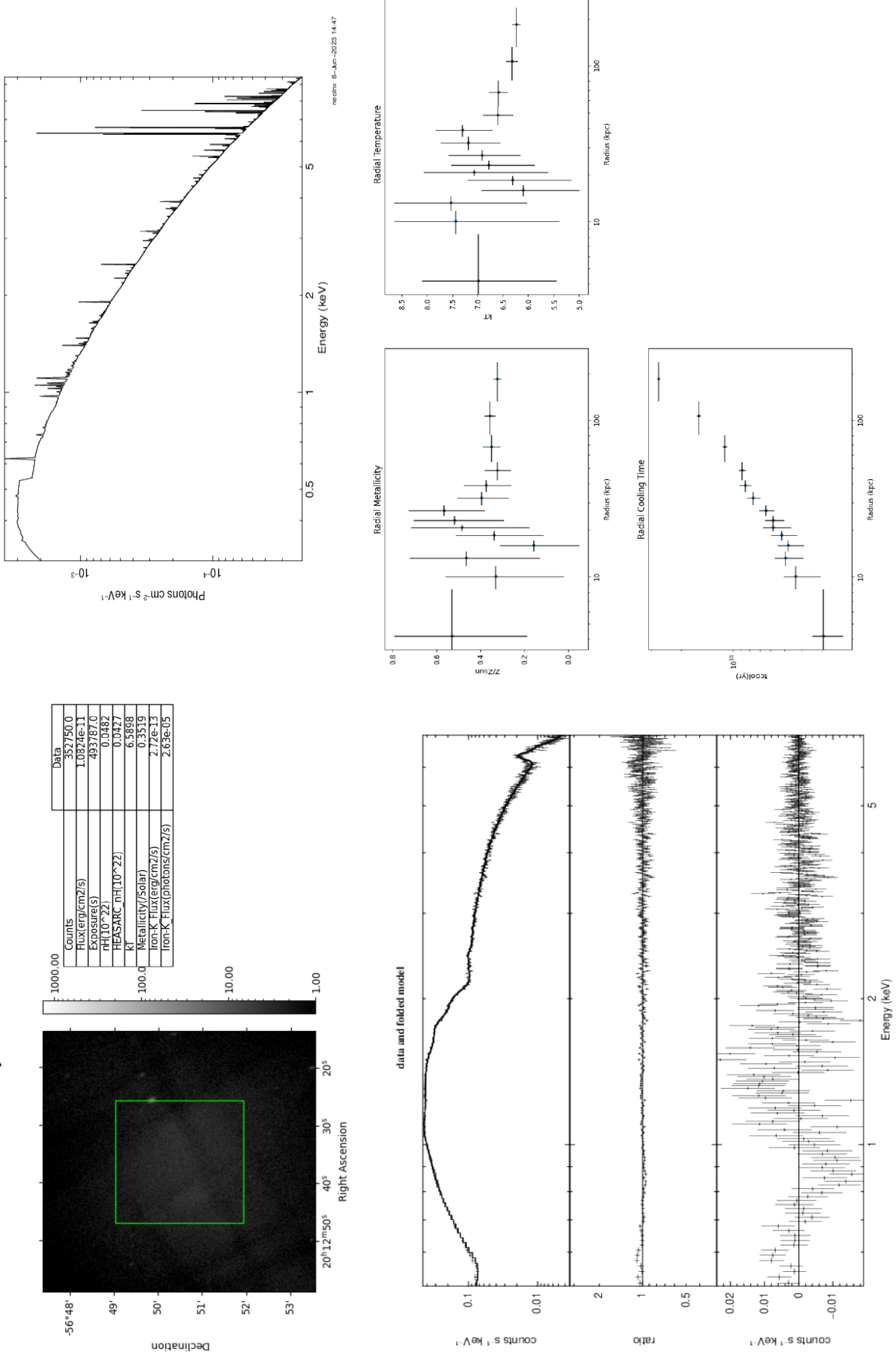
# Galaxy Cluster: A3571

Current Theoretical Model



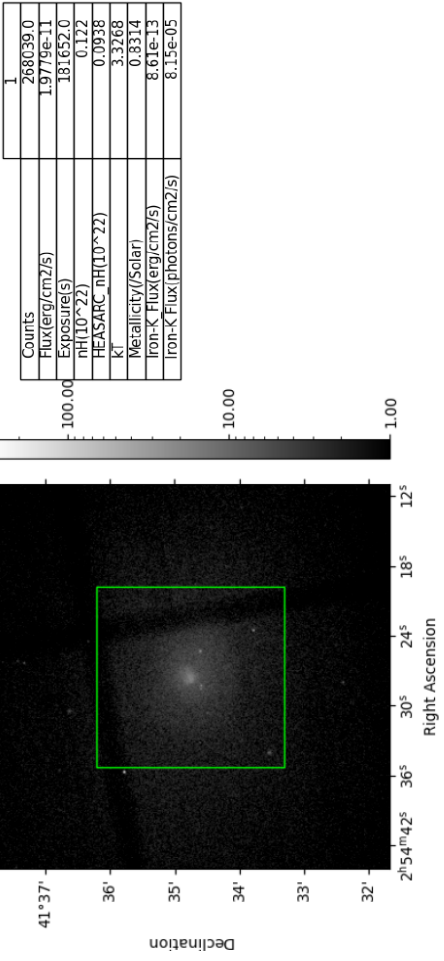
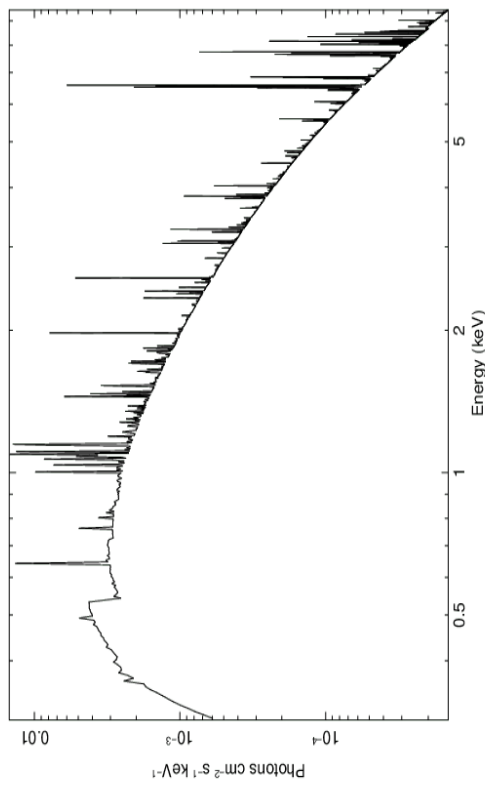
# Galaxy Cluster: A3667

Current Theoretical Model

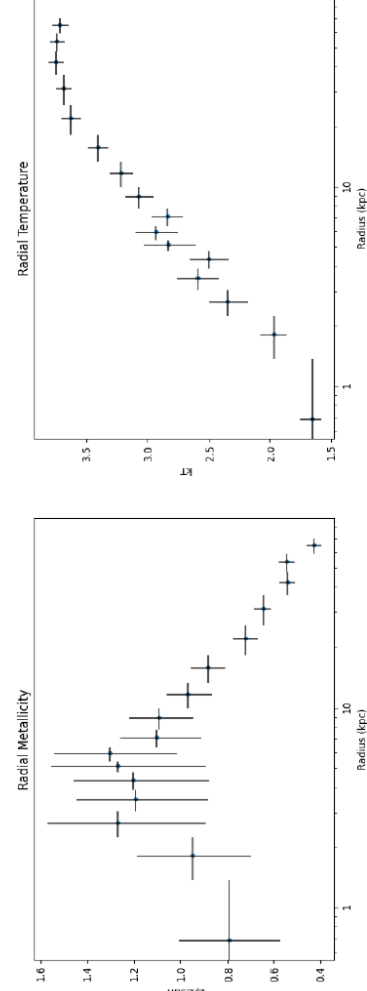
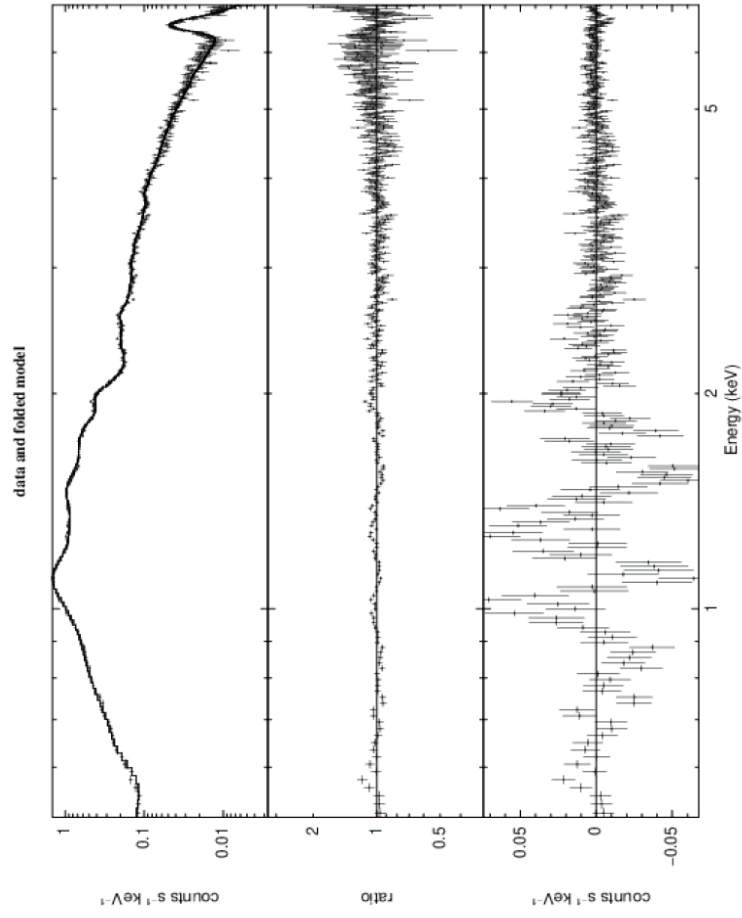


# Galaxy Cluster: AWM7

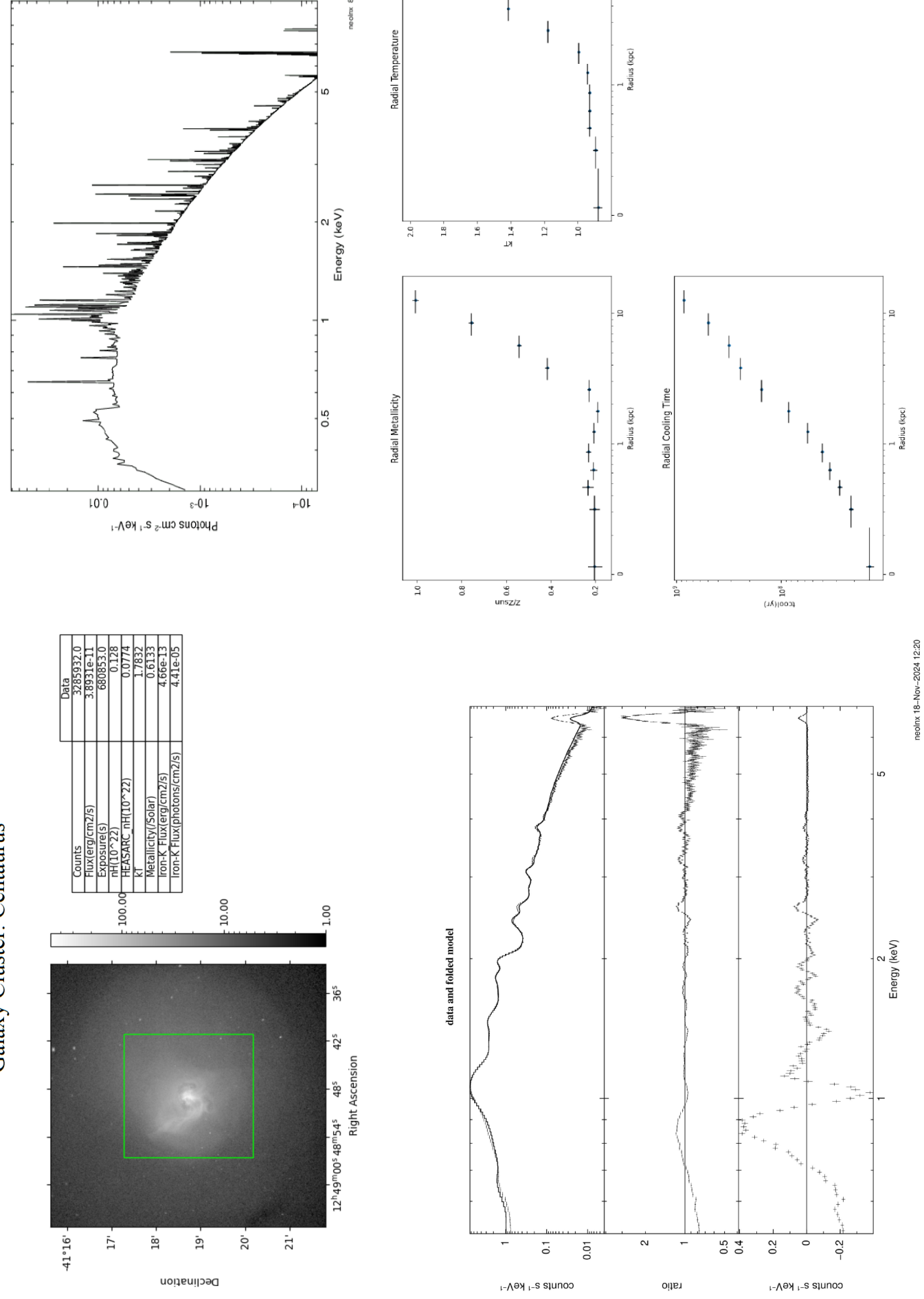
Current Theoretical Model



data and folded model

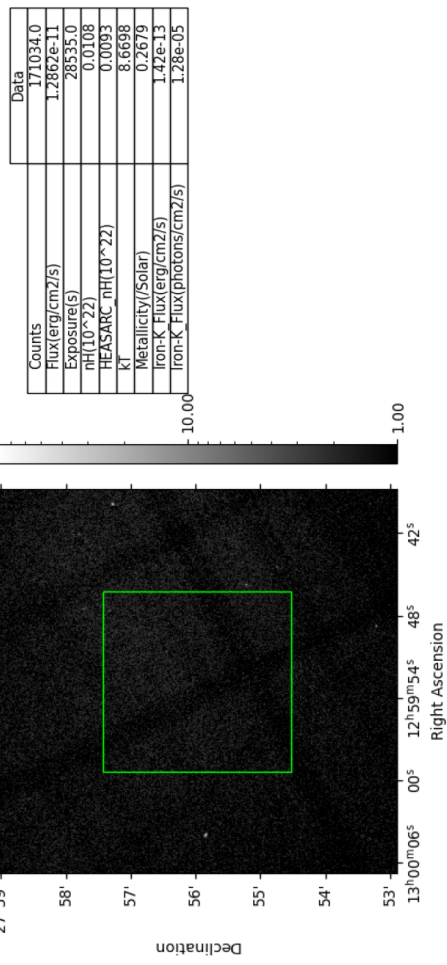
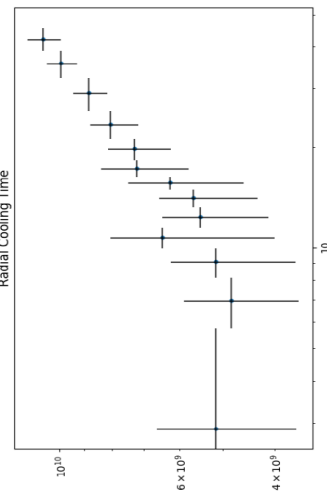
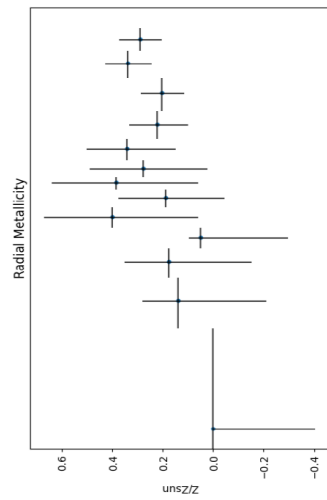
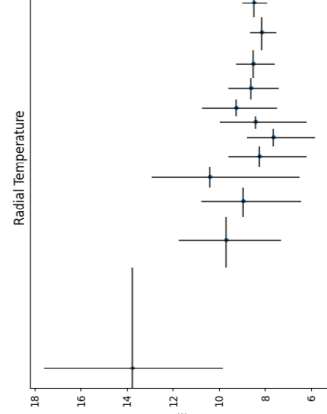
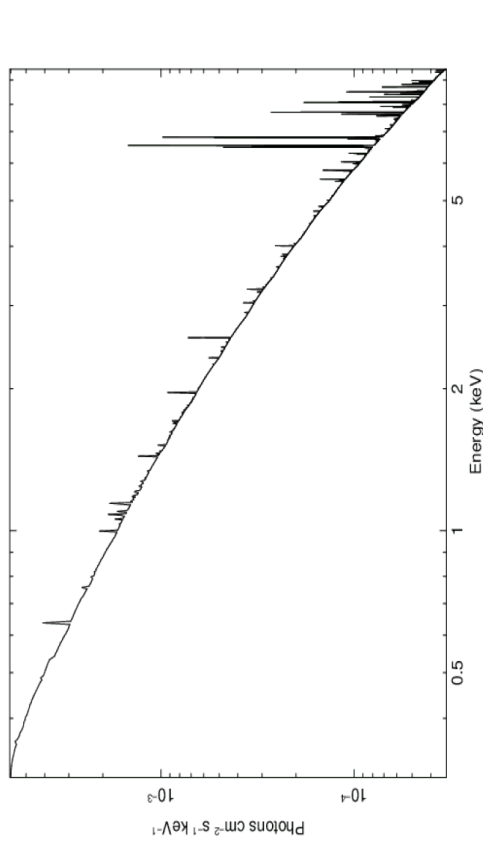


## Galaxy Cluster: Centaurus



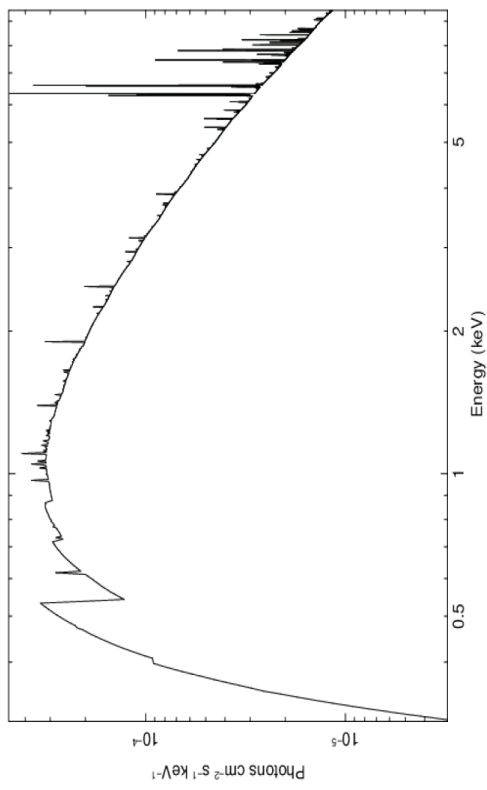
# Galaxy Cluster: Coma

## Current Theoretical Model

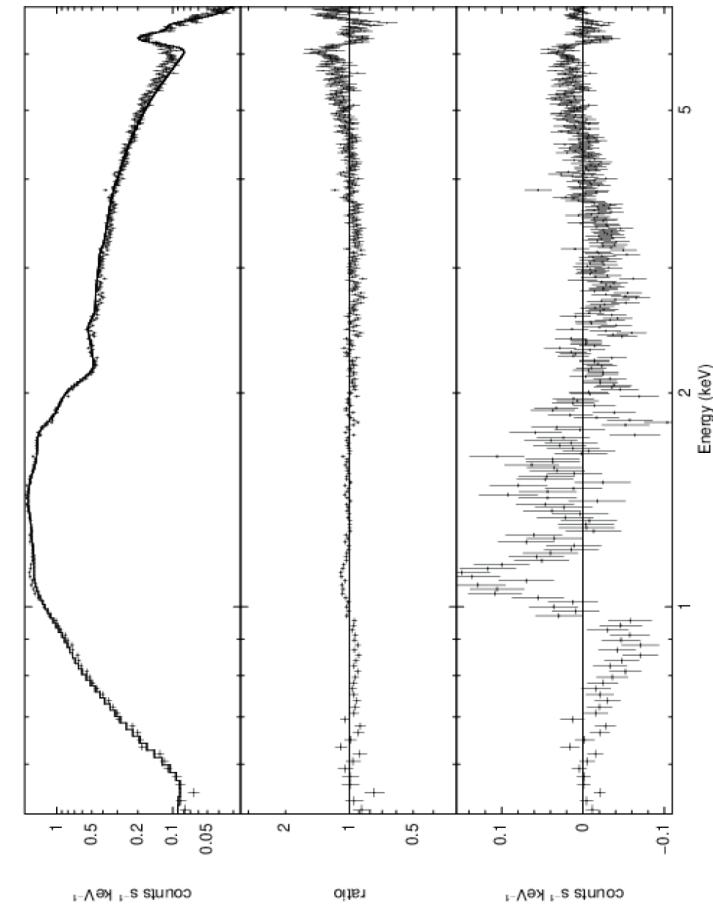


## Galaxy Cluster: CygnusA

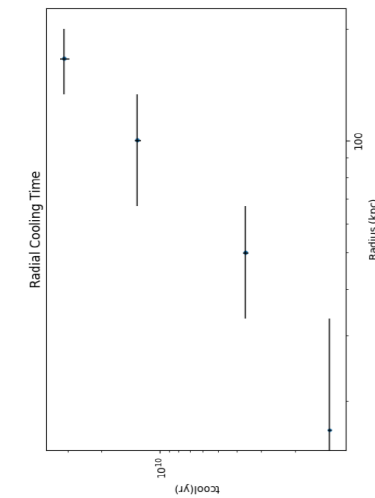
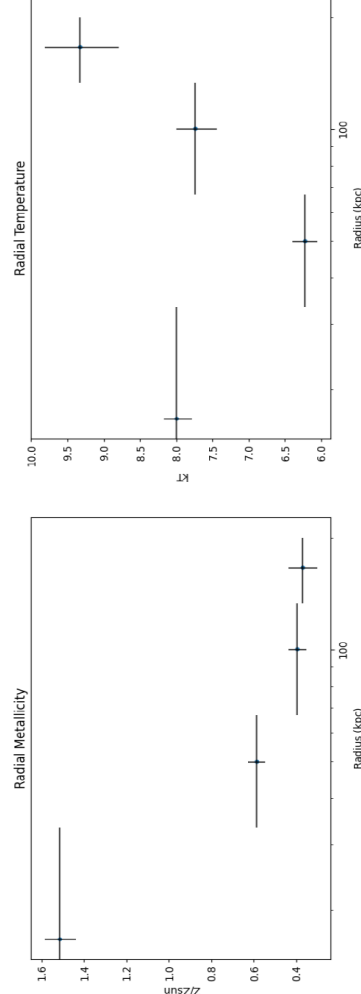
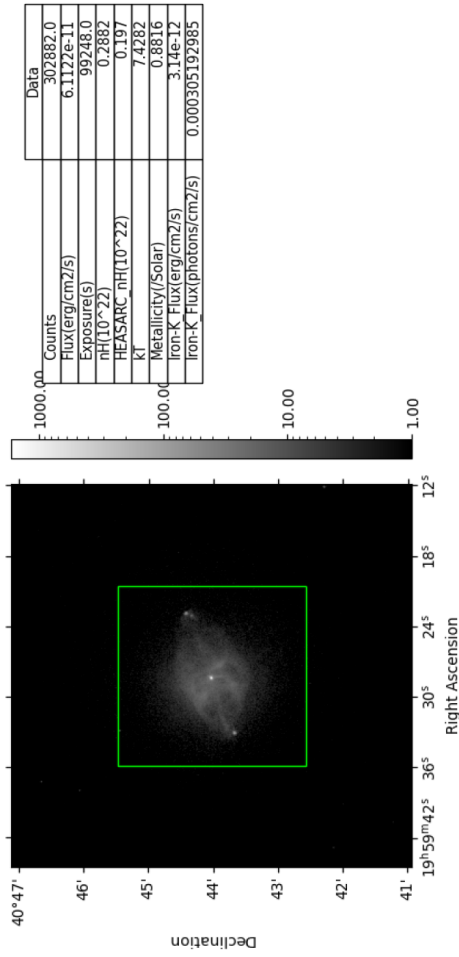
Current Theoretical Model



data and folded model



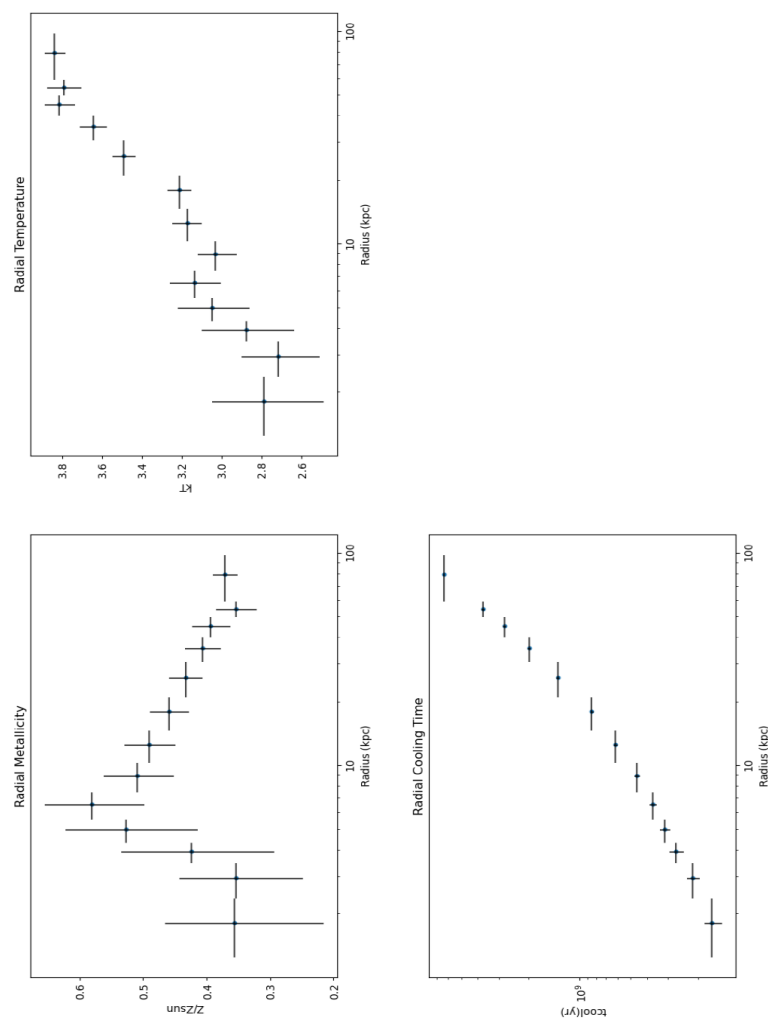
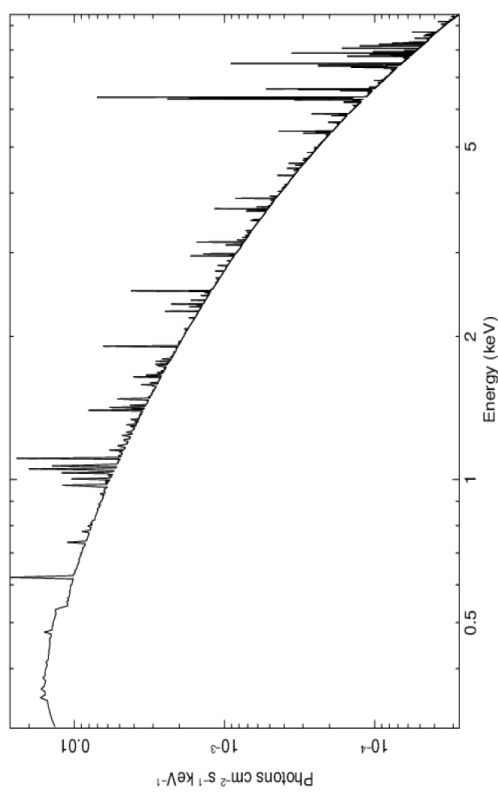
ne01mx 4-Jul-2023 !



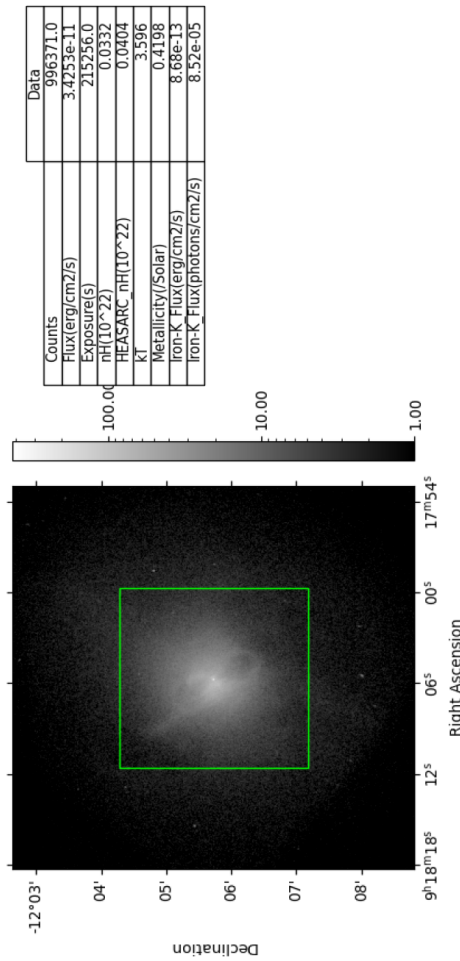
ne01mx 22-Jun-2023 12:40

# Galaxy Cluster: HydraA

Current Theoretical Model

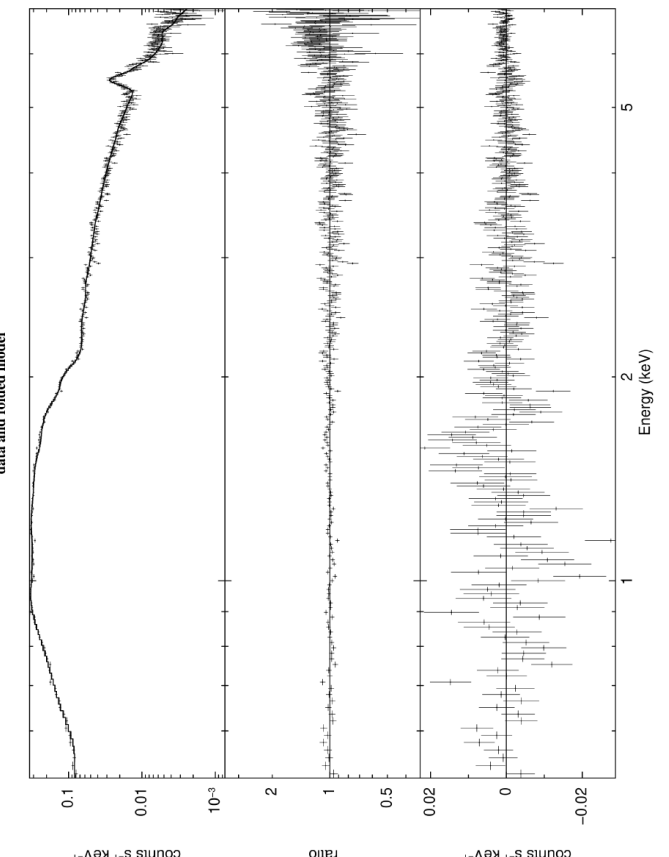
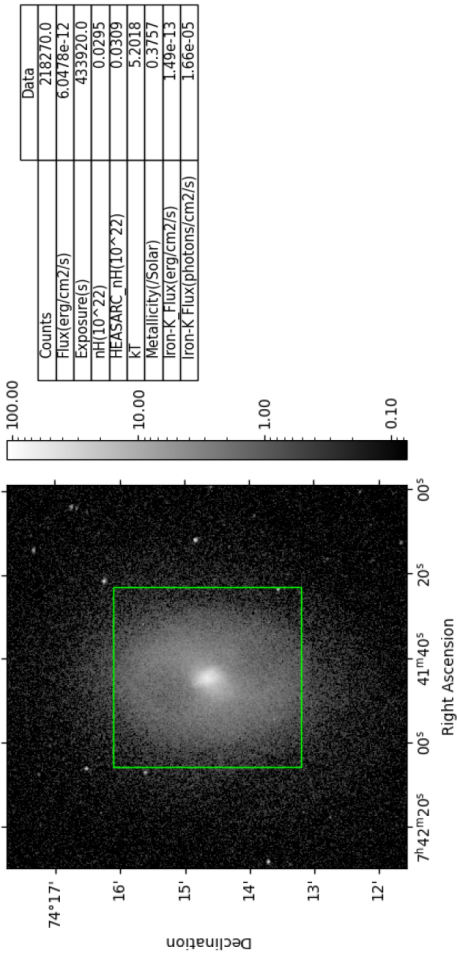
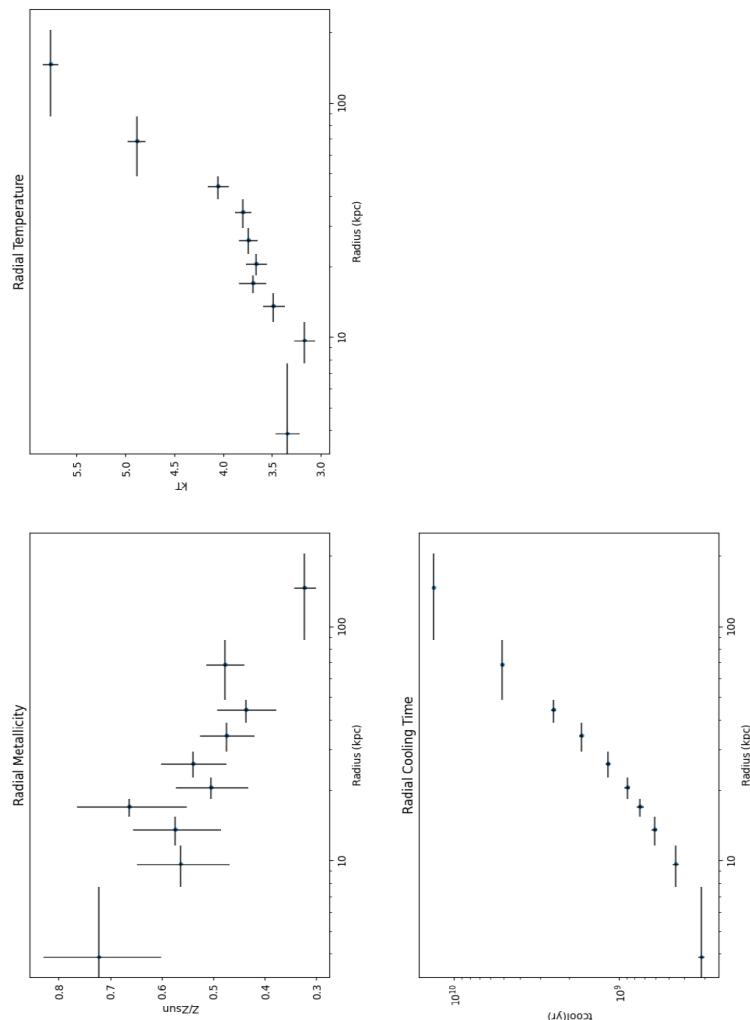
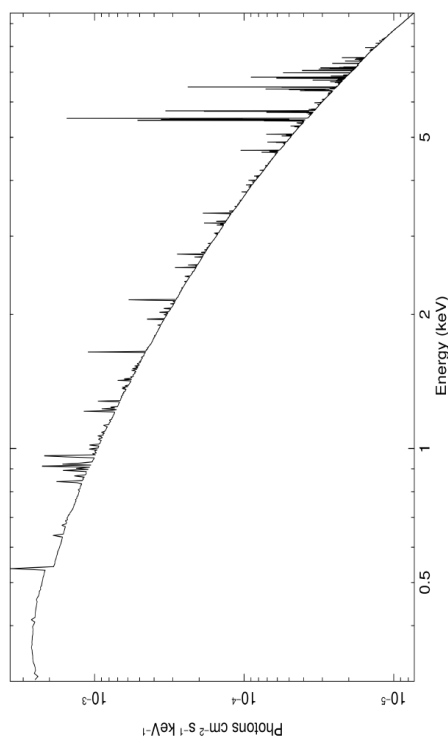


ne01mx 4-Jul-2023 1



# Galaxy Cluster: MS07

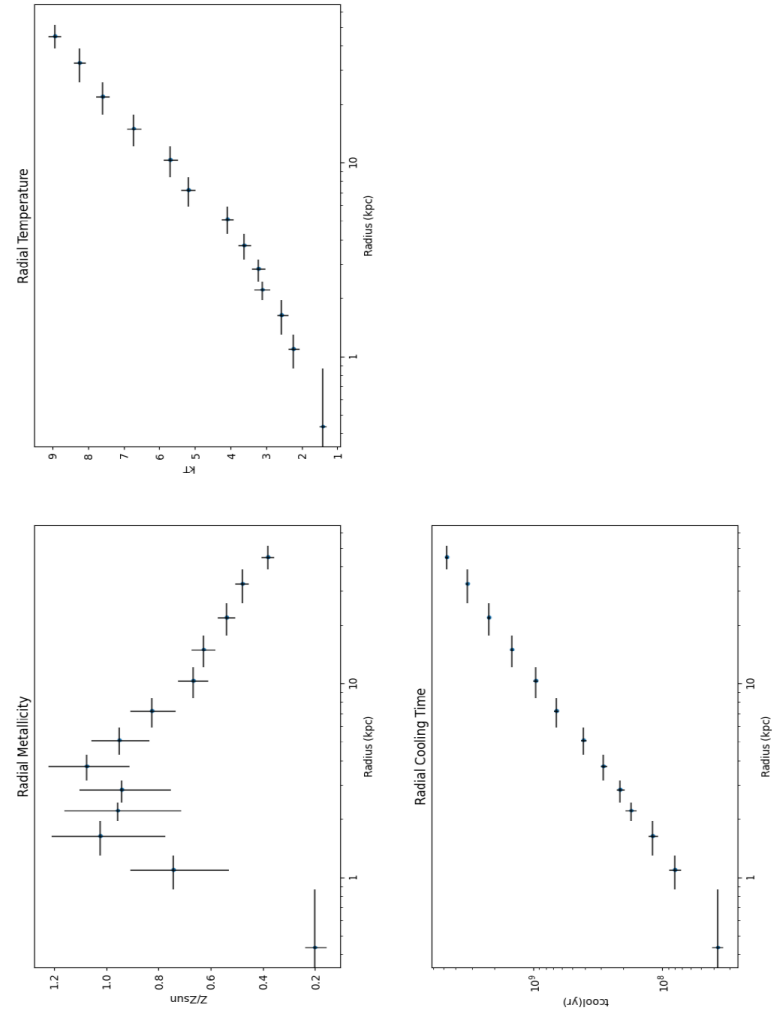
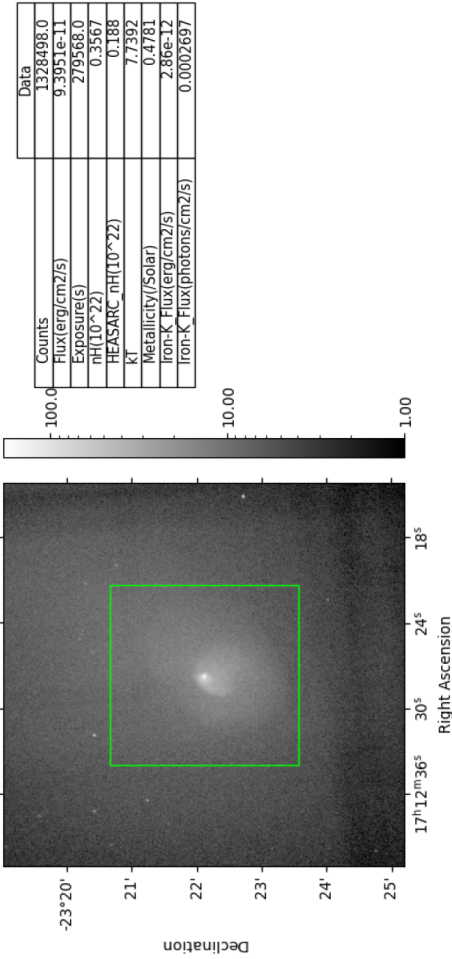
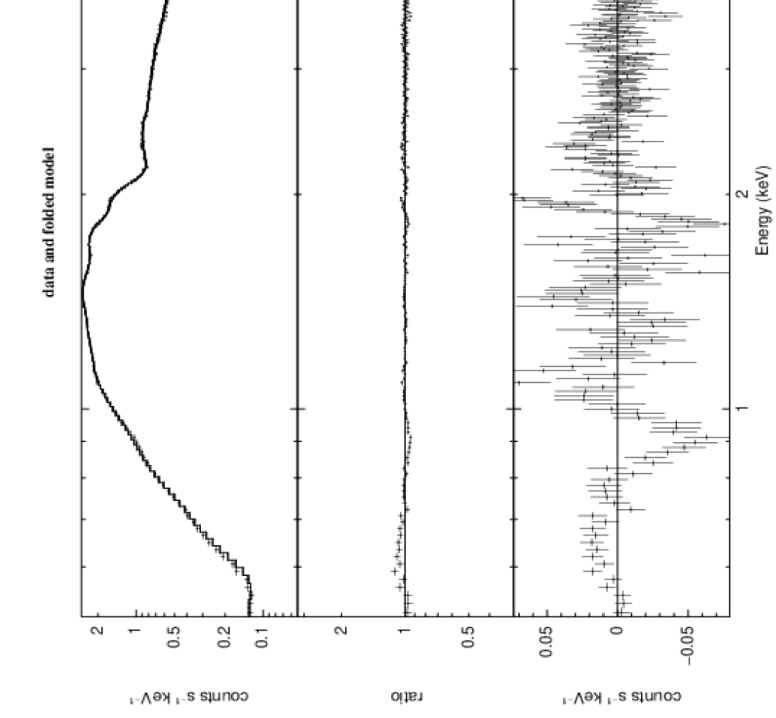
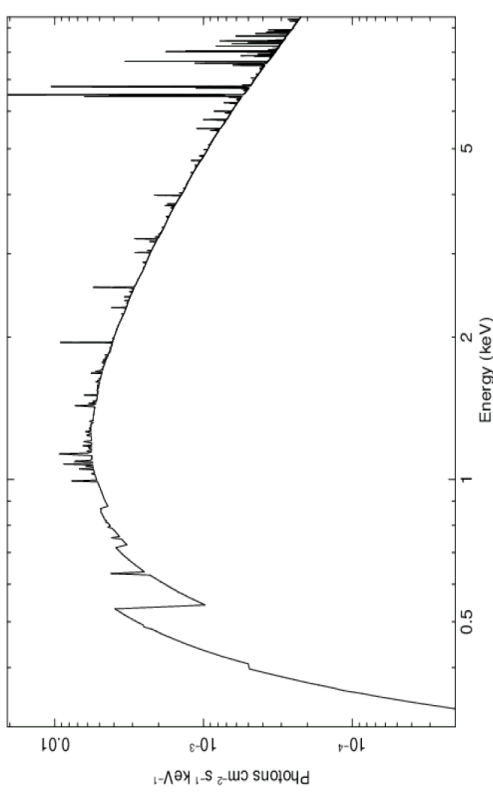
Current Theoretical Model



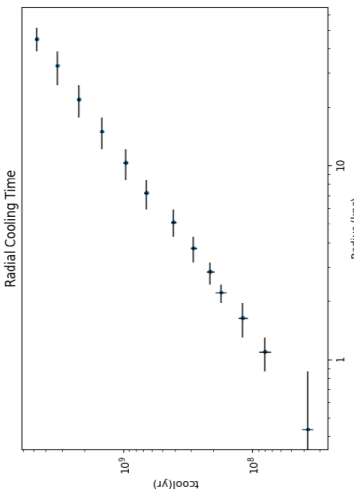
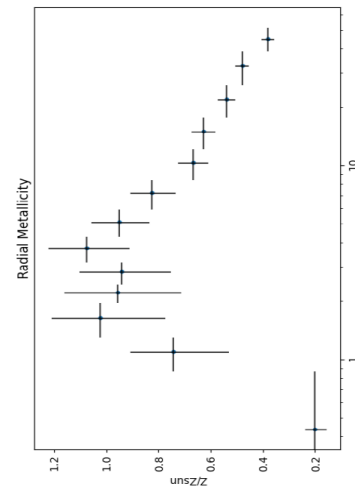
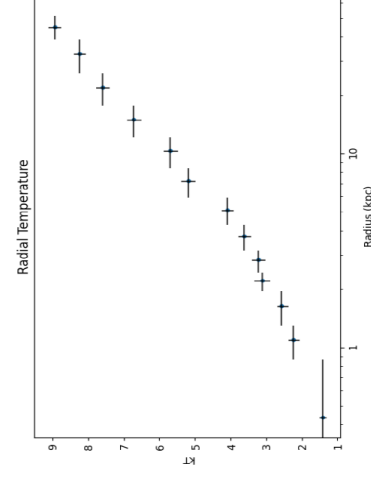
nebrix 30-May-2023 12:30

# Galaxy Cluster: Ophiuchus

Current Theoretical Model



neolmx 19-Jun-2023



counts s<sup>-1</sup> keV<sup>-1</sup>

rate

neolmx 8-Jun-2023 15:03